Available online at www.sciencedirect.com
SCIENCE DIRECT®
Physics Reports 376 (2003) 133–223
PHYSICS REPORTS
www.elsevier.com/locate/physrep

Paramagnetic Meissner effect and related dynamical phenomena

Mai Suan Li

Institute of Physics, Polish Academy of Sciences, Al. Lotnikow 32/46, 02-668 Warsaw, Poland

Accepted 12 December 2002
editor: D.L. Mills

Abstract

The hallmark of superconductivity is the diamagnetic response to external magnetic field. In striking contrast to this behavior, a paramagnetic response or paramagnetic Meissner effect was observed in ceramic high-T_c and in conventional superconductors. The present review is given on this interesting effect and related phenomena. We begin with a detailed discussion of experimental results on the paramagnetic Meissner effect in both granular and conventional superconductors. There are two main mechanisms leading to the paramagnetic response: the so-called d-wave and the flux compression. In the first scenario, the Josephson critical current between two d-wave superconductors becomes negative or equivalently one has a π junction. The paramagnetic signal occurs due to the nonzero spontaneous supercurrent circulating in a loop consisting of odd number of π junctions. In addition to the d-wave mechanism we present the flux compression mechanism for the paramagnetic Meissner effect. The compression may be due to either an inhomogeneous superconducting transition or flux trap inside the giant vortex state. The flux trapping which acts like a total nonzero spontaneous magnetic moment causes the paramagnetic signal. The anisotropic pairing scenario is believed to be valid for granular materials while the flux trap one can be applied to both conventional and high-T_c superconductors. The study of different phenomena by a three-dimensional lattice model of randomly distributed π Josephson junctions with finite self-inductance occupies the main part of our review. By simulations one can show that the chiral glass phase in which chiralities are frozen in time and in space may occur in granular superconductors possessing d-wave pairing symmetry. Experimental attempts on the search for the chiral glass phase are analysed. Experiments on dynamical phenomena such as AC susceptibility, compensation effect, anomalous microwave absorption, aging effect, AC resistivity and enhancement of critical current by external electric fields are considered. These phenomena were studied by Monte Carlo and Langevin dynamics simulations which show satisfactory agreement with experiments. We present a resistively shunted junction model describing rich dynamics of Josephson junction networks.

PACS: 74.25.Ha

E-mail address: masli@ifpan.edu.pl (M.S. Li).

0370-1573/03/$ - see front matter
doi:10.1016/S0370-1573(02)00635-X

Contents

1. Introduction

The phenomenon of superconductivity was first discovered in 1911 by H. Kamerlingh Onnes. He observed that when mercury was put into a liquid helium bath and cooled down to very low temperatures, its resistivity dropped to zero once the temperature becomes lower than a critical value T_c. It was soon observed that superconductors, except from zero resistivity, also exhibit unusual magnetic properties. In 1933 Meissner and Ochsenfeld found that when a superconducting specimen is placed in a low enough magnetic field and is subsequently cooled through its transition temperature, the magnetic flux is totally expelled from its interior. This phenomenon was called Meissner effect.

In the conventional Meissner phase the magnetic susceptibility is negative or the response to the external magnetic field is diamagnetic.

The revolutionary discovery of high temperature superconductivity by Bednorz and Muller [1] ignited an explosion of efforts in study of ceramic materials. One of such efforts led to the discovery of the so called *paramagnetic Meissner effect* (PME). Contrary to the standard diamagnetic response to the external field, a paramagnetic signal was observed in certain ceramic superconductors upon cooling in low enough fields [2–5]. In other words, the field cooled (FC) susceptibility becomes positive whereas the zero field cool (ZFC) magnetization remains negative. This effect is now referred to as the PME or as the Wohlleben effect [6]. The existence of the PME is quite surprising because according to the Ginzburg–Landau phenomenology for continuous media [7], the lowest free energy states should be diamagnetic.

The anomalous PME in ceramic superconductors has been interpreted in the framework of different models, such as spontaneous supercurrents due to vortex fluctuations combined with pinning [2], orbital glass [8], the presence of so called π contacts [4,9–11,6,12], and Josephson junctions [13,14]. In this review we focus on the most prominent d-wave mechanism proposed by Sigrist and Rice [9,10]. According to their theory, the nature of the unusual paramagnetic behavior may be related to the existence of π-junctions characterized by negative Josephson couplings (conventional 0-junctions have positive couplings). It was argued that such π-junctions are a consequence of $d_{x^2-y^2}$ type pairing symmetry [9]. If a loop consists of odd number of π junctions then one can show that the spontaneous current (or magnetic moment) circulating around it becomes nonzero. Such a frustrated π loop would, therefore, behave like a paramagnet and have the paramagnetic response to the external magnetic field. The existence of the d-wave pairing seems to be supported by phase-sensitive and phase-insensitive experiments [15].

The situation becomes ambiguous when the PME was observed even in conventional superconductors such as Nb [16,17] and Al [18]. This has prompted the appearance of a less-exotic mechanism based on flux capture inside a superconducting sample and its consequent compression with lowering temperature [19–21]. The flux trap can be caused by inhomogeneities [19,20] but could also be an intrinsic property of any finite-size superconductor due to the sample boundary [21]. The trapped fluxes play the same role as spontaneous supercurrents in the d-wave mechanism and give rise to the PME.

At present, it is not clear if one needs the exotic d-wave mechanism to explain the PME in ceramic materials or the flux trapping is adequate for both conventional low-T_c and high-T_c superconductors [18,22]. The study of dynamical phenomena such as the microwave absorption (MWA) [3], the compensation effect [23], the aging [24] and enhancement of critical current [25], may shed light on this important issue. The anomalous MWA, e.g., was observed [3] only in the ceramic samples showing the paramagnetic signal. Simulations by different groups show that all of dynamical effects may be captured by the multi-loop model of the Josephson network [12] with π-junctions. So the study of dynamics effects in ceramic superconductors supports the d-wave mechanism.

Recently we have proposed that a novel thermodynamic phase might occur in zero external field in unconventional superconductors [26,27]. This phase is characterized by a broken time-reversal symmetry and called a chiral glass phase. The key idea is that the random distribution of 0- and π-junctions between adjacent $d_{x^2-y^2}$ superconducting particles causes the frustration effect and induces the chiral glass transition. In the chiral glass phase, similar to spin glasses, chiralities [28] are frozen

in space and in time. Using the multi-loop model [12] one can show that this phase is stable even under the screening [27]. Since the existence of the chiral glass would favour the d-wave mechanism for the PME, its study is very important for classification of the symmetry of the order parameter. The experimental search for the chiral glass phase in ceramic samples of different groups gives controversial results [29–32]. In this review we also briefly discuss the difference between the chiral glass and other glassy phases in impure type-II superconductors such as the gauge glass, vortex and Bragg glass.

It should be noted that results obtained before 1995 were summarized in the review article of Sigrist and Rice [10]. However, these authors discussed only the d-wave mechanism of the paramagnetic Meissner effect and related experiments in ceramic materials and interesting dynamical phenomena correlated with the PME were not addressed. The present review focuses on the progress achieved after 1995. The main developments of this period are:

(a) the discovery of the PME in conventional superconductors [18];
(b) more detailed study of the PME and related dynamical phenomena in ceramic materials;
(c) flux compression mechanism [19,21] which is not based on the d-wave pairing symmetry;
(d) theoretical and experimental search for a chiral glass phase.

The article is organized as follows. In Section 2 we present a brief summary of experimental results on the PME in both ceramic and conventional superconductors. In Section 3 we review the mechanisms for occurrence of π junction. One of them is relied on the scattering on magnetic impurities and the another, more intrinsic, mechanism is based on the anisotropic pairing of superconducting electrons. Section 4 concerns theory and simulations of the PME in ceramic superconductors employing single-loop and multi-loop models of the Josephson junction network with π junctions. In Section 5 we discuss the flux compression mechanism for the PME based on the Bean critical model and the Ginzburg–Landau equation approach. Section 6 is focused on the simulation and experimental search for the chiral glass phase in granular materials. Experiments and simulations on dynamical phenomena related to the PME are presented in Section 7. The multi-loop model is shown to provide an unique tool to describe all of these effects.

2. Experiments on paramagnetic Meissner effect

In the Meissner phase the total magnetic field B inside conventional superconductors vanishes and we have

$$\vec{B} = \vec{H} + 4\pi\chi\vec{M} = 0 \ ,$$
$$\chi = \frac{\partial M}{\partial H} = -\frac{1}{4\pi} \ , \tag{2.1}$$

where H, M and χ are the external field, the induced magnetization and the susceptibility. Due to the finite London penetration depth (of order of 500 Å) the magnetic fluxes do not, however, entirely

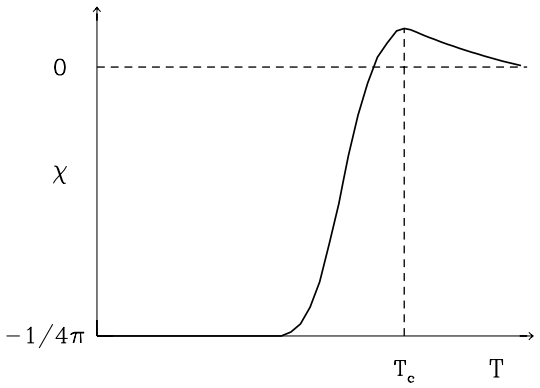

Fig. 1. Schematic temperature dependence of the susceptibility of superconductors without the PME.

pull out from the interior and χ approaches $-1/4\pi$ as $T \to 0$. It is shown schematically in Fig. 1. Above T_c one has the paramagnetic behavior $\chi = c/T$ [7]. The susceptibility is slightly positive even in the narrow temperature region below T_c but it has nothing to do with the PME where the FC susceptibility remains positive up to $T = 0$.

2.1. High-temperature superconductors

Approximately 100 different cuprate materials, many of which are superconducting, have been discovered since 1986. Cuprates have layered structure, with quite similar a- and b-axis and considerably longer c-axis. They consist of CuO_2 planes, normal to c-axis, separated by layers containing other types of atoms. The superconductivity occurs in the CuO_2 layers and it is sensitive to the oxygen content. The layered structure gives rise to strong anisotropy of many physical quantities.

The PME was first observed in the $Bi_2Sr_2CaCu_2O_{8+\delta}$ (Bi2212) the structure of which is schematically shown in Fig. 2. The lattice constants are $a = 5.141$ Å, $b = 5.148$ Å and $c = 30.66$ Å. The onset of superconductivity occurs at $T_c \approx 87$ K and the transition width is about 5 K. In general, T_c depends on the oxygen content [4].

The Bi2212 samples are prepared by two techniques: the reaction sintering [2,4,38] and the melt-cast [4]. As shown by Scanning Electron Microscopy, sintered Bi2212 have a porous structure with a typical grain size of 1–4 μm [4] (see also Table 1) and typical thickness of 0.2–0.4 μm [39]. High resolution transmission electron microscopy studies [33] have shown that the samples obtained by the melt-cast technique have an extremely polydomain microstructure on a μm length scales. The grains are significantly larger and more densely packed compared to the sintered samples. The single crystalline domains are preferably c-axis oriented with extremely sharp interfaces (width $\leqslant 1$ nm) which provide good contacts between the domain in ab-planes. Such kind of interfaces result in Josephson junctions with quite large critical currents ($10^5 - 10^6$ A/cm^2 [33,40]). Depending on the morphology of the samples the Bi-2212 may exhibit the PME or not.

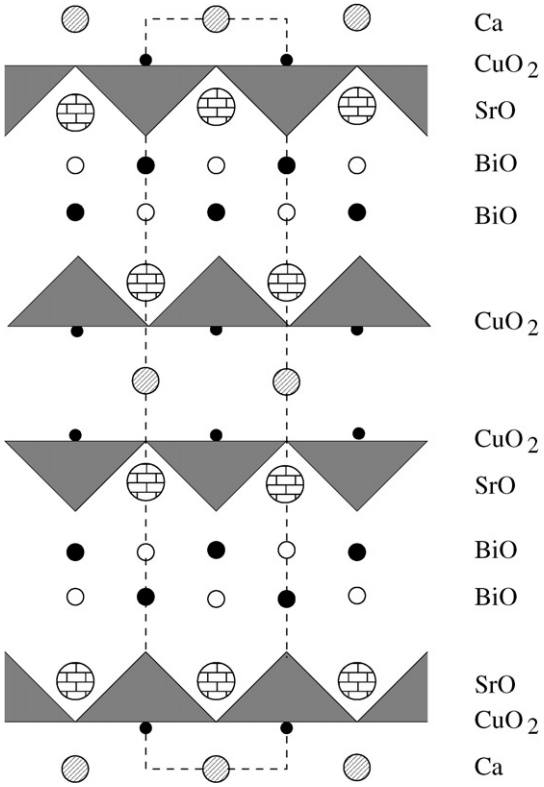

Fig. 2. Schematic structure of the crystal lattice $Ba_2Sr_2CaCu_2O_{8+x}$ where triangles represent pyramids with an oxygen atom in each corner. The lattice constants $a = 5.141$ Å, $b = 5.418$ Å and $c = 30.66$ Å. Adapted from Ref. [39].

Table 1
Ceramic superconductors showing the PME

Compound	Source	T_c (K)	J_c (A/cm^2)	Grain size (μm)
$Bi_2Sr_2CaCu_2O_{8.182}$	[4]	84	10^5–10^6 [33]	2–3
$Bi_{1.73}Pb_{0.27}Sr_2Ca_2Cu_3O_y$	[4]	110	10^5–10^6	4
$YBa_2Cu_3O_{7-\delta}$	[34]	89	—	—
$Nd_{2-x}Ce_xCuO_y$	[35]	21	—	—
$La_2CuO_{4+\delta}$	[36]	32	10^4–10^5	—
Ba–K–Bi–O	[37]	32	—	—

Fig. 3 shows the standard Meissner behavior of the dc susceptibility in granular superconductor $Bi_2Sr_2CaCu_2O_8$ under FC and ZFC conditions. The results were obtained on a high-quality sintered sample [3,4]. In the FC regime one has a fractional Meissner effect due to a certain amount of magnetic flux trapped in the voids of the multiply connected sample. The screening in the ZFC

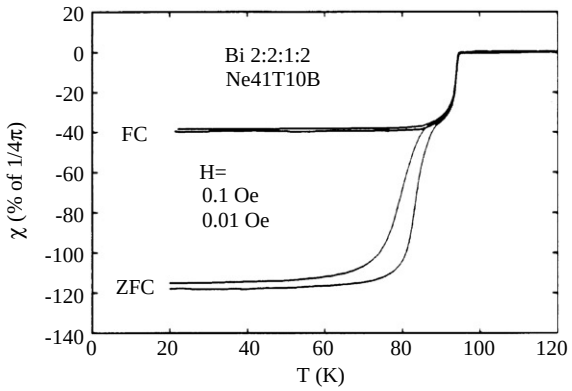

Fig. 3. ZFC and FC susceptibilities as a function of temperature of a high-quality ceramic Bi-2212 in very low fields. The reduced FC flux expulsion resembles the behavior commonly observed at intermediate field. After Braunish et al. [4].

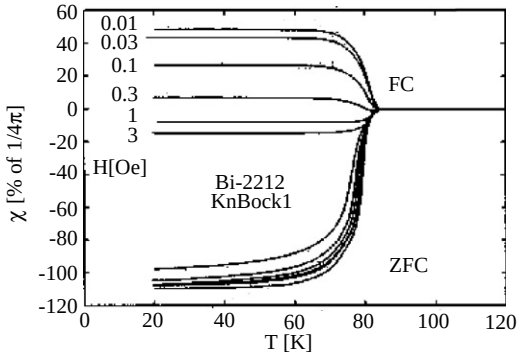

Fig. 4. ZFC and FC susceptibilities as a function of temperature of a granular superconductor $Bi_2Sr_2CaCu_2O_8$ exhibiting the PME in very low fields. Reprinted from [3].

mode is, however, larger than 100% of $-1/4\pi$. It is because the screening currents, which are induced by applying the field below T_c at the start of the measurement, screen also voids present in those granular materials [4]. Therefore the screened volume is larger than the effective volume with respect to the mass of the sample as calculated by the X-ray density.

The unusual behavior of the dc susceptibility in Bi-2212 compound obtained by the melt-cast technique is shown in Fig. 4. For very small external fields ($H \sim 0.01$–1 Oe) a paramagnetic response in the FC conditions appears below the superconducting transition temperature. The smaller the H, the stronger the paramagnetic signal, as seen from Fig. 5.

For fields $H \geqslant 1$ Oe, χ becomes slightly diamagnetic. The fact that even small fields are sufficient to enforce nearly complete polarization reveals that orbital currents spontaneously created in the superconducting state should interact weakly. It was shown that the magnetization consists of two

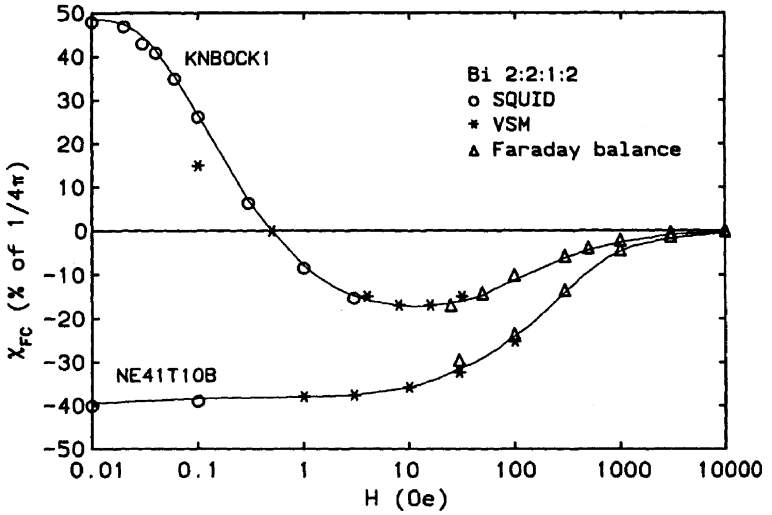

Fig. 5. Field dependence of the FC susceptibility of the melt-process sample KnBock1 and of the sintered sample Ne41T10B at 20 K. The applied field was varied between 10 mOe and 10 kOe. The measurements were performed with the SQUID magnetometer, the vibrating sample magnetometer (VSM), and a Faraday balance (see [4] for details). The PME of KnBock1 sample emerges in fields $H < 2$ Oe. Reprinted from [4].

parts: the conventional diamagnetic part and the paramagnetic one [4,41]

$$M(H) = M_0(H) + \chi_{\mathrm{dia}} H \ ,$$
$$M_0(H) = \frac{M_s H}{(H_0 + H)^{\alpha}} \ ,$$
$$\chi = \chi_{\mathrm{dia}} + \frac{M_s}{(H_0 + H)^{\alpha}} \ . \tag{2.2}$$

Here χ_{dia}, M_s, α and H_0 depend on the samples (H_0 may be interpreted as the field below which the thermal and interaction effects suppress complete polarization). For Bi-2212, e.g., χ_{dia} is about 17% of $-1/4\pi, \alpha \approx 1, H_0 = 0.16$ Oe and $M_s = 0.095$ G/4π.

As to the ZFC experiments, at a first glance one may think that the Meissner effect is similar to that in ordinary ceramic superconductors. Namely, χ_{ZFC} depends on T but not on the external field. However, a more careful inspection [2,38] shows its rather weak field dependence. This nonlinear effect gets enhanced near the phase transition to the superconducting state.

Recently Freitag et al. [33] have found a clear qualitative distinction between the morphology of the samples with and without the PME when approaching a length scale of several microns. It is shown in Fig. 6 where High-Resolution Transmission Electron Microscopy photos of two respective samples are shown. The samples with PME are characterized by an extremely polycrystalline "chaotic" structure with typical sizes of single crystalline domains $\leqslant \mu$m (see Fig. 6a). In contrast, as seen in Fig. 6b, samples without PME show a pattern of large well-ordered single crystalline domains. The density of the domain boundaries is much larger for the former samples than for the latter.

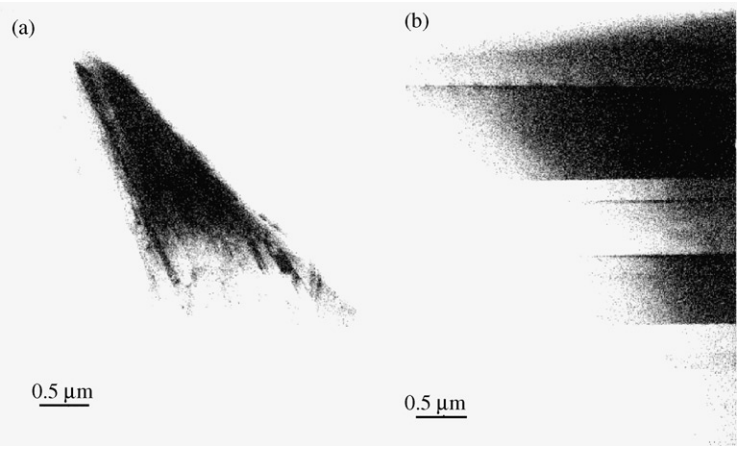

Fig. 6. High-Resolution Transmission Electron Microscopy photos of samples with PME (a) and without PME (b) on the scale of several microns. After Freitag et al. [33].

The another class of materials where the PME has been also observed is high-quality, twined single crystals $YBa_2Cu_3O_{7-\delta}$ [34,42]. The study of this material would help to discriminate the d-wave and the grain boundary origin of π-junctions. Since crystals are single the later mechanism can be ruled out. The PME has found to appear only with the magnetic field parallel to the c axis, i.e., the spontaneous currents are confined to the ab plane [34]. It is clear from Fig. 7, the magnitude of the observed signal here is considerably smaller than that for the ceramic samples (less than 3% of the full shielding value as compared to up to 50%) [3,4,23]. The field below which a PME is observed is, however, much higher than that in the ceramic samples (0.7 mT compared to about 0.05 mT). Since the sample is a single crystal one has a complete flux expulsion in the ZFC regime.

A positive FC magnetization has also been observed in $Nd_{2-x}Ce_xCuO_y$ [35], $La_2CuO_{4+\delta}$ [36,43], and Ba–K–Bi–O compounds [37]. In the later case the magnitude of χ_{FC} is much smaller than the one observed in BSCCO samples at weak fields but it remains positive for much larger applied fields.

Table 1 collects ceramic high-T_c superconductors showing the PME.

2.2. Conventional superconductors

One of the scenarios for the PME in granular hole-doped cuprates discussed above is that the FC paramagnetic response appears from current loops with π phase shifts of the superconducting order parameter at some grain-boundary junctions. It was argued that such behavior would be expected to occur in a d-wave superconductor, but not in a conventional s-wave superconductor. The test of this hypothesis led to the discovery of the PME in conventional superconductors like Nb [44,16,17,45], Al [18] and the Nb–AlO_x–Nb tunnel junctions [46,47]. The occurrence of the PME in these systems is probably due to the confined geometry and flux trapping. In this section we discuss the main experimental findings for the conventional superconductors.

In the experiments of Minhaj et al. [44,16] niobium disks of diameter 6.6 mm and thickness 0.127 mm were used to study the PME. The dc FC magnetization shows the paramagnetic response

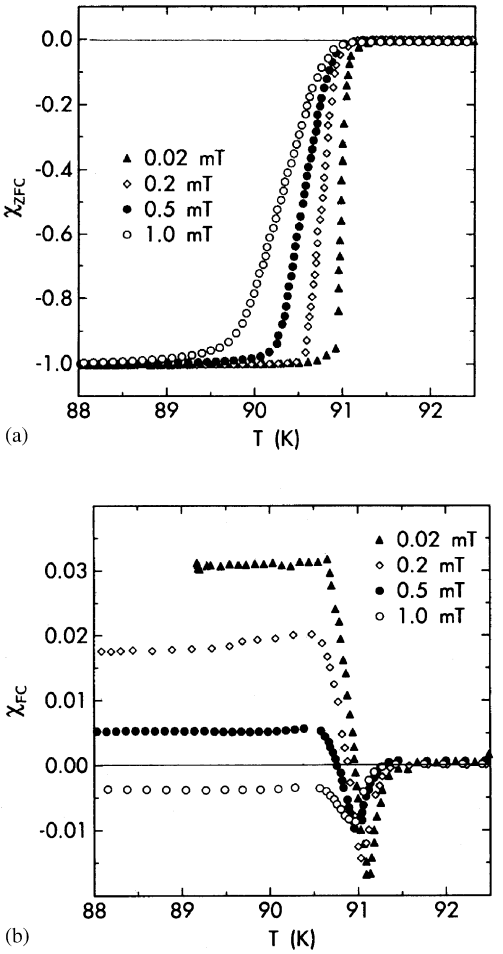

Fig. 7. Susceptibility of single crystal $YBa_2Cu_3O_{7-\delta}$ in various applied fields vs. temperature T. From Riedling et al. [34].

below the superconducting transition temperature $T_c \approx 9,2$ K when the applied magnetic field is normal to the disk. It is demonstrated in Fig. 8. The paramagnetic signal is much weaker compared to its counterpart in BiSrCaCuO compounds and it becomes diamagnetic for fields larger than 20 Oe.

Comparing Figs. 7 and 8 one can see the remarkable similarity in the temperature dependence of the susceptibility of Nb disks and single crystal $YBa_2Cu_3O_{7-\delta}$. With increasing temperatures the ZFC data indicate the presence of two different superconducting transitions at $T_1 \approx 9.2$ K and $T_p \approx 9.06$ K. The strong field dependence of χ_{ZFC} indicates that the local field is larger than the lower critical field $H_{c1}(T)$ in the interval $T_p < T < T_1$. The appearance of the two transition temperatures is also seen in the FC measurements: at T_1 the paramagnetic moment first appears (vanishes) and a lower temperature T_p defines the temperature where the positive moment no longer increases [16,48]. The sharp increase of positive FC magnetization upon cooling below T_1 is fairly spontaneous similar to the onset of global diamagnetic screening currents at T_c rather than the viscous nature exemplified by

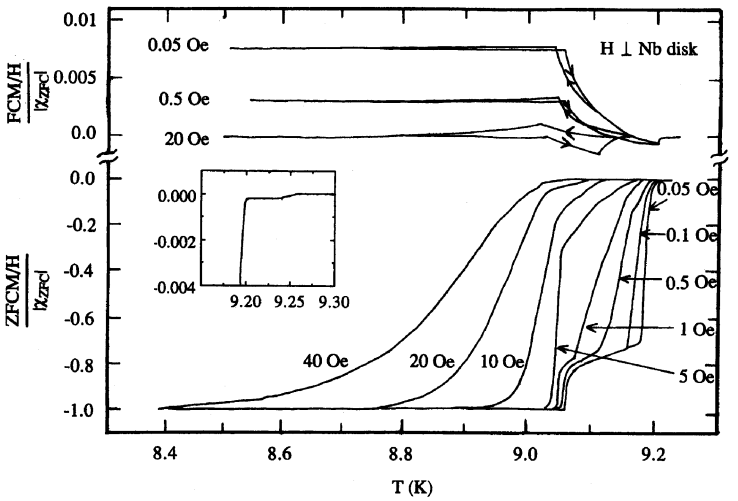

Fig. 8. The FC (upper) and ZFC (lower) susceptibility for a macroscopic Nb disk with magnetic fields applied normal to the disk surface. The data are scaled to the complete shielding value of χ_{ZFC}. The inset shows an enlargement of χ_{ZFC} around $T = 9,26$ K. From Thompson et al. [16].

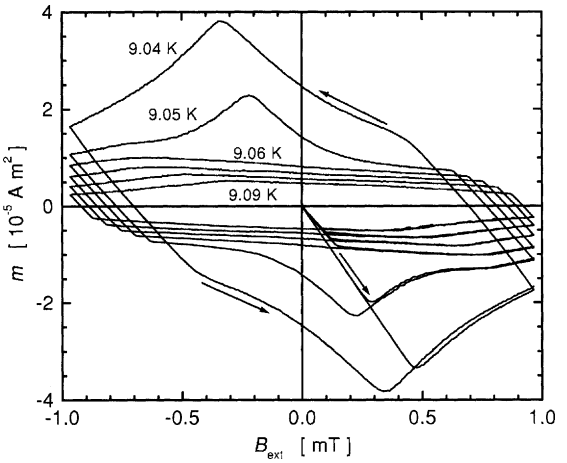

Fig. 9. Magnetic hysteresis loops of the Nb disks in the temperature range $9.04 \leqslant T \leqslant 9,09$ K for 0.01 K increments. The remarkable change of their shapes between 9.05 and 9.06 K, i.e., at $T = T_p$. From Pust et al. [45].

flux flow. Below T_p this moment apparently does not change with temperature and can be regarded as an additive constant to the FC magnetic moment of a nonPME superconductor.

To gain more insight on the nature of the FC paramagnetic moment for the Nb disks, magnetic hysteresis loops were measured [16,45]. A set of such loops recordered in the temperature range from 9.04 to 9.09 K, i.e., around T_p are shown in Fig. 9. Between T_c and T_1 the system is superconducting but only a small diamagnetic screening current can be induced by ramping the external field. Below T_1 the critical current is expected to increase significantly and the loops exhibit a strange, nearly

parallelogramlike shape the size of which increases with lowering temperature [45]. Just below T_p the hysteresis loops change their shapes drastically and they are more reminiscent of a type-II superconductor with the magnetization becoming less diamagnetic as the flux penetrates into the bulk for $H \geqslant H_{c1}$.

Interesting similarity to the $YBa_2Cu_3O_{7-x}$ single crystals [34] results in the hysteresis behavior of the FC magnetization between cooling and warming cycles. As one can see from Fig. 8 the FC magnetizations are more positive than its warming counter part. On cooling, the flux should overcome activation-type process in order to be expelled and consequently the FC magnetization is more positive than the equilibrium one. In the warming cycle, the flux cannot, however, easily penetrate the sample and the magnetization is more diamagnetic. This behavior is common in type-II superconductors and is consistent with a theoretical interpretation based on the critical-state model [49].

It has been found that the PME in Nb samples is very sensitive to their surface and geometry [16,17,45]. In particular, the paramagnetic response occurs in Nb disks cut from some sheets of rolled Nb. Disks cut from other source materials do not show the PME [17]. Fig. 10 shows the FC magnetizations obtained before and after polishing the sample faces. Interestingly, the FC paramagnetic signal disappears after both faces of the sample were polished. This gives strong evidence that the surface pinning of the magnetic flux plays an important role. One may think that the PME

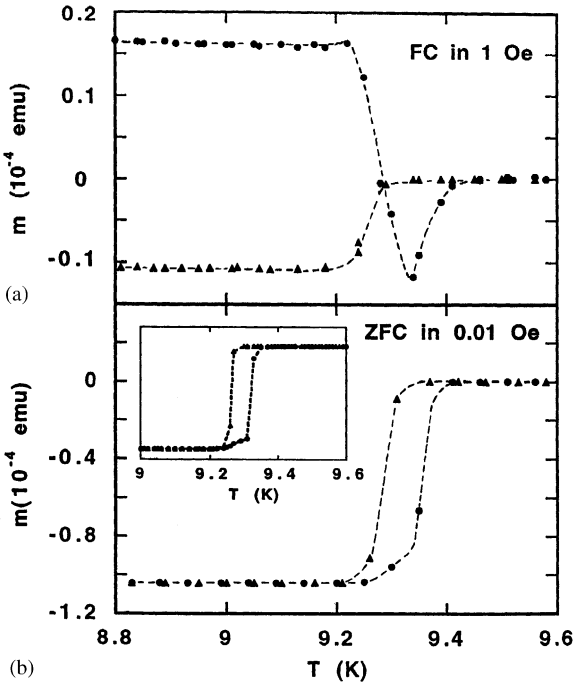

Fig. 10. FC (a) and ZFC (b) magnetizations of a Nb disk measured before (solid squares) and after (solid triangles) polishing the sample surface. The values of the external magnetic field are shown next to the curves. Inset: a high point density ZFC measurement at 0.05 Oe from another sample cut. The PME disappears after both faces of the sample were polished. From Kostic et al. [17].

is likely to arise from inhomogeneously trapped flux, and is unlikely to have any relationship with d-wave superconductivity.

We now discuss the PME in small (micrometre-size) superconductors. The experiments were carried out for Nb and Al discs [18] with diameters from 0.3 to 3 μm and thicknesses from 0.03 to 0.15 μm. The thickness is comparable to the characteristic penetration depth $\lambda \sim 500$ Å [50]. Study of small samples is interesting in two ways. First, an application of the Koshelev–Larkin model [19] to data for Nb discs [17] suggested that the paramagnetic magnetization must be small for samples much thicker than λ; however, for very thin films one can expect a much larger effect due to macroscopic penetration of Meissner currents into the sample interior. Second, confinement of superconductivity in a small volume leads to pronounced quantization, so that a mesoscopic superconductor resides in one of well-resolved states, depending on temperature and magnetic field (superconducting states are characterized by a different number and distribution of vortices [51–54]). This allows one to measure magnetization of individual vortex states and rules out the pinning effect.

The typical field dependence of the FC paramagnetic moment of mesoscopic samples is shown in Fig. 11 [18]. The strong oscillation clearly seen for the larger sample of diameter 2.5 μm is due to size quantization. Each jump corresponds to a change in the number of vortices inside the disk, which can either form an array of single quantum vortices or assemble into a single giant vortex [21,51–54]. The latter configuration is expected at fields between the second and third critical field, $H_{c2} < H < H_{c3}$, where H_{c3} is related to the surface superconductivity [21]. The smaller sample (diameter 1.0 μm) does not show the paramagnetic response over the entire field interval. This qualitatively different behavior may be explained by the fact that, in smaller sample the superconductivity is suppressed

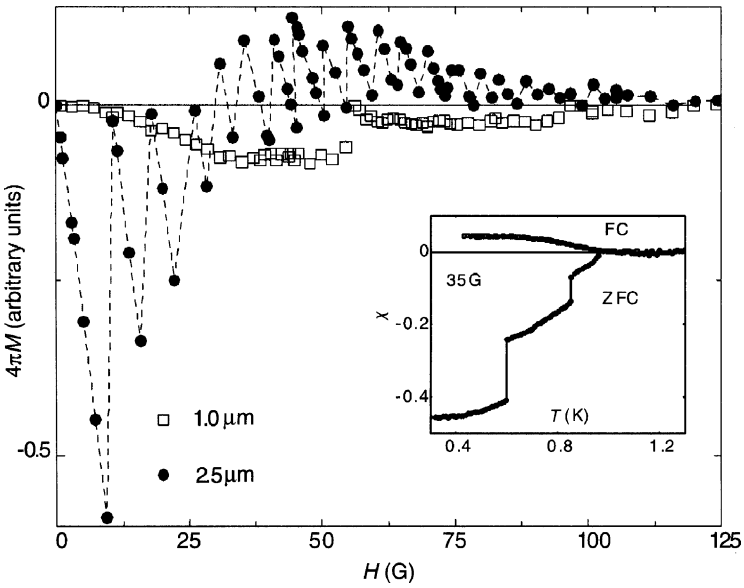

Fig. 11. The field dependence of the Meissner response for Al disks of diameter 1.0 (open squares) and 2.5 μmi (closed circles) at $T = 0.4$ K. The dashed line is a guide to the eye. The inset compares FC and ZFC magnetization of the 2.5 μm disk at the field where the paramagnetic response is close to its maximum. The jumps in the ZFC curve correspond to entry of individual vortices into the disk interior. After Geim et al. [18].

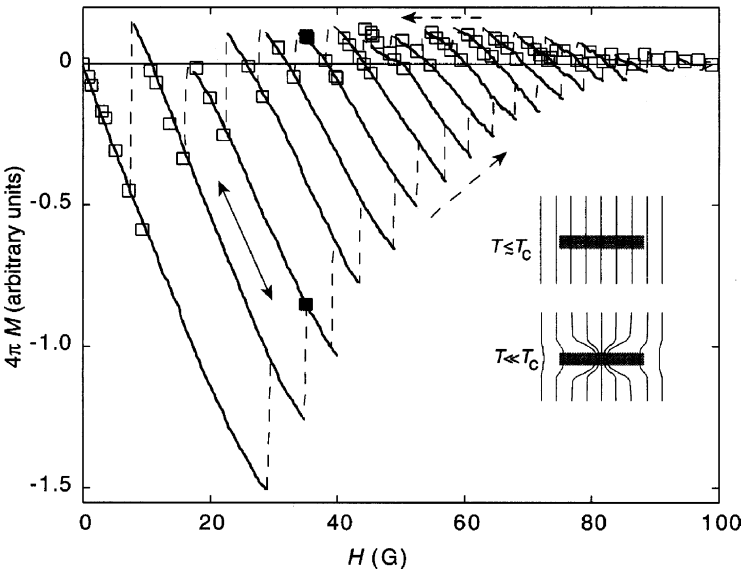

Fig. 12. The magnetization measured by cooling in a field and by sweeping the field at a constant temperature (0.4 K). Arrow shows the direction of the sweep. The FC data shown by open squares are for the 2.5 μm disk of Fig. 11. The solid curves were measured by pausing at various fields and then sweeping the field up and down. When the field swept continuously, the magnetization evolves along one of the solid curves until it reaches the end of this curve and jumps to the next one belonging to another vortex state. Then, the process repeats itself all over again as shown by dashed lines. The closed squares at 35 G indicate the low-temperature states for the FC and ZFC curves of Fig. 11. The inset illustrates the compression of a giant vortex into a smaller volume which allows extra flux to enter the sample at the surface. From Geim et al. [18].

by ~ 3 flux quanta entering the whole disk area while $\sim 20\Phi_0$ (Φ_0 is the flux quantum) are needed to spoil superconductivity of the larger disk [18,51–53]. Thus, the diamagnetic response is always observed in low magnetic fields and the PME occurs only in intermediate fields allowing at least several flux quanta penetrate into the interior. This seems to contradict the previous studies on macroscopic samples, where the paramagnetic signal is recorded in very low fields and gradually disappeared with increasing field. Such discrepancy is due to the large number of flux quanta (many thousands) may enter the macroscopic samples even in lowest fields.

The nature of the PME becomes more evident from measurements of the magnetization by sweeping the magnetic field at a constant temperature [18] (see Fig. 12). Instead of a single magnetization curve characteristic for macroscopic samples one has a family of curves corresponding to different vortex states. Since several superconducting states are possible at the same magnetic field, the states in which the PME occurs are metastable. Only the state with the most negative magnetization is thermodynamically stable [52,53]. The metastability results from the sample surface which favours a large superconductivity and opposes both vortex escape and entrance [55]. As shown below, combining the ideas of flux compression [19] and the trap in giant vortex states [21] one can explain the experimental findings for mesoscopic superconductors [18].

3. Mechanisms for π junction

3.1. Scattering on paramagnetic impurities

The effect of magnetic impurities present in the barrier between s-wave superconductors on the tunneling current was first studied by Kulik [56] (see also [57]). Later Bulaevskii et al. [58] have realized that the presence of such impurities may lead to a spin-flip intermediate state which actually shifts the phase by π.

Consider a SIS contact with magnetic impurities in the thin insulator layer. The Hamiltonian of this system is as follows [56,58]:

$$H_T = \sum_{\vec{k},\vec{k}',\vec{n},s,s'} (t_{\vec{k}\vec{k}'}\delta_{ss'} + v_{\vec{k}\vec{k}'\vec{n}}\vec{\sigma}_{ss'}S_{\vec{n}})a^{+}_{\vec{k}s}b_{\vec{k}'s'} + c.c \ . \tag{3.1}$$

Here $a_{\vec{k}s}(b_{\vec{k}s})$ are electron annihilation operators in superconducting layer A (B); $S_{\vec{n}}$ is spin of impurities localized at point $\vec{n}$ and $\vec{\sigma}$ are Pauli matrices.

Using the Green function technique [59], in the second order of perturbation theory we obtain the stationary Josephson current J and the contact energy E in the following form

$$J = J_c \sin\phi, \ E = -\frac{\hbar}{2e}J_c\cos\phi, \quad J_c = J_0 - J_s$$

$$J_0 = 2\pi^2 e t^2 N^2(0)\Delta(T)\text{th}\,\frac{\Delta(T)}{2T} \ ,$$

$$J_s = 2\pi^2 e\sum_{\vec{n}} v^2_{\vec{n}} S(S+1)N^2(0)\Delta(T)\text{th}\,\frac{\Delta(T)}{2T} \ , \tag{3.2}$$

where t^2 and $v^2_{\vec{n}}$ are average values of $t^2_{\vec{k}\vec{k}'}$ and $v^2_{\vec{k}\vec{k}'\vec{n}}$ on the Fermi surface respectively, $N(0)$ the density of states on the Fermi surface, $2\Delta(T)$ the energy gap and ϕ the difference between superconducting phases. J_0 is the standard Ambegaokar-Baratoff term and J_s describes the electron tunneling with the spin flip [56].

Since $v_{\vec{k}\vec{k}'\vec{n}} \sim [\varepsilon_d(\varepsilon_d + U)]^{-1}$ [60], where ε_d is the energy of one electron and U the energy of the Coulomb repulsion between two electrons, one can choose ε_d so that J_c becomes negative ($J_s > J_0$) [58]. The another possibility to have $J_c < 0$ is that, as follows from Eq. (3.2), the concentration of magnetic impurities should be high enough making the spin flip term to be dominant.

Rewriting the Josephson current as

$$J = \begin{cases} J_c\sin(\phi + 0) & \text{if } J_c > 0 \ , \\ |J_c|\sin(\phi + \pi) & \text{if } J_c < 0 \ , \end{cases} \tag{3.3}$$

one can understand the meaning of terminology *π-junction*. Namely, in the case when the critical current $J_c < 0$ the current (or the contact energy) has the same form as in the conventional case with $J_c > 0$ [10] but the phase is shifted by π. For this reason an junction with negative critical current is called π junction whereas $J_c > 0$ corresponds to the standard 0 junction.

An another possibility of occurrence of negative critical currents was also pointed out by Spivak and Kivelson [61]. The main difference from the Bulaevskii approach [58] is that they described an impurity by the Anderson model in a regime where the localized magnetic moments exist. Spivak

and Kivelson argued that J_c may become negative in a dirty system due to an interplay of disorder and electron correlations. Similar results were obtained earlier by Altshuler et al. [62].

The existence of π-junctions leads to non-trivial physical phenomena. In the next section we will show that the spontaneous current in the ground state of a frustrated loop of odd number of π junctions is nonzero. This can serve as a reason for the paramagnetic response to the external magnetic field.

3.2. *d-wave picture of a π-junction*

In all cases discussed above the appearance of the π junction depends not on the intrinsic properties of a superconductor, but rather on external conditions like degree of disorder, impurity concentration etc. Furthermore, the spin flip mechanism, for example, may require the high density of magnetic impurities causing the strong magnetic interaction which would invalidate elastic tunneling.

There is, however, another, intrinsic and more exciting scenario for π-junctions: the spontaneous moments may naturally occur in ceramic superconductors with the d-wave pairing symmetry [9]. This idea was inspired by the works of Geshkenbein and co-workers [63,64] on heavy-fermion superconductivity showing that special arrangements of junctions may lead to the π shift. In this chapter, using the Ginzburg–Landay theory for the Josephson junction with two connected d-wave superconductors we show that the critical current may be positive or negative.

It is well established that the phonon mediated electron-electron interaction gives rise to spin-singlet pairing with s-wave symmetry [65] in conventional low-T_c superconductors. The question of symmetry of the order parameter of high-T_c superconductors is under intense debate [66,67]. Although the mechanism of high-T_c superconductivity remains unknown experiments on Shapiro steps [68], the magnetic-flux states of YBCO [69], the Andreev-reflection [70] and spin susceptibilities [71,72] give strong evidence for spin-singlet Cooper pairing in ceramic materials. We shall focus on this type of pairing.

Within the Ginzburg–Landau formalism the normal metal–superconductor phase transition may be described by the scalar complex order parameter $\Psi(\vec{r})$ which is the pair wave function. In momentum-space representation, $\Psi(\vec{k}) \propto \langle a_{\vec{k}\uparrow} a_{-\vec{k}\downarrow} \rangle$ and is related to the gap function $\Delta_{\vec{k}}$ through $\Psi(\vec{k}) = \Delta_{\vec{k}}/2E_{\vec{k}}$, where $E_{\vec{k}}$ is the quasiparticle excitation energy. The energy gap $\Delta_{\vec{k}}$ can serve as a well defined superconducting order parameter or as a measure of long-range phase coherence in the pair state. Its symmetry can be experimentally determined, even without detailed knowledge about the microscopic origin of superconductivity [15].

Since the transition to the superconducting state is second order it should be accompanied with a continuous symmetry breaking. The symmetry group $\mathscr{H}$ describing the pair state must be a subgroup of the group $\mathscr{G}$ describing the normal state, i.e. $\mathscr{H} \subset \mathscr{G}$ [73]. Considering pairing in a crystal one has $\mathscr{G} = \mathrm{G} \times \mathrm{R} \times \mathrm{I} \times \mathrm{T} \times \mathrm{U}(1)$, where G is the finite crystallographic point group, R the symmetry group of spin rotation, I the space inversion operation, T the time-reversal symmetry operation and U(1) the one-dimensional global gauge symmetry. For BCS superconductors the gauge symmetry U(1) is broken in the superconducting state due to the existence of off-diagonal long-range order. In an unconventional superconductor, in addition to U(1) one or more symmetries may be broken at T_c. Since spin–orbit interaction in ceramic superconductors is rather weak the pair wave function should be either singlet (spin $S = 0$, $\Psi(-\vec{k}) = \Psi(\vec{k})$) or triplet ($S = 1$, $\Psi(-\vec{k}) = -\Psi(\vec{k})$).

The mixed state like $a\Psi^s + b\Psi^t$ is forbidden. Due to the spatial inversion the singlet pair wave function does not change under the inversion operation ($I\Psi^s = \Psi^s$) whereas the triplet one changes its sign ($I\Psi^t = -\Psi^t$).

Point group classification of pair states in cuprate superconductors has been extensively studied [66,74–79]. They are divided into two groups: tetragonal crystal lattice with point-group symmetry D_{4h} and orthorhombic crystal lattice with point-group symmetry D_{2h}. $La_{2-x}Sr_xCuO_4$, $Tl_2Ba_2CaCu_2O_8$, $HgBa_2CaCuO_4$ and some YBa_2Cu_3 compounds belong to the first group whereas $YBa_2Cu_3O_{7-\delta}$ and $Bi_2Sr_2CaCu_2O_8$ possess D_{2h} symmetry. All possible pair wave functions of D_{4h} and D_{2h} groups are given in [76]. It should be noted that superconductivity of cuprates basically originates from the CuO_2 square/rectangular layers. Therefore we focus on the symmetry of possible pair states on the square lattice which is characterized by point-group symmetry C_{4v}. The list of spin-singlet even parity pair states for the tetragonal point group C_{4v} is given in Table 2. All representations A_{1g}, A_{2g}, B_{1g} and B_{2g} are one-dimensional.

Since there is strong experimental evidence for $d_{x^2-y^2}$ symmetry [80,15] in the high-temperature superconductors (see below) we will concentrate our study on this type of symmetry. Neglecting the possible orthorhombic distortion the pair wave function is described by B_{1g} representation of C_{4v} or D_{4h} group. In momentum space the pair wave function is

$$\Psi(\vec{k}) = \langle c_{\vec{k}\uparrow} c_{-\vec{k}\downarrow} \rangle = \cos k_x - \cos k_y \ . \tag{3.4}$$

The schematic description of the pair wave function of s and $d_{x^2-y^2}$ symmetry is shown in Fig. 13. The anisotropic function $\cos k_x - \cos k_y$ has the same symmetry property in C_{4v} as $k_x^2 - k_y^2$. For this

Table 2
Even-parity pair states allowed by C_{4v} symmetry

Name	State	Gap function $\Delta(\vec{k})$	Nodes
s-wave	$^1A_{1g}$	1	None
g	$^1A_{2g}$	$k_x k_y (k_x^2 - k_y^2)$	Line
$d_{x^2-y^2}$	$^1B_{1g}$	$k_x^2 - k_y^2$	Line
d_{xy}	$^1B_{2g}$	$k_x k_y$	Line

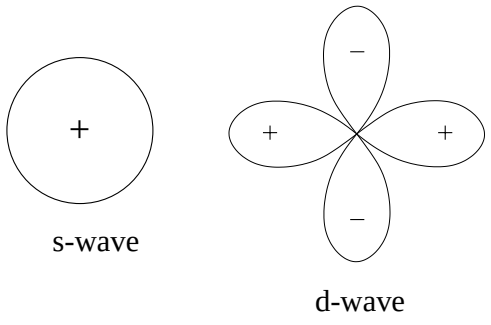

Fig. 13. Schematic description of s- and $d_{x^2-y^2}$-wave functions. The order parameter may be positive (+) or negative (−).

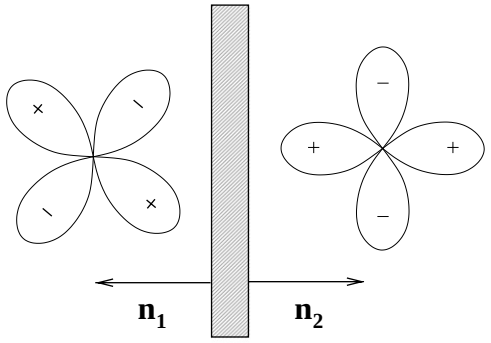

Fig. 14. Josephson junction between two $d_{x^2-y^2}$-wave superconductors. Vectors $\vec{n}_1$ and $\vec{n}_2$ defined on the basis of local crystal axes are normal to the interface.

reason, this state is called the d-wave with the angular momentum $L=2$, although the classification with respect to angular momentum has no real meaning under the discrete crystal field symmetry. Since function (3.4) is described by one-dimensional representation, the time-reversal symmetry can not be broken at T_c. Breaking of this symmetry is possible only for multi-dimensional representations [81].

We now consider the phenomenological theory of the Josephson effect in the case of a junction between two unconventional superconductors based on symmetry arguments. So far as $d_{x^2-y^2}$-wave corresponds to one-dimensional representation B_{1g} their complex order parameters η_1 and η_2 should be one-component

$$\eta_1 = |\eta_1| e^{i\phi_1}, \quad \eta_2 = |\eta_2| e^{i\phi_2} \ . \tag{3.5}$$

An intensive discussion of the experimental evidence for XY-universality class identifying the order parameter as a complex scalar belonging to a one-dimensional irreducible representation may be found in Ref. [82].

The free energy of two subsystems (see Fig. 14) joined by a junction is determined by the expression [10,83]

$$\begin{aligned}
&\mathscr{F} = \mathscr{F}_1 + \mathscr{F}_2 + \mathscr{F}_{12} \ , \\
&\mathscr{F}_i = \int_{\vec{r}\vec{n}_i > 0} d\vec{r}\ F_i (i = 1,2) \ , \\
&F_i = \alpha_0 \left(\frac{T - T_c}{T_c} \right) |\eta_i|^2 + \frac{\beta}{2} |\eta_i|^4 + K_{i1} (|D_x \eta_i|^2 + |D_y \eta_i|^2) + K_{i2} |D_z \eta_i|^2 + \frac{B^2}{8\pi} \ , \\
&\mathscr{F}_{12} = \oint dS\, t_0 g_1(\vec{n}_1) g_2(\vec{n}_2) (\eta_1^* \eta_2 + \eta_1 \eta_2^*) \ .
\end{aligned} \tag{3.6}$$

Here $\alpha_0, \beta, K_{i,j} (i,j = 1,2)$ and t_0 are phenomenological parameters; outward normal to the junction surface vectors $\vec{n}_i$ ($\vec{n}_1 = -\vec{n}_2$) are defined in the basis of local crystal axes; $D_{x,y,z}$ are the components of the gauge-invariant gradient $\vec{D} = (\nabla - 2\pi i \vec{A}/\Phi_0)$, where $\vec{A}$ is the vector potential ($\vec{B} = \nabla \times \vec{A}$).

$\mathscr{F}_1$ and $\mathscr{F}_2$ are scalar under the operations of the complete symmetry of the system $\mathscr{G}$ including the crystal symmetry D_{4h} (or C_{4v}), time reversal, spin rotation and gauge symmetry [84,75,76]. The interface term $\mathscr{F}_{12}$ was chosen in the lowest order and so that it generates the correct boundary conditions [63,75,85,84]. Functions $g_1(\vec{n}_1)$ and $g_2(\vec{n}_2)$ should be invariant under all operations of the symmetry group of the respective half-space. This condition is satisfied if we choose them to have the same symmetry properties as the corresponding order parameters. For the $d_{x^2-y^2}$ we have

$$g_{\rm i}(\vec{n}_{\rm i}) = n_{ix}^2 - n_{iy}^2 \sim \cos n_{ix} - \cos n_{iy} \ (i = 1, 2) \ . \tag{3.7}$$

Varying the gradient term of Eq. (3.6) with respect to $\vec{A}$, we obtain the current density in the left and right half-spaces

$$\vec{j}_1 = -c\frac{\delta\mathscr{F}_{1,\rm grad}}{\delta\vec{A}} = -\frac{2\pi c}{\Phi_0} Re\eta_1^*[K_{11}(D_x + D_y) + K_{12}D_z]\eta_1 \ ,$$

$$\vec{j}_2 = -c\frac{\delta\mathscr{F}_{2,\rm grad}}{\delta\vec{A}} = -\frac{2\pi c}{\Phi_0} Re\eta_2^*[K_{21}(D_x + D_y) + K_{22}D_z]\eta_2 \ . \tag{3.8}$$

The boundary conditions for the Ginzburg–Landau equations at the junction interface are obtained by varying the full free energy (3.6) with respect to η_1^* and η_2^*

$$\mathrm{i}[K_{11}(n_{1x}D_x + n_{1y}D_y) + K_{12}n_{1z}D_z]\eta_1|_{\rm S} = -t_0 g_1(\vec{n}_1)g_2(\vec{n}_2)\eta_2|_{\rm S} \ ,$$

$$\mathrm{i}[K_{21}(n_{2x}D_x + n_{2y}D_y) + K_{22}n_{2z}D_z]\eta_2|_{\rm S} = -t_0 g_1(\vec{n}_1)g_2(\vec{n}_2)\eta_1|_{\rm S} \ . \tag{3.9}$$

From Eqs. (3.8) and (3.9) we have the current density through the Josephson junction

$$\vec{j} = (\vec{j}_1 + \vec{j}_2)\vec{n}_1|_S = J_{\rm c}\sin(\phi_1 - \phi_2) \ ,$$

$$J_{\rm c} = \frac{4\pi c t_0}{\Phi_0} g_1(\vec{n}_1)g_2(\vec{n}_2)|\eta_1\|\eta_2| \ . \tag{3.10}$$

Taking Eqs. (3.7) and (3.10) into account one can see that the critical current $J_{\rm c} \propto (n_{1x}^2 - n_{2x}^2)(n_{1y}^2 - n_{2y}^2)$ may be positive or negative depending on orientation of vectors $\vec{n}_1$ and $\vec{n}_2$. A negative $J_{\rm c}$ is equivalent to an intrinsic phase shift of π in the junction. Because $g_{\rm i}(\vec{n}_{\rm i})$ has essentially the same symmetry as the order parameters, the Josephson effect allows one to probe the phase of the pair wave function. The existence of π junctions may serve as an indicator for the d-wave superconductivity.

3.3. Experimental verification of d-wave pairing

So far as the d-wave pairing may play a key role in understanding the PME in ceramic superconductors, in this part we discuss experiments which support its existence. Those experiments are divided into two classes: phase insensitive and phase sensitive ones [15].

Phase insensitive experiments. There are two kinds of phase-insensitive experiments. One of them probes the gap features at the Fermi surface. It includes, in particular, the angle-resolved [86], tunnel [87], Raman scattering [88] and point-contact [89] spectroscopies. The results obtained by these techniques for a number of specific hole-doped oxides, are usually interpreted as manifestation

of the d-wave pairing although it is impossible in some cases to distinguish it from the anisotropic s-wave symmetry [15]. Here we focus on the second group of phase-insensitive experiments based on the fact that the low temperature behavior of thermodynamic and transport properties of d-wave superconductors is governed not by exponential as in the BCS theory but by power laws.

At low temperatures the specific heat of BCS superconductors behaves as $C_s(T \to 0) \sim T^{-3/2} \exp(-\Delta_0/T)$, where Δ_0 is the isotropic s-gap at $T = 0$ [7]. Simple calculations [90] show, however, that for the hexagonal $d_{x^2-y^2}$ superconductors $C_s \sim T^2$ due to lines of nodes on the Fermi surface. There is some controversy about experiments of different groups. The $C_s \sim T^3$ was found in Bi-compounds [91] whereas the linear behavior $C_s \sim T$ was reported by other investigators [92–94]. Recent experiments on single crystals [95,96] and ceramic samples [97] of YBCO show, however, that $C_s \sim T^2$.

In the presence of the magnetic field the quadratic temperature dependence rolls over to a T [98], i.e. $C_s = k\gamma_n T\sqrt{H/H_{c2}}$ for $T/T_c \ll \sqrt{H/H_{c2}}$, where k is a constant of order one and γ_n is the coefficient of the linear-T term in normal state [7]. This linear-T and $H^{1/2}$ dependence was confirmed by experiments [96,97,99]. Furthermore Revaz et al. [100] found that the anisotropic component of the field-dependent specific heat $C_s(T, H\|c) - C_s(T, H \perp c)$ of single crystal YBCO obeyed a scaling relation predicted for a superconductor with a line of nodes [101,102].

In the low temperature limit the London penetration depth $\lambda_L(T)$ of the conventional superconductors approaches its zero value $\lambda_L(0)$ exponentially: $\delta\lambda_L(T) = (\lambda_L(T) - \lambda_L(0))/\lambda_L(0) \sim T^{-1/2} \exp(-\Delta_0/T)$. The theory of $d_{x^2-y^2}$ superconductivity gives $\delta\lambda_L(T) \sim T$ for pure materials and $\delta\lambda_L(T) \sim T^2$ for dirty ones [103,104]. For nominally clean YBCO samples linear dependence was observed [105] whereas for Zn- and Ni-doped as well as nonhomogeneous crystals the quadratic behavior was reported [105–111]. Although these results agree with the d-wave symmetry of the gap function, they cannot distinguish between the d- and s-wave because the linear dependence of $\delta\lambda_L(T)$ could also arise from promixity effects between alternating s-wave superconducting and normal layers in the cuprates [112,113].

The another way to probe the symmetry of the order parameter is to study the low-T behavior of the thermal conductivity of electrons $\kappa_e(T)$. $\kappa_e(T) \sim T^{-1}\exp(-\Delta_0/T)$ for the BCS superconductors but it should obey the Wiedemann–Franz law, $\kappa_e(T) \sim T$, for the $d_{x^2-y^2}$ materials [114,115]. This linear dependence was shown to be insensitive to the impurity scattering [115]. Unfortunately, it is difficult to extract the thermal conductivity component $\kappa_e(T)$ from experiments due to the complex mutual action of electrons, phonons and impurities [114,116]. Nevertheless, the existing experiments confirm the Wiedemann–Franz law in Zn-doped YBCO [117–119], below $T^* = 200$ mK in $Bi_2Sr_2Ca(Cu_{1-x}Ni_x)_2O_8$ [120] and in BiSrCaCuO [121].

As to the ultrasonic attenuation coefficient α_s in superconducting state with anisotropic pairing, the theory [122] predicted $\alpha_s \sim T$ at low temperatures. Experiments performed for $YBa_2Cu_3O_{7-x}$ [123,124] and $La_{1.8}Sr_{0.2}CuO_{4-x}$ showed that $\alpha_s \sim T^n$ with a large scatter of exponent n for each substance.

Finally, as $T \to 0$, the nuclear spin-lattice relaxation rate T_1^{-1} of the $d_{x^2-y^2}$ superconductors was shown to scale with temperature as $T_1^{-1} \sim T^3$ [104]. Such a temperature dependence was confirmed by experiments [104,125].

It should be noted that low temperature asymptotics of various thermodynamic and transport properties of s-wave superconductors can roll over power-laws [126,127] provided the gap values are widely distributed due to structure domains, charge stripes, charge-density waves or other mesoscopic

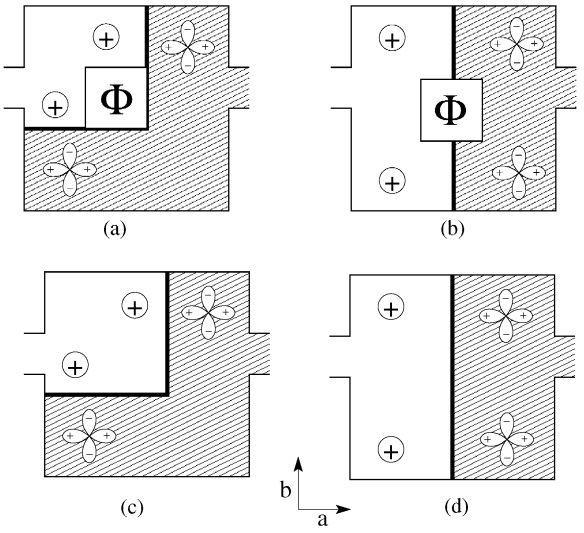

Fig. 15. Experimental geometry for the SQUID and single junction experiments (see Ref. [128,137]): (a) Configuration of the corner SQUID interferometer experiment used to determine the relative phase between orthogonal crystal directions a and b. (b) The edge SQUID used as a control sample, in which both junctions are on the same crystal face. (c) The corner configuration for a single junction experiment. (d) The same as in (c) but for the edge geometry.

inhomogeneities. So the interpretation of the d-wave symmetry based only on the low-T asymptotics remains ambiguous.

Phase sensitive experiments. Recently, a number of phase-sensitive experimental techniques has been developed to determine the order parameter symmetry of cuprate superconductors [80,104,66,15] starting from the pioneering work of Wollman et al. [128]. The key idea is relying on the sign changes in the Josephson critical current I_c as proposed first by Geshkenbein and Larkin [63] as a test for axial p-wave pairing symmetry in the heavy fermion superconductors.

In the "corner SQUID" design shown in Fig. 15(a) Josephson junctions are made between s-wave Pb thin films and two orthogonally oriented ac and bc plane faces of single crystal YBCO [128]. If YBCO is a d-wave superconductor, then, according to Eq. (3.10), there should be a π phase shift between weak links on adjacent faces of the crystal. For the "edge SQUID" geometry in Fig. 15(b) no phase shift is expected because both two junctions are on the same crystal face.

We consider the dc "corner" SQUID with junction critical currents I_a and I_b. Then a bias current through the SQUID is the sum of the currents passed by junctions a and b

$$I = I_a \sin\phi_a + I_b \sin\phi_b \ . \tag{3.11}$$

On the other hand, the quantum phase coherence around the SQUID loop forces the constraint on the gauge-invariant phase differences across the junctions on the ca and cb faces of crystal [7,128], namely,

$$\phi_a - \phi_b + 2\pi\left(\frac{L_a I_a}{\Phi_0} - \frac{L_b I_b}{\Phi_0} + \frac{\Phi_{\rm ext}}{\Phi_0}\right) + \delta_{ab} = 2\pi n \ , \tag{3.12}$$

where L_a and L_b are the effective self-inductances of the two arms of the ring, n is integer, δ_{ab} accounts for the intrinsic phase shift inside the YBCO crystal between pairs tunneling into the crystal in the a and c directions. One can expect that $\delta_{ab}=\pi$ and $\delta_{ab}=0$ for the "corner" and "edge SQUID", respectively.

In order to find the maximum current one can substitute ϕ_b from Eq. (3.12) into Eq. (3.11) and then find the maximum of I with respect to ϕ_a. For a symmetric dc SQUID with equal junction critical currents $I_a=I_b=I_0$, in the limit of zero loop inductance, simple algebra gives the following expression for the field dependence of the maximum supercurrent

$$I_c(\Phi_{ext})=2I_0\left|\cos\left(\pi\frac{\Phi_{ext}}{\Phi_0}+\frac{\delta_{ab}}{2}\right)\right| . \tag{3.13}$$

For finite values of self-inductances the modulation depth of the critical current is reduced because the circulating currents generate a flux contribution in the ring [128]. From the last equation it is clear that if YBCO has s-wave symmetry then $\delta_{ab}=0$ and the circuit will behave as an ordinary dc SQUID [7]: I_c has a maximum at $\Phi_{ext}=0$. Such a behavior should be also exhibited by "edge SQUID" regardless to the type of symmetry of pairing in the YBCO material. In contrast, for d-wave symmetry the "corner SQUID" should have $\delta_{ab}=\pi$ and the critical supercurrent would display a minimum at zero external flux. This important prediction was confirmed by the experiments of Wollman et al. [128].

It should be noted that there are several complicating factors in interpretation of results obtained by the SQUID experiment of Wollman et al. [80,15]. Since YBCO has an orthorhombic crystal structure, it has a tendency to form a twin boundaries at which a and b lattice constants are interchanged. This would randomlize the phase that these experiments depend on. However, there are both experimental [129,130] and theoretical [80] showed that the order parameter maintains its orientation across twin boundaries and forms a single domain even in twined samples. Moreover, experiments on detwined samples [131,80] gave consistent results indicating that the $d_{x^2-y^2}$ component of the order parameter has the same phase across twin boundary.

Klemm was concerned [132] about the role of the corners in dc SQUID measurements of the phase anisotropy of YBCO crystals [128]. Since flux trapping, demagnetization and field-focusing effects can be strongly dependent on the sample geometry he argued that the π phase shifts seen between the corner and edge SQUIDS could result simply from their geometry differences, even for s-wave superconductors. This point of view was criticized by Wollman et al. [133] showing that corners play no significant role.

An another concern is the flux trapping near the SQUID. This flux can be coupled to the SQUID loop and create a shift in the flux modulation pattern that is indistinguishable from the intrinsic phase shift. In order to avoid this effect one can cool the SQUID many times to get the lowest-energy state, which will be one with no flux trap. Magnetic imaging of the ac and bc plane faces of cuprate superconductors [134,135] shows that there can be vortices trapped between the planes, even when they are cooled in a very small field. Such trapped vortices could affect the measured critical-current vs. applied field characteristics of the SQUID's but not substantially.

Since Eq. (3.13) was obtained for a symmetric ($I_a=I_b$) SQUID with zero self-inductance. Asymmetries between critical current in the junctions and the nonzero loop inductance can modify the critical current pattern significantly. Of particular importance here is a shift in the pattern, since this could mimic or obscure phase shifts arising from the pairing symmetry. Since the asymmetry-induced

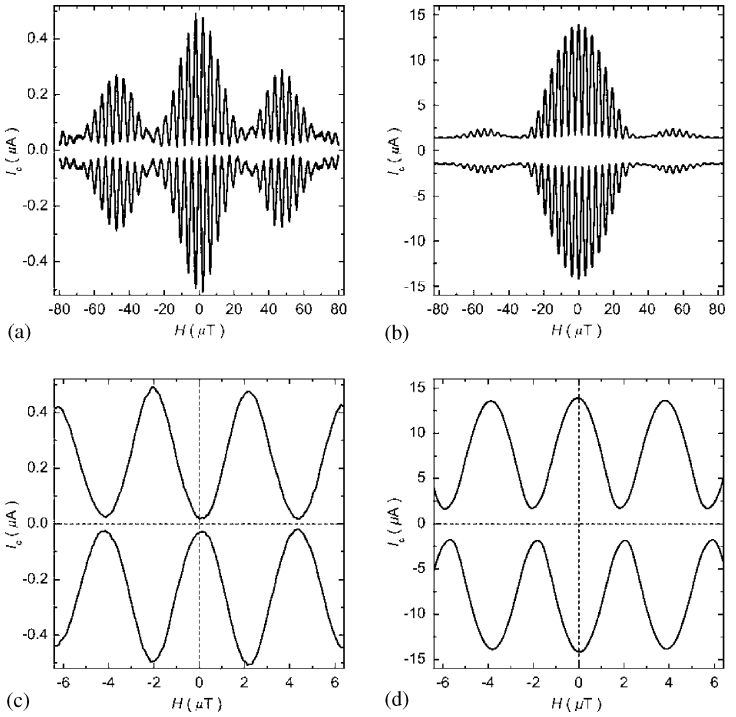

Fig. 16. Field dependence of the critical current of the π-SQUID (a) and (b) and of the standard SQUID (c) and (d) at $T = 77$. The dip at zero field in the corner SQUID is evidence for $d_{x^2-y^2}$ pairing symmetry in the YBCO. After Schulz et al. [136].

shifts of the $I_c(\Phi_{ext})$ pattern are proportional to the screening, it is vital to design SQUIDs with negligible inductance. Such a problem was solved by Schulz et al. [136] using YBCO thin films epitaxially grown on bicrystal and tetracrystal substrates. They obtained, as one can see from Fig. 16, nearly ideal dependences of the critical current on applied field, with a minimum at $H = 0$ for the π-ring SQUID, as expected for a d-wave superconductor in the tetracrystal geometry used. A more detailed discussion on the SQUID technique was given in Ref. [15].

We now discuss single-junction modulation experiments [137] the geometry of which is shown in Fig. 15c and d for the corner and the edge case, respectively. These experiments have a distinct advantage over the SQUID ones since they are less sensitive to flux trapping and sample asymmetry. The basic idea is relied on the well known effect of an applied magnetic field on the critical current of Josephson tunnel junctions [7,138]. The magnetic field penetrating though the barrier region transverse to the tunneling direction forces a gradient in the phase of the order parameter across the width of the junction, resulting in a variation of the local current density and a reduction in the total critical current. If the junction is rectangular and homogeneous with the field applied parallel to one edge of the rectangle, and if the junction size is much smaller than the Josephson penetration depth, the critical current has the standard Fraunhofer form [7,138]

$$I_c(\Phi) = I_0 \left| \frac{\sin(\pi\Phi/\Phi_0)}{\pi\Phi/\Phi_0} \right| \tag{3.14}$$

which is familiar from single-lit optical diffraction, Φ is the flux threading the junction. The Fraunhofer pattern given by the last equation is valid for an edge junction with arbitrary pairing symmetry and for a corner junction with *xisd*-wave superconductors. Similar to the edge SQUID, this pattern has a maximum at $\Phi = 0$.

In the case of the corner junction, the order parameter in the a and b directions would be of opposite sign, modifying the diffraction pattern. In a symmetric junction with equal geometries on the a and b faces, the critical current modulates according to [137,139]

$$I_c(\Phi) = I_0 \left| \frac{\sin^2(\pi\Phi/2\Phi_0)}{\pi\Phi/2\Phi_0} \right|. \tag{3.15}$$

Contrary to the edge junction, I_c vanishes at zero applied field as the current through two orthogonal faces cancels exactly.

The field dependence the critical current of the edge and corner junctions obtained by Wollman et al. [137] is shown in Fig. 17. Similar patterns were reported by different groups [139–141]. The pattern shown in Fig. 17b) for d-wave corner junction does not agree closely with the ideal expression (3.15). It may be attributed, as shown by theoretical predictions, to the flux trap in the sample [142] or by the size of the junction [143]. So the experiments on the modulation pattern

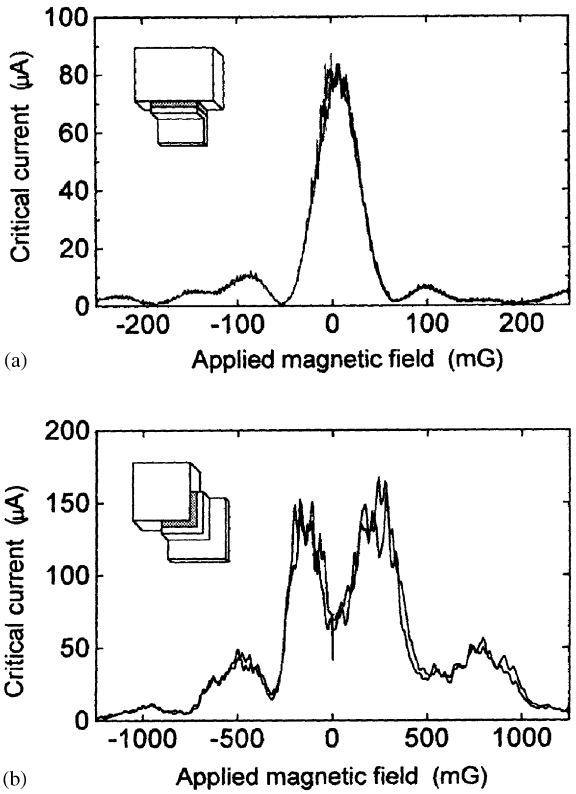

Fig. 17. Field dependence of the critical current of the edge junction (a) and of the corner junction (b). The minimum at zero field in the corner edge is evidence for $d_{x^2-y^2}$ pairing symmetry in the YBCO. After Wollman et al. [137].

of the critical current in the single Josephson junction support the existence of the d-wave pairing symmetry.

To summarize, the phase sensitive, along with phase insensitive experiments give strong evidence in favour of predominantly d-wave pairing symmetry in a number of cuprates. The identification of this type of symmetry is based purely on very general principles of group theory and the macroscopic quantum coherence phenomena of pair tunneling and flux quantization. It does not, therefore, necessarily specify a mechanism for high temperature superconductivity.

4. Paramagnetic Meissner effect in d-wave superconductors

This section is focused on the d-wave mechanism of the PME in the framework of the single-loop and loop models.

4.1. One-loop model

As shown above, the phase across a π-junction between two d-wave superconductors is shifted by π and the corresponding energy is proportional to $\cos(\phi_1 - \phi_2 + \pi)$. The system tries to minimize its energy by setting the phase difference $(\phi_1 - \phi_2)$ equal to π. Thus, there is no way to measure this phase shift directly because it merely corresponds to the phase change in one of the two superconductors, say, $\phi_1 \to \phi_1 + \pi$. This transformation is equivalent, as one can see from Eq. (3.7), to the exchange of the x and y coordinates in superconductor (1). In other words, the connection of two d-wave superconductors by a single π-junction does not, by itself, lead to any special observable effects. In this sense, whether a junction is 0- or π-junction is just a matter of convention.

Physically interesting consequences are, however, expected to arise if an odd number of π-junctions are connected in a loop [10]. A cartoon of a contact from three junctions is shown in Fig. 18a. One can choose the coordinates x and y in two segments to convert two π-junctions into two 0-junctions but there is no transformation to remove the remaining π-junction without putting one of the two 0-junctions back to a π-junction. After all redefinitions of the crystal axis the multi-connected loop

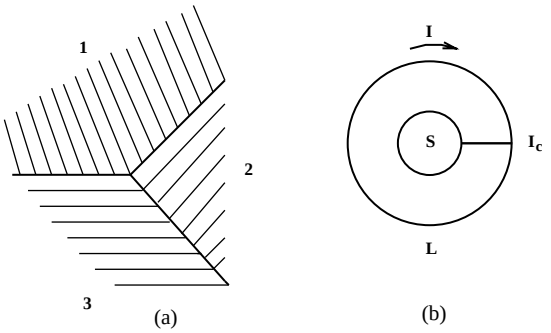

Fig. 18. (a) Schematic plot of a contact of three grains of superconductors with unconventional pairing with different orientation of their local crystal axis. These grains form a frustrated loop with nonzero spontaneous current in the ground state. (b) Single π-junction loop with the self-inductance L, area S and critical current I_c.

has at least one π-junction. Since there is no way to minimize the energy of all junctions and at the same time to keep the phase of the order parameter constant in each segment, such a loop is, in analogy with spin glass physics [144], frustrated. In what follows any single loop is supposed to contain effectively only one π junction as shown in Fig. 18b or one 0 junction which is not frustrated.

Assuming that the loop has self-inductance L and the current I flowing in it is small compared to the critical current $I_c > 0$, the energy is given by the following form [9,10]:

$$F(\Phi, \Phi_{\text{ext}}) = \frac{1}{2L}(\Phi - \Phi^{\text{ext}})^2 - \frac{I_c \Phi_0}{2\pi} \cos\left(2\pi \frac{\Phi}{\Phi_0} + \delta\right) . \tag{4.1}$$

Here Φ^{ext} is the created by the external field flux threading through the loop, $\Phi = LI$ and the phase shift δ is equal to 0 and π for 0- and π-junction, respectively. The first term in Eq. (4.1) corresponds to the screening whereas the second term is standard for an Josephson junction. The important question is if the spontaneous magnetic moment (flux or supercurrent) occurs in zero external field. The answer to this question may be obtained by finding minimum of energy (4.1).

In the absence of the external field the dimensionless energy $\tilde{F}(\Phi/\Phi_0)$ reads as

$$\tilde{F}(\Phi/\Phi_0) = \frac{2L}{\Phi_0^2} F = \left(\frac{\Phi}{\Phi_0}\right)^2 - \frac{\tilde{L}}{2\pi^2} \cos\left(2\pi \frac{\Phi}{\Phi_0} + \delta\right) . \tag{4.2}$$

Here the dimensionless self-inductance $\tilde{L}$ is equal to

$$\tilde{L} = \frac{2\pi I_c L}{\Phi_0} . \tag{4.3}$$

It is easy to show that at $\Phi/\Phi_0 = 0$ the energy has extremum and its second derivative with respect to Φ/Φ_0 has the simple form

$$\tilde{F}''(0) = 2(1 \pm \tilde{L}) , \tag{4.4}$$

where the sign plus and minus corresponds to the 0- and π-junction, respectively. For an unfrustrated loop $\tilde{F}''(0) > 0$ and the state without the supercurrent should be stable and the PME is not, as expected, possible. In the case of the π-junction the energy has minimum $\Phi/\Phi_0 = 0$ ($\tilde{F}''(0) > 0$) for $\tilde{L} < 1$ and *maximum* ($\tilde{F}''(0) < 0$) for $\tilde{L} > 1$. We come to a very interesting result: the energy of a frustrated loop has minimum at $\Phi \neq 0$ provided $\tilde{L} > 1$. It is demonstrated in Fig. 19. Thus, above the critical value $\tilde{L}_c = 1$ the spontaneous magnetic moment M_{sp} appears in the single π-junction loop leading to the PME.

In the $\tilde{L} \to \infty$ limit M_{sp} may be determined exactly. In this case the second term in (4.1) dominates and the energy has a ladder of minima at $\Phi = n\Phi_0$ and $\Phi = (n + \frac{1}{2})\Phi_0$ (n is integer number) for 0-junction and π-junction, respectively. The spontaneous magnetization corresponding to the global minimum with $n = 0$ is equal to $M_{\text{sp}} = \Phi_0/8\pi S$, where S is the loop area.

Since the energy minima of the single π-junction are located near $\Phi = (n + \frac{1}{2})\Phi_0$ the PME is, in some sense, the manifestation of the common half-integer flux quantum effect [15]. The screening plays a key role in the observation of the paramagnetic response. Taking into account the temperature dependence of critical current I_c and using the one-loop model (4.1), Sigrist and Rice were able to reproduce the paramagnetic behavior in the FC regime [9,10]. In accord with experiments the paramagnetic signal is suppressed as the external field is increased.

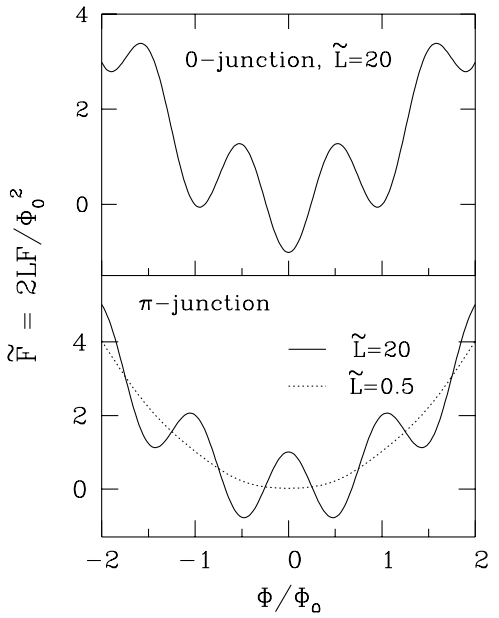

Fig. 19. Flux dependence of the dimensionless free energy $\tilde{F}$ of the one-loop model. For the 0-junction with $\tilde{L} = 20$ (upper panel) and π-junction with $\tilde{L} = 0.5 < 1$ (dotted line in lower panel) the function $\tilde{F}$ has minimum at $\Phi/\Phi_0 = 0$. For a π-junction with $\tilde{L} = 20 > 1$ (solid line in lower panel) the minimum is located at $\Phi/\Phi_0 \neq 0$ and the paramagnetic response becomes possible.

4.2. Multi-loop model

Although the single-loop model considered in the previous chapter predicts the appearance of the PME, it fails to capture many cooperative phenomena such as the aging, the compensation effect, a possibility of the existence of a new chiral glass phase *etc* in granular materials. This shortcoming may be amended in the multi-loop model [12,145] where the interaction between loops is taken into account.

4.2.1. Hamiltonian

Suppose that weak links connecting the neighboring grains are distributed sufficiently dense, so that the system can be viewed as an infinite network of Josephson junctions which are not decomposed into finite clusters. We model such ceramic superconductors by a hypercubic (two- or three-dimensional) lattice model of a Josephson junction arrays with finite self-inductance. Neglecting charging effects of the grain the Hamiltonian is given by [12]

$$\mathscr{H} = -\sum_{\langle ij\rangle} J_{ij}\cos\left(\phi_{\mathrm{i}} - \phi_j - A_{ij}\right) + \frac{1}{2L}\sum_{\mathrm{p}}\left(\Phi_{\mathrm{p}} - \Phi_{\mathrm{p}}^{\mathrm{ext}}\right)^2 ,$$

$$\Phi_{\mathrm{p}} = \frac{\Phi_0}{2\pi}\sum_{\langle ij\rangle}^{p} A_{ij}, A_{ij} = \frac{2\pi}{\Phi_0}\int_{\mathrm{i}}^{j}\vec{A}(\vec{r})\mathrm{d}\vec{r} , \tag{4.5}$$

where ϕ_i is the phase of the condensate of the grain at the ith site of a simple hypercubic lattice, $\vec{A}$ is the fluctuating gauge potential at each link of the lattice, J_{ij} denotes the Josephson coupling between the ith and jth grains, and L is the self-inductance of a loop. The effect of screening currents inside grains is not considered explicitly, since for large length scales they simply lead to a Hamiltonian $\mathscr{H}$ with an effective self-inductance L [146]. The first sum is taken over all nearest-neighbor pairs and the second sum is taken over all elementary plaquettes on the lattice. Fluctuating variables to be summed over are the phase variables, ϕ_i, at each site and the gauge variables, A_{ij}, at each link. Φ_p is the total magnetic flux threading through the pth plaquette, whereas Φ_p^{ext} is the flux due to an external magnetic field applied along the z-direction,

$$\Phi_p^{ext} = \begin{cases} HS & \text{if } p \text{ is on the } \langle xy \rangle \text{ plane}, \\ 0 & \text{otherwise}, \end{cases} \tag{4.6}$$

where S denotes the area of an elementary plaquette. Hamiltonian (4.5) is an extension of the single-loop energy (4.1) to the interacting loops case.

In the s-wave ceramics, sign of the Josephson coupling is always positive ($J_{ij} > 0$), while in d-wave ceramics it could be either positive (0-junction) or negative (π-junction) depending on the relative direction of the junction and the crystal grains on both sides. In d-wave case, the sign of J_{ij} is expected to appear randomly since the spatial orientation of each crystal grain would be random. It was also suggested [147] that the Josephson junction between d-wave superconductors under certain circumstances (e.g., near the interface) might have an energy minimum at some fractional value, neither at 0 or π, as a result of a spontaneous time-reversal symmetry breaking at the junction. Such a possibility is not discussed in this review.

The model with uniform ferromagnetic couplings ($J_{ij} = J$) studied by Dasgupta and Halperin [148] exhibits a standard normal-superconductor transition. Here we deal with two types of bond distributions. For d-wave ceramics J_{ij} is assumed to take the value $-J$ (π-junction) with probability c and $+J$ (0-junction) with probability $(1 - c)$ [12]. In the s-wave model J_{ij} is always positive ("ferromagnetic" interaction) but distributed uniformly between 0 and 2π [145].

In the case of d-wave superconductors the frustration due to competition between "ferromagnetic" and "antiferromagnetic" interactions [144] causes the nonzero spontaneous magnetic moment provided c exceeds the percolation threshold. The global PME becomes, therefore, possible. In the absence of an external field, the global minimum of the energy of the s-wave system corresponds to the configuration with zero supercurrents and the system displays a standard diamagnetism.

4.2.2. Critical self-inductance

In the single-loop model with one π-junction the dimensionless critical inductance above which the system shows the PME is equal to $\tilde{L} = 1$. The question we as now is does the interaction between frustrated loops change this critical value. For the multi-loop model (4.5) $\tilde{L}$ is also given by Eq. (4.3) with the critical current [145]

$$I_c = \frac{2\pi J}{\Phi_0} . \tag{4.7}$$

One can show (see Appendix A) that, contrary to the one-loop model, the critical inductance above which the PME is observable is equal to

$$\tilde{L} = 0 . \tag{4.8}$$

In the limit of small inductances the spontaneous flux of the multi-loop model is equal to [145]

$$\frac{\Phi}{\Phi_0} \approx \pm \frac{\tilde{L}}{2\sqrt{2}\pi} \quad \text{for } \tilde{L} \ll 1 \ . \tag{4.9}$$

The last expression shows that for small inductance, spontaneous flux remains nonzero but becomes small. In real ceramic samples one has an additional diamagnetic contribution from intragranular supercurrents neglected in the present model, a small paramagnetic contribution from the intergranular supercurrents may easily be masked. Therefore, in practice, moderately large inductance would be necessary to observe the paramagnetic behavior.

4.2.3. Simulation results

Total magnetization along the z-axis normalized per plaquette m is given by [12]

$$m = \frac{1}{N_p \Phi_0} \sum_{p \in \langle xy \rangle} (\Phi_p - \Phi_p^{ext}) \ , \tag{4.10}$$

where the sum is taken over all N_p plaquettes on the $\langle xy \rangle$ plane. The linear susceptibility χ (dimensionless in CGS units) may be calculated via fluctuation of the magnetization as follows

$$\chi = \frac{\pi J N_p}{k_B T \tilde{L}} [\langle m^2 \rangle - \langle m \rangle^2]_J - \frac{1}{4\pi} \ , \tag{4.11}$$

where $\langle \cdots \rangle$ and $[\ldots]_J$ represent a thermal average and a configurational average over the bond distribution, respectively. For conventional superconductors the first term in (4.11) vanishes at low temperatures and χ takes on a standard value $-1/4\pi$.

The temperature and field dependence of the FC and ZFC susceptibility was studied by Langevin dynamics [12] and by Monte Carlo simulations [145]. Both these methods give essentially the same results and we present those obtained by the latter approach.

As can be seen from Fig. 20, a paramagnetic behavior is shows up in FC regime in the field range $h \leqslant 1$ (roughly corresponding to $\Phi^{ext} \sim \Phi_0/4$), where the dimensionless field h is defined as [145]

$$h = \frac{2\pi S H}{\Phi_0} \ . \tag{4.12}$$

By contrast, χ_{ZFC} remains diamagnetic at low temperatures for any value of the dc fields studied.

From Fig. 20 it follows that the remanent magnetization $m_{rem} \approx m_{FC} - m_{ZFC}$ is positive, consistent with experiments on high-T_c ceramics [149,150]. This observation indicates the occurrence of flux trapping in the d-wave model.

The Monte Carlo simulations [145] showed that the PME is clearly visible for a very small inductance $\tilde{L} = 0.1$. This result compatible with the conclusion in the previous section that $\tilde{L}_c = 0$ for the multi-loop model.

Fig. 21 shows the temperature and field dependence of χ_{FC} and χ_{ZFC} of the s-wave system. We set the system size $l = 8$ and $\tilde{L} = 1$. As expected, the response is always diamagnetic. Furthermore, there is no appreciable difference between χ_{FC} and χ_{ZFC} for $h < 0.2$. Within the statistical errors m_{rm} turns out to be zero confirming that the flux does not get trapped inside a sample.

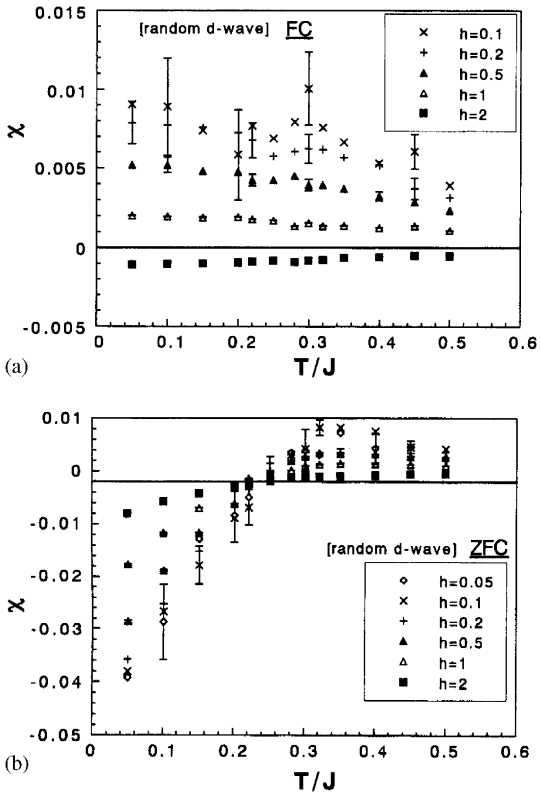

Fig. 20. The temperature dependence of the FC susceptibility (a) and of the ZFC susceptibility (b) of d-wave ceramics for several values of the external field. The lattice size is equal to $l=8$, $\tilde{L}=1$ and the concentration of π junctions $c=0.5$. After Kawamura and Li [145].

4.3. Other models

Using a Josephson junction model of special geometry [151] Auletta et al. [152] have shown that the PME is possible even without π-junctions. The similar conclusion was also made by other groups [46,47,153–155] for standard systems of 0-junctions (the effect of mutual inductances has been considered in [153,155]). The paramagnetic behavior can arise either in a d-wave sample or in a conventional sample of confined geometry. From this point of view, the PME observed in simulations of the 0-junction networks [46,47,152–155] may be due to the finite size effect or it is merely a metastable effect.

Recently, Khalil [20] assumed that near randomly distributed defects the localized superconducting states with different orbital moments could exist. The first-order transitions between these states below the critical temperature are accompanied by jumps of the magnetic moments. As a result, multiple-quanta vortices and spontaneous moments randomly distributed in the material matrix will be formed. This provides the explanation of the PME.

Authors of Ref. [156] proposed that a certain amount of local moments exist that are becoming partially aligned by an external field. Based on experimental data, these moments are estimated to

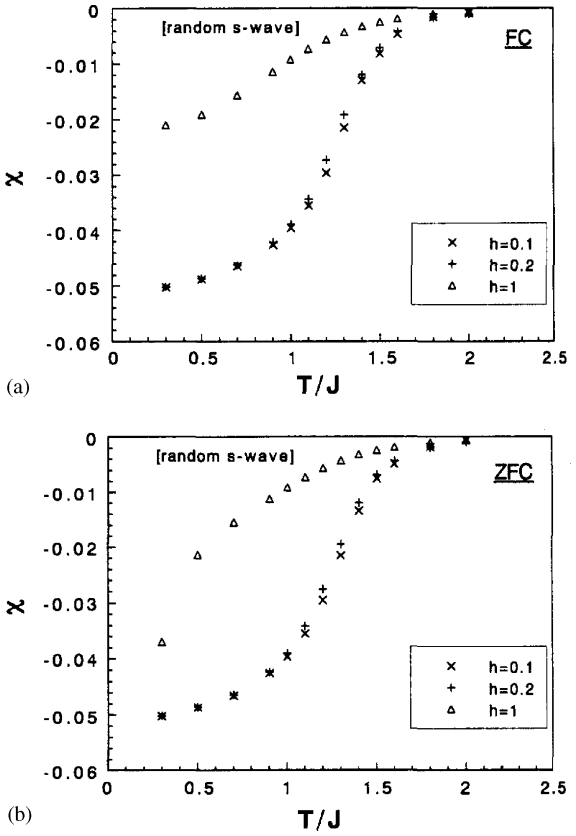

Fig. 21. The temperature dependence of the ZFC susceptibility (a) and of the ZFC susceptibility (b) of s-wave ceramics for several values of the external field. The lattice size is equal to $l = 8$ and $\tilde{L} = 1$. After Kawamura and Li [145].

be too small compared to the half flux quanta. They are cannot be, therefore, due to π-junctions but their nature remains unspecified.

The another interpretation [157] of the PME is based on the so called impurity mechanism [158] for high-T_c superconductivity. The validity of this heuristic argument remains ambiguous.

Finally, the PME was proposed to be related to the vortex pinning [2] at the Kosterlitz–Thouless transition. Since this transition is possible in two dimensions [159] it is not clear if the scenario of Svelindh et al. [2] is applied to three-dimensional systems.

5. Flux compression and paramagnetic Meissner effect

In this chapter we discuss the flux compression mechanism for the PME which is probably applied to conventional superconductors with s-wave type of pairing symmetry. There are two approaches to study the flux trapping in the confined geometry. One of them is based on the Bean critical model and was developed by Koshelev and Larkin [19]. The second approach [21] relied on the numerical

solution of the Ginzburg–Landay equations, predicts the paramagnetic response due to spontaneous magnetic moments in giant vortex states which occur below the third critical field.

5.1. Bean model

The PME observed in conventional superconductors [18] and in twined single crystals of $YBa_2Cu_3O_{7-\delta}$ suggests the possibility of alternative explanations without exotic d-wave pairing. One of such possibilities is based on the flux compression mechanism [19] using the Bean model [160] for the critical state. A possible origin of the existence of the spontaneous paramagnetic moment is flux trap caused by an inhomogeneous superconducting transition. If the edges of the sample becomes superconducting first due to, e.g., inhomogeneity of material (surface layers have a higher value of T_c compared to the bulk) or inhomogeneous cooling, then expulsion of vortices from this area opens a flux-free region near the edges. This gives rise to the flux capture inside the sample. Further cooling leads to a broading of the flux-free region and further compression of the flux due to, e.g., the vortex Nernst effect [161]. As the whole sample becomes superconducting the critical Bean state develops in the flux region. For a thin superconducting strip geometry (see Fig. 22) one can imagine this scenario as follows. The outer current mimics the diamagnetic shielding current, while the inner current models the paramagnetic pinning current. If the flux is trapped inside sample, then the flux created by the outer current should be completely compensated by the flux generated by the inner current in the flux free region. Since the field generated by currents flowing in the inner region changes sign, these currents give a smaller contribution to the total flux than do the currents flowing in the outer region [19]. This should be compensated by a larger magnitude of the inner paramagnetic currents, which gives rise to the paramagnetic moment.

We now give a qualitative description of the existence of the PME due to flux compression in a simple case of a thin superconducting slab of width $2w$ and thickness d situated in a transverse magnetic field [19] as shown in Fig. 22. The Bean state is assumed to be complete with the critical current j_c flowing in the strip of width $2b$ ($|x| < b < w$) surrounded by flux free region of width $w - b$ ($b < |x| < w$) (the incomplete Bean state was also discussed by Koshelev and Larkin [19]).

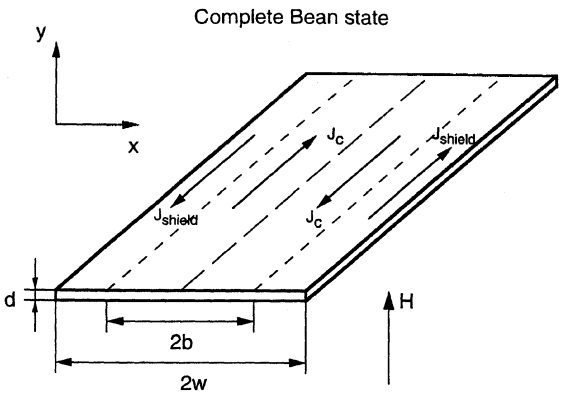

Fig. 22. Complete Bean critical state in a thin superconducting slab after field cooling. Reprinted from Koshelev and Larkin [19].

Then the tangential (H_x) and longitudinal (H_y) field components satisfy the following boundary conditions [19]

$$H_x = H_J \operatorname{sign}(x), \quad 0 < |x| < b \ ,$$
$$H_x = 0, \quad |x| > b \ ,$$
$$H_y = 0, \quad b < |x| < w \ ,$$
$$H_y = H_\infty, \quad r \to \infty \ , \tag{5.1}$$

where $2H_J = (4\pi/c)J_c, J_c = dj_c$. The first equation in (5.1) from the Gaussian theorem and the continuous boundary conditions for the tangential component of the field near the slab surface [162,163]. The second and third equations are valid for the flux-free region. The field distribution may be obtained from the Maxwell equations

$$\operatorname{div} \vec{B} = 0, \quad \operatorname{rot} \vec{B} = 0 \tag{5.2}$$

subjected to boundary conditions (5.1). An elegant way to solve these equations is based on theory of complex variable functions [19]. Introducing the complex function $H(z) = H_x + \mathrm{i}H_y$ of complex variable $z = x + \mathrm{i}y$, then from Maxwell equations (5.2) it follows that H_x and H_y satisfy the Cauchy conditions for an analytic function. The problem of finding $H(z)$ is, therefore, reduced to the finding of an analytic function satisfying conditions (5.1). One can show that [19]

$$H(z) = -\frac{H_J}{\pi}\left[\left(\frac{z^2-b^2}{z^2-w^2}\right)^{1/2} \ln\left(\frac{w+b}{w-b}\right) - \ln\frac{(1-z^2/b^2)^{1/2}+(1-z^2/w^2)^{1/2}}{(1-z^2/b^2)^{1/2}-(1-z^2/w^2)^{1/2}}\right] H_\infty \left(\frac{z^2-b^2}{z^2+b^2}\right)^{1/2} . \tag{5.3}$$

Using this function we obtain the total magnetic flux

$$\Phi = 2\int_0^b H_y \,\mathrm{d}x = \Phi_J + \Phi_H \ ,$$
$$\Phi_J = -\frac{2wH_J}{\pi}\left\{[E(m) - (1-m)K(m)] \ln\frac{1+\sqrt{m}}{1-\sqrt{m}} - 2\sqrt{m}K(m)\right\} \ ,$$
$$\Phi_H = 2wH_\infty[E(m) - (1-m)K(m)], \quad m = b^2/w^2 \ , \tag{5.4}$$

where $E(m)$ and $K(m)$ are complete elliptic integrals [164]. The condition $\Phi = 2wH_\infty f$, with f being the fraction of trapped flux, gives the relation between the critical field H_J and the width b of flux region.

The magnetic moment can be determined from the large-distance asymptotics of the field as

$$H(z) \to \frac{4wdM}{z^2}, \quad z \to \infty \ , \tag{5.5}$$

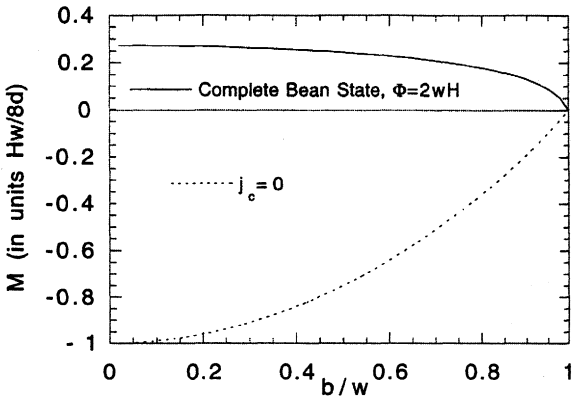

Fig. 23. Dependence of magnetic moment in the compressed flux state ($f = 1$) on the relative width of the flux region. For comparison similar dependence for an ideal superconductor ($j_c = 0$) is shown. After Koshelev and Larkin [19].

which gives

$$M = M_J + M_H \ ,$$
$$M_J = \frac{H_J w}{8\pi d}\left[(1-m)\ln\left(\frac{1+\sqrt{m}}{1-\sqrt{m}}\right) + 2\sqrt{m}\right] \ ,$$
$$M_H = -\frac{H_\infty w}{8d}(1-m) \ . \tag{5.6}$$

Parameter m has to be expressed through the critical current $J_c = cH_J/2\pi$ and the fraction of captured flux $f = \Phi/2wH_\infty$ using Eq. (5.4). In the limit $m \ll 1$ (strong compression) the magnetic moment

$$M = \frac{H_J w\sqrt{m}}{8d}\left(\frac{4}{\pi} - \frac{1}{f}\right) + \mathrm{O}(m) \tag{5.7}$$

which is positive for $f > \pi/4 \approx 0.79$. Remarkably, this value almost coincides with the critical value $f \approx 0.8$ (above which a paramagnetic moment is possible) obtained numerically [19]. Fig. 23 shows the dependence of M on the relative width of flux region b/w for $f = 1$ obtained from Eqs. (5.4) and (5.6).

In the weak compression regime $w - b \ll w$ one can show that the magnetization is always negative [19].

5.2. Ginzburg–Landau equation approach

In this section we consider the flux compression mechanism by the another approach [21] which is based on the self-consistent numerical solution of the Ginzburg–Landau equations. One can show show that due to confined geometry the giant vortex state is formed in the FC regime at the third critical field $H_{c3}(T)$. The PME appears as a result of the flux trap inside the giant vortex state with a fixed orbital quantum number L.

The basic postulate of the Ginzburg–Landau theory is that if the Cooper wave function Ψ is small and varies slowly in space, the free energy $\mathscr{F}$ can be expanded in a series of the form [165]

$$\mathscr{F} = \int \mathrm{d}\vec{r} \left\{ \alpha|\Psi|^2 + \frac{\beta}{2}|\Psi|^4 + \frac{1}{2m^*}\left|\left(\frac{\hbar}{\mathrm{i}}\nabla - \frac{e^*}{c}\vec{A}\right)\Psi\right|^2 + \frac{H^2}{8\pi}\right\} , \tag{5.8}$$

where $\alpha(T) \propto (T - T_{c0})$, T_{c0} is the mean field transition temperature. Minimizing the Ginzburg–Landau free energy with respect to the fields $\Psi(\vec{r})$ and vector potential $\vec{A}(\vec{r})$ one can get two well-known equations which will be used to study the PME.

Following Ref. [21] (see also Ref. [166]) we consider a infinitely long cylinder of radius r_0 in a magnetic field parallel to its axis. First we will find $H_{c3}(T)$ above which the nucleation of the superconducting phase takes place and then study the PME. Determination of $H_{c3}(T)$ requires to solve the linearized Ginzburg–Landau equation for the superconducting order parameter Ψ [7]

$$\frac{1}{2m}\left(-\mathrm{i}\hbar\vec{\nabla} - \frac{e^*}{c}\vec{A}\right)^2 \Psi = -\alpha\Psi , \tag{5.9}$$

which is identical to the Schrödinger equation for a particle of charge $e^* = 2e$ in a uniform magnetic field given by the vector potential $\vec{H} = \vec{\nabla} \times \vec{A}$. Parameter α in Eq. (5.9) plays the role of energy E in the corresponding Schrödinger equation and

$$E = -\alpha = \frac{\hbar^2}{2m\xi^2(T)} = \frac{\hbar^2}{2m\xi^2(0)}\frac{T_{c0} - T}{T_c} , \tag{5.10}$$

where $\xi(T)$ is the bulk coherence length and T_{c0} is the critical temperature at zero field.

For finite samples the order parameter Ψ should satisfy the boundary condition for a superconductor-insulator interface [167]

$$\left(-\mathrm{i}\hbar\vec{\nabla} - \frac{e^*\vec{A}}{c}\right)\Psi|_n = 0 \tag{5.11}$$

which assures that no current passes through the surface.

The common strategy to find $H_{c3}(T)$ is that [7] one has to solve the linearized Ginzburg–Landau equation subjected to the boundary condition (5.11). Then $H_{c3}(T)$ is subtracted from the lowest energy $E(H)$ which gives the highest T in Eq. (5.10) coinciding with the nucleation phase boundary. In the case of large bulk samples when the boundary condition (5.11) becomes irrelevant, the lowest Landau level $E = \hbar\omega/2$ (the cyclotron frequency $\omega = e^*H/mc$) gives the well known upper critical field H_{c2}

$$H_{c2} = \frac{\hbar c}{e^*\xi^2(0)}\frac{T_{c0} - T}{T_{c0}} = \frac{\Phi_0}{2\pi\xi^2(T)} . \tag{5.12}$$

For samples of confined geometry the boundary condition (5.11) must be taken into account. The crucial question is how small the sample should be to observe the finite size effect. To answer this question one may refer to analogy between the Ginburg–Landau equation (5.9) and the Schrődinger equation for normal electron considered by Dingle [168] for the analysis of quantum oscillations in small metallic samples. The finite size effect is expected to become visible [168] provided $r_0 \leqslant r_L$,

where r_L is the Larmor radius or

$$H \times r_0 \leqslant 5(Gcm) \ . \tag{5.13}$$

Clearly, the critical size depends on the applied magnetic field. If the size is equal to, say, $r_0 = 5$ μm then the boundary condition (5.11) must be taken account for $H < 10^4$ G.

In order to solve the linearized Ginzburg–Landau equation (5.9) for a long cylinder we choose the cylindrical coordinates (r, ϕ, z) and the following gauge:

$$\vec{A} = (0, Hr/2, 0) \ . \tag{5.14}$$

Then the solution reads as [169]

$$\Psi_L(R, \phi) = e^{\pm iL\phi} R^L \exp(-R^2/2) M(-N, L+1, R^2) \tag{5.15}$$

and the energy $E_\perp$ of motion in the plane perpendicular to $\vec{H}$ is given by the orbital quantum number L and parameter N:

$$E_\perp = \frac{e^* \hbar H}{2mc} (2N \pm L + L + 1) \ . \tag{5.16}$$

Here $M(-N, L+1, R^2)$ is the Kummer function [169], the dimensionless radius $R = \sqrt{\gamma} r$, $\gamma = e^* H/(2\hbar c)$. From the condition $\Phi(r, \phi + 2\pi) = \Phi(r, \phi)$ it follows that L should be integer number. It is important to stress that N is not necessarily integer number and it must be found from the boundary condition (5.11) which with the gauge choice (5.14) is reduced to

$$\frac{\partial |\Psi(R)|}{\partial R}|_{R=R_0} = 0 \ . \tag{5.17}$$

So far as we are looking for the lowest possible energy state for determination of $H_{c3}(T)$, one should take the minus sign in the argument of the exponent $\exp(-iL\phi)$ in the solution (5.15). Then the energy levels become

$$E_\perp = \hbar\omega(N + 1/2) \ , \tag{5.18}$$

where ω is the cyclotron frequency. This expression coincides with the well-known Landau levels but now N is any real number including negative one.

From Eqs. (5.15) and (5.17) we obtain the equation for determination of the parameter N [21]

$$(L^2 - R_0^2) M(-N, L+1, R_0^2) - \frac{2NR_0^2}{L+1} M(-N+1, L+2, R_0^2) = 0 \ . \tag{5.19}$$

Remarkably, the numerical solution of the last equation gives negative values for $N(L, R_0)$ which immediately lead to the energy $E_\perp$ in (5.18) lower than the bulk value $\hbar\omega/2$. Therefore, as seen from Fig. 24, in the presence of the finite surface the superconductivity can occur well above $H_{c2}(T)$ line obtained for $N = 0$. The cusplike phase boundary H_{c3} occurs due to switching between different orbital momenta L. Such a phase boundary was observed experimentally [170,171] for the superconducting disks. The linear component of the cusplike H_{c3} line is $1.965H_{c2}$, which is in good agreement with the calculations of H_{c3} in the $L \to \infty$ limit [167,172].

In order to study the PME one has to answer the following question: how to mimic the FC and ZFC experiments by the Ginzburg–Landau method? In the FC mode when the external field is

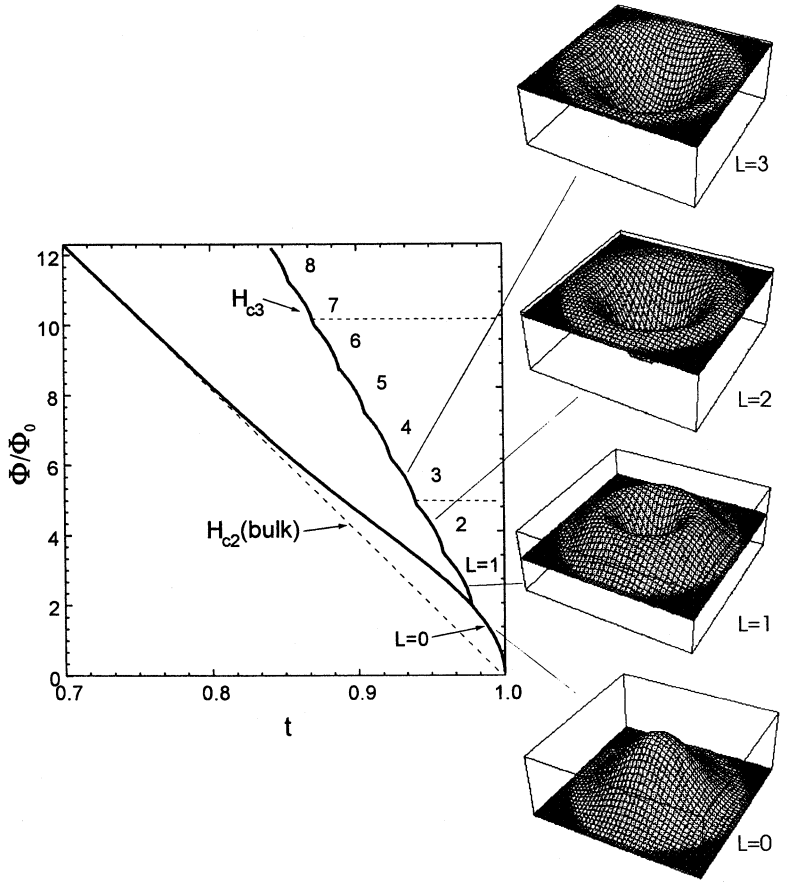

Fig. 24. The third critical field H_{c3} and the bulk upper critical field H_{c2} (dashed line) vs. normalized temperature $t = T/T_c$. The cusplike H_{c3} is formed due to the jump of the orbital quantum number L. The three-dimensional plot of $|\Psi|$ is shown for several values of L. After Moshchalkov et al. [21].

applied to a sample the states with orbital quantum numbers $L > 0$ corresponding to the rotation of the superconducting condensate due to the action of the Lorentz force are expected to be formed. Then by cooling down we are crossing the $H_{c3}(T)$ boundary (see Fig. 24) at a given $L > 0$ and reaching a temperature $T < T_{c3}(H)$ at which measurements are carried out. It should be noted that [173] L can be retained over a large temperature interval, namely, from $T(H_{c3})$ to $T(H_c)$ (near or at $T(H_c)$ the quantum number L changes abruptly, thereby expelling a large amount of flux from the sample, as the specimen makes a transition to the Meissner state). From the physical point of view, the conservation of L is related to pinning of the giant vortex state by the sample boundary. Thus, the FC experiments may be analysed by solving the Ginzburg–Landau equations below $H_{c3}(T)$ for fixed $L > 0$. The same is valid for the ZFC regime but with $L = 0$.

Below $H_{c3}(T)$, one needs to solve the full Ginzgurg–Landau equations because the superconducting condensate induces the screening due to supercurrents (proportional to Ψ^2) which should be taken

into account. Then two coupled dimensionless equations are [174]

$$\left(\frac{\vec{\nabla}}{\mathrm{i}\kappa}-\vec{A}\right)^2\Psi=\Psi(1-|\Psi|^2)\ ,$$

$$\vec{\nabla}\times\vec{\nabla}\times\vec{A}=\frac{1}{2}$$

$$\left[\Psi^*\left(\frac{\vec{\nabla}}{\mathrm{i}\kappa}-\vec{A}\right)\Psi+\Psi\left(-\frac{\vec{\nabla}}{\mathrm{i}\kappa}-\vec{A}\right)\Psi^*\right]\ , \tag{5.20}$$

where $\Psi,\vec{A}$ and r are in units of $\Phi_{\mathrm{infty}},\sqrt{2}H_{\mathrm{c}}\lambda(0)$ and $\lambda(0)$, respectively. Ψ_∞, H_{c}, $\lambda(0)$ and κ are the wave function in bulk, the thermodynamic critical field, the penetration depth at zero field and zero temperature, and the Ginzburg–Landau parameter, respectively. For the cylindrical symmetry we choose

$$\Psi(r,\phi)=\mathrm{e}^{\mathrm{i}L\phi}F(r),\quad \vec{A}=\left(0,\frac{Hr}{2}+\frac{\varphi}{2r},0\right)\ . \tag{5.21}$$

Comparing Eqs. (5.21) and (5.14) one can see that the vector potential in the full Ginzburg–Landau equations contains the induced field neglected in the linear approximation. Denoting the local magnetic field by b and using $\vec{b}=\vec{\nabla}\times\vec{A}$ we have

$$b=H+\frac{1}{2r}\frac{\mathrm{d}\varphi}{\mathrm{d}r}\ . \tag{5.22}$$

Substitution of Eqs. (5.21) and (5.22) into Eq. (5.20) gives two coupled equations for determination of F and φ [21]

$$\frac{\mathrm{d}^2F}{\mathrm{d}r^2}=-\frac{1}{r}\frac{\mathrm{d}F}{\mathrm{d}r}+\left(\frac{1}{2}\kappa Hr+\frac{1}{2}\frac{\kappa\varphi}{r}-\frac{L}{r}\right)^2F-\kappa F(1-F^2)\ ,$$

$$\frac{\mathrm{d}^2\varphi}{\mathrm{d}r^2}=\frac{1}{r}\frac{\mathrm{d}\varphi}{\mathrm{d}r}+\left(Hr^2+\varphi-\frac{2L}{\kappa}\right)F^2\ . \tag{5.23}$$

The corresponding boundary conditions are [175]

$$\frac{\mathrm{d}F}{\mathrm{d}r}=0,\quad \frac{\mathrm{d}\varphi}{\mathrm{d}r}=0 \tag{5.24}$$

at $r=r_0$ and

$$\varphi=0,\ F=0\quad \text{for } L\neq 0\ ,$$

$$\frac{\mathrm{d}F}{\mathrm{d}r}=0\quad \text{for } L=0\ , \tag{5.25}$$

at $r=0$.

The magnetization per unit volume $4\pi M$ can be defined via the flux through the cylinder and has the following form:

$$\frac{4\pi M}{H_{\mathrm{c}}}=2\int_0^{r_0}(b(r)-H)r\,\mathrm{d}r=\varphi(r_0)\ . \tag{5.26}$$

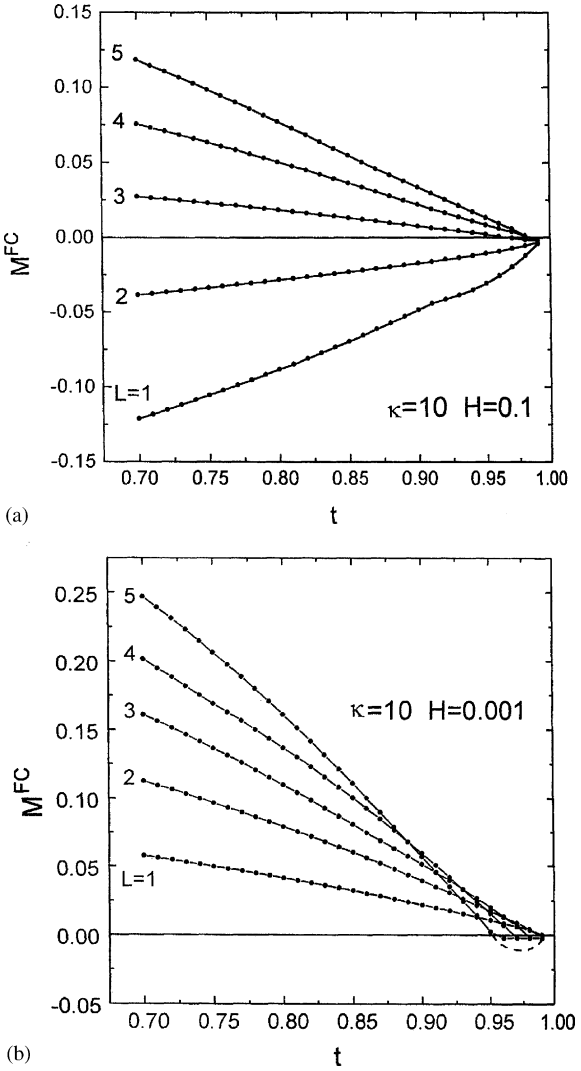

Fig. 25. Temperature dependence of M_{FC} of a superconductor with the Ginzburg–Landau parameter $\kappa = 10$ for different values of L in applied magnetic field $H = 0.1$ (a) and $H = 0.01$ (b). The radius of the cylinder $r_0 = \sqrt{3}\lambda(0)$. After Moshchalkov et al. [21].

As in the linear approximation the orbital quantum number L remains a good quantum number due to the cylindrical symmetry. For a fixed L one can solve Eqs. (5.23)–(5.25) numerically to obtain the magnetization in the FC mode. The typical results are shown in Fig. 25. In accord with experiments the PME occurs for the fixed values of L and it gets enhanced as the external field is lowered. The paramagnetic signal is, however, sensitive to H and L. For $L = 1$ and 2 the increase in the field from $H = 0.001$ to $H = 0.001$ changes the sign of the magnetization from unusual paramagnetic to conventional diamagnetic. The reported sensitivity to the surface treatment [16,17,42] may be caused

by violation of the L conservation and recovery of a normal diamagnetic response corresponding to a transition from large L values trapped at H_{c3} to the state with $L = 0$.

The numerical solution of Eqs. (5.23)–(5.25) for the ZFC regime with $L = 0$ gives, in agreement with experiments, the diamagnetic response at any temperature [21]. Thus, the PME and its field dependence can be obtained from the self-consistent solution of the Ginzburg–Landau equations assuming that orbital quantum number L is conserved. This very simple and natural approach does not involve any further assumptions related to the existence of a π junction or d- wave superconductivity. The drawback of the Ginzburg–Landau equation approach is that it does not allow for studying the PME far from the transition temperature to the superconducting phase.

The PME in a mesoscopic disk has been also studied [176,55] by the Ginzburg–Landau method. The results are qualitatively the same as for the case of the cylindrical symmetry.

To summarize this section, according to the Ginzburg–Landau theory, the paramagnetism in low-T_c mesoscopic superconductors may be caused by moments in giant vortex states. The vortices formed inside a sample in the FC regime get pinned to the boundary which is a source of inhomogeneity. The directions of the external and of the vortex magnetic fields are the same but the directions of currents screening these fields from the bulk are opposite. Since the screening currents contribute to the magnetic moment they give two contributions of opposite sign ($M = M_{\rm dia} + M_{\rm para}$). The distributions of the fields and currents inside the sample vary with H and the measured magnetization, therefore, may be either positive or negative depending on H.

6. Chiral glass

The existence of spontaneous supercurrents in ceramic superconductors may lead to, as assumed by Kusmartsev [8], a so called “orbital glass”. A natural question arises is what is the nature of the orbital glass? The picture by Sigrist and Rice [9] is essentially a single-loop picture in which the interactions between loops are irrelevant. In their scenario, when the temperature is lowered across the superconducting transition of each grain $T_c^{\rm gr}$, the FC susceptibility changes sign from negative to positive at a certain temperature T_0, sightly below $T_c^{\rm gr}$. Such a change of sign of $\chi_{\rm FC}$, which is often regarded as a measure of the orbital glass transition point, is a crossover not related to any intergranular (interloop) cooperative phenomena. In this picture, the PME arises as a property of an ensemble of noninteracting loops if there occurs an intragranular superconducting transition. By contrast, the possible cooperative character of the orbital glass was pointed out by Dominguez et al. [12] and by Khomskii [6], although these authors did not detail the nature of the cooperative phenomena.

Naturally, one may ask here whether could be a thermodynamically stable orbital glass state characterized by a spontaneous breaking of certain symmetry over an entire granular system. An issue to be addressed is whether there could be some sort of thermodynamic *intergranular* phase transition accompanied with a divergent length scale over grains, and if it is, what is the order parameter of such phase transition. It is reasonable to assume that the orbital glass is, similar to spin glass, a state of frozen spontaneous moments or fluxes due to frustration caused by random distribution of π junctions.

An attempt [177] to detect such a orbital (or flux) glass by Monte Carlo simulations with the use of multi-loop model (4.5) gave an ambiguous conclusion. Instead, the simulations [27,177] showed

clearly that a novel thermodynamic phase may occur *in zero external field* in certain ceramic high-T_c superconductors. This phase is characterized by a spontaneously broken time-reversal symmetry with keeping $U(1)$ gauge symmetry, and is called "chiral glass phase". The order parameter is then a "chirality", quenched-in half a vortex, which represents the direction of the local loop-supercurrent circulating over grains. As one can see below, since chirality and flux have the same symmetry we believe that the orbital glass should also exist in three dimensions. The fact that it was not identified in Monte Carlo simulations [177] may be related to small system sizes.

In this chapter we introduce the chirality concept in discuss the chiral glass phase in detail. Experimental search for this new phase will be presented.

6.1. Chirality concept

Frustration in vector spin systems often give rise to noncollinear and noncoplanar spin orderings which may be characterized by the so call chiral degrees of freedom. While the chirality concept has long been a familiar concept in molecular chemistry, it was introduced into the field of magnetism first by Villain [28].

The simplest way to introduce the chirality concept [28] is to consider the XY model defined by the following Hamiltonian

$$H = -\sum_{ij} J_{ij}\vec{S}_i \cdot \vec{S}_j = -\sum_{ij} J_{ij}\cos(\phi_i - \phi_j) \ , \tag{6.1}$$

where the unit spin vector $\vec{S}_i = (\cos\phi_i, \sin\phi_i)$. Model (6.1) is the simplest version of (4.5) without the external field and screening. We consider the triangular lattice and assume that the spin-spin interaction is uniform and antiferromagnetic ($J_{ij}=J<0$), then the ground state of three spins located at corners of a triangle, as shown in Fig. 26 is two-fold degenerate. Angles between neighboring spins are 120° and -120° for the left and right panel, respectively. One may define the chirality κ via a vector product of two neighboring spins averaged over three spin pairs

$$\kappa = \frac{2}{3\sqrt{3}}\sum_{\langle ij\rangle}[\vec{S}_i \times \vec{S}_j]_z = \frac{2}{3\sqrt{3}}\sum_{\langle ij\rangle}\sin(\phi_i - \phi_j) \ . \tag{6.2}$$

Clearly, $\kappa = 1$ for the right-handed (clockwise) configuration in left panel of Fig. 26 and $\kappa = -1$ for the left-handed (counterclockwise) configuration in right panel. In the case of XY spins considered

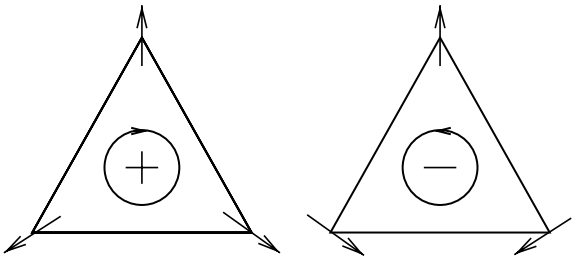

Fig. 26. The ground state spin configuration of three XY spins antiferromagnetically coupled on a triangle lattice. Frustration leads to the canted ordered state. The ground state is twofold degenerate according to whether the non-collinear spin structure is right- or left-handed, each of which is characterized by the opposite chirality as shown in left and right panel.

here, the chirality κ is actually a *pseudoscalar*. It remains invariant under global SO(2) proper spin rotations while it changes sign under global Z_2 spin reflections. In order to transform the chiral state with $\kappa = 1$ to the state with $\kappa = -1$ one needs to make a global spin reflection.

It should be noted that if the interaction is ferromagnetic then the system becomes geometrically unfrustrated (all spin in the ground state are parallel) and $\kappa = 0$. So the chirality concept makes sense only for frustrated systems. The chirality defined by Eq. (6.2) is a vector quantity, while in the literature one discusses also a scalar chirality [178] for Heisenberg spins.

The chirality concept plays an important role in physics of classical [178,179] and quantum [180] spin systems. Especially since the discovery of high-T_c cuprates the scalar chirality has been a key theoretical concept in physics of strongly correlated electrons [181–183]. In order for the spin chirality to be ordered both the time-reversal and parity symmetry must be broken. Breaking of these symmetries in two dimensions brings about many intriguing physics such as parity anomaly [184,185], anyon superconductivity [186], and quantized Hall effect in zero external magnetic field [187]. In this review we try to attract the attention of readers to a possibility to observe the so-called chiral glass phase in ceramic materials.

6.2. Simulation search for the chiral glass phase

In order to study the nature of ordering of the chiral glass phase in ceramic superconductors we use the multi-loop Hamiltonian (4.5) with the zero external field. The Josephson coupling J_{ij} is assumed to be an independent variable taking the values J or $-J$ with equal probability (bimodal distribution). While we present results for this particular distribution, one could expect from experience in spin glass studies that the results would be rather insensitive to the details of the distribution.

Contrary to the gauge-glass model [188–190], the Hamiltonian (4.5) defined at $H = 0$, keeps the Z_2 time-reversal symmetry in addition to the $U(1)$ gauge symmetry. Frustration arises from the random distribution of both positive and negative Josephson couplings. This should be contrasted to the vortex-glass (gauge-glass) problem, where the associated Hamiltonian does not possess the time-reversal symmetry due to external magnetic fields, while the frustration arises from the magnetic field but not from the J_{ij}.

Extending definition (6.2) to the case of the multi-loop model the local chirality at each plaquettes is given by the gauge-invariant quantity [145]

$$\kappa_p = 2^{-3/2} \sum_{\langle ij \rangle}^{p} \mathrm{sign}(J_{ij}) \sin\left(\phi_i - \phi_j - A_{ij}\right) , \tag{6.3}$$

where the sum runs over a directed contour along the sides of the plaquette p. Physically, the chirality, κ_p, is a half (π) vortex, being proportional to the loop-supercurrent circulating round a plaquette p. If the plaquette p is frustrated, the local chirality κ_p tends to take a finite value, its sign representing either clockwise or counterclockwise orientation of circulating supercurrent. If, on the other hand, the plaquette is unfrustrated, as mentioned before, it tends to take a value around zero. Note that the chirality is a pseudoscalar in the sense that it is invariant under global $U(1)$ gauge transformation, $\phi_i \to \phi_i + \Delta\phi$, $A_{ij} \to A_{ij}$, but changes its sign under global Z_2 time-reversal transformation, $\phi_i \to -\phi_i$, $A_{ij} \to -A_{ij}$. Due to this symmetry property, chirality can be regarded as an order parameter of the chiral order.

In analogy with the spin glass theory, the chiral glass phase may be characterized by the Edwards–Anderson order parameter [191] $q_{\mathrm{CG}}^{\mathrm{EA}}$:

$$q_{\mathrm{CG}}^{\mathrm{EA}} = [\langle \kappa_p \rangle^2]_J \ . \tag{6.4}$$

In the chiral glass phase $q_{\mathrm{CG}}^{\mathrm{EA}} \neq 0$, while in the chirality-disordered ("paramagnetic") phase $q_{\mathrm{CG}}^{\mathrm{EA}} = 0$. In the chiral glass state chiralities are orientated randomly in space but frozen in time.

The magnetization and linear susceptibility are given by Eqs. (4.10) and (4.11) but with $\Phi^{\mathrm{ext}} = 0$. The nonlinear susceptibility, χ_2 is defined as follows [145,177]:

$$\chi_2 = \frac{1}{6}\frac{\mathrm{d}^3 m}{\mathrm{d}H^3} = \frac{1}{6}\left(\frac{\pi J N_p}{k_{\mathrm{B}} T \tilde{L}}\right)^3 [\langle m^4 \rangle - 3\langle m^2 \rangle^2 - 4\langle m \rangle \langle m^3 \rangle + 12\langle m^2 \rangle \langle m \rangle^2 - 6\langle m \rangle^4]_J \ . \tag{6.5}$$

Note that χ_2, being proportional to the minus of the third-harmonic component of the ac susceptibility, is sometimes denoted as χ_3 in the literature.

Following the standard technique from the spin glass theory [144] we introduce the overlap q between the chiral variables in the two independent replicas [27,177]

$$q = \frac{1}{N_p} \sum_p \kappa_p^{(1)} \kappa_p^{(2)} \ , \tag{6.6}$$

where upper indices 1 and 2 denote two replicas. In terms of this chiral overlap the Binder ratio of the chirality is calculated by

$$g_{\mathrm{CG}} = \frac{1}{2}\left(3 - \frac{[\langle q^4 \rangle]_J}{[\langle q^2 \rangle]_J^2}\right) \ . \tag{6.7}$$

Here g_{CG} is normalized so that in the thermodynamic limit it tends to zero above the chiral glass transition temperature, T_{CG}, and tends to unity below T_{CG} provided the ground state is non-degenerate. At the chiral glass transition point, curves of g_{CG} against T for different system sizes l should intersect asymptotically. It should be noted that one can use not only the standard Binder function g but also the so-called A and G function [192–194] to study the nature of ordering in frustrated systems.

The chiral glass susceptibility, which is expected to diverge at the chiral glass transition point, is given by

$$\chi_{\mathrm{CG}} = N_p [\langle q^2 \rangle]_J \ . \tag{6.8}$$

In the framework of the one-parametric scaling theory the correlation length ξ diverges as one approaches to the chiral glass transition temperature by a power law

$$\xi \sim |T - T_{\mathrm{CG}}|^{-\nu_{\mathrm{CG}}} \ . \tag{6.9}$$

The divergence of the nonlinear and the chiral glass susceptibilities near T_{CG} is characterized by critical exponent γ_2 and γ_{CG}

$$\begin{aligned} \chi_2 &\sim |T - T_{\mathrm{CG}}|^{-\gamma_2} \ , \\ \chi_{\mathrm{CG}} &\sim |T - T_{\mathrm{CG}}|^{-\gamma_{\mathrm{CG}}} \ . \end{aligned} \tag{6.10}$$

For the finite size scaling analysis we introduce the scaling functions [144,27,177]

$$g_{\mathrm{CG}} \equiv g_{\mathrm{CG}}(l^{1/\nu_{\mathrm{CG}}}|T - T_{\mathrm{CG}}|) \tag{6.11}$$

for the Binder parameter,

$$\chi_2 = L^{\gamma_2/\nu_{\mathrm{CG}}}\tilde{\chi}_2(l^{1/\nu_{\mathrm{CG}}}|T - T_{\mathrm{CG}}|)\ , \tag{6.12}$$

for the nonlinear susceptibility and

$$\chi_{\mathrm{CG}} = L^{2-\eta_{\mathrm{CG}}}\tilde{\chi}_{\mathrm{CG}}(l^{1/\nu_{\mathrm{CG}}}|T - T_{\mathrm{CG}}|) \tag{6.13}$$

for the chiral glass susceptibility. The critical exponents can be determined from the condition that the scaling functions, plotted versus argument $l^{1/\nu_{\mathrm{CG}}}|T - T_{\mathrm{CG}}|$, should not depend on system size l [195]. In the other words, they must be collapsed onto a single curve. Exponent η_{CG} determining the decay of the chiral correlation function at $T = T_{\mathrm{CG}}$ ($[\langle\kappa_p(0)\kappa_p(r)\rangle]_J \sim r^{-D+2-\eta_{\mathrm{CG}}}$, where D is spatial dimensionality) and exponent γ_{CG} are related by a simple scaling law

$$\gamma_{\mathrm{CG}} = (2 - \eta_{\mathrm{CG}})\nu_{\mathrm{CG}}\ . \tag{6.14}$$

In the vicinity of the transition point the Edwards–Anderson order parameter behaves as

$$q_{\mathrm{CG}}^{\mathrm{EA}} \sim |T - T_{\mathrm{CG}}|^{\beta_{\mathrm{CG}}}\ . \tag{6.15}$$

Exponent β_{CG} is expressed via the other exponents by

$$2\beta_{\mathrm{CG}} = D\nu_{\mathrm{CG}} - \gamma_{\mathrm{CG}}\ . \tag{6.16}$$

It should be noted that the chiral glass phase in the multi-loop model (4.5) without screening has been studied [196,197] by Monte Carlo simulations. It was shown that thermal fluctuations destroy the three-dimensional spin glass ordering but leaving the chiral glass ordering to be stable at nonzero temperature. Although chiralities and Ising spins have the same symmetry, the chiral and spin glass phases may belong to different universality classes. Furthermore, in contrast to spin glasses, the chiral glass phase is likely to exhibit a one-step-like peculiar replica symmetry breaking [197]. Similar behavior was recently observed in the chiral glass state of the three-dimensional Heisenberg systems [198]. The one-step replica symmetry breaking was also reported to take place in the random field model [199] and fragile glasses [200].

In this review we focus on the chiral glass phase in the model (4.5) with screening which captures the PME in ceramic superconductors. Moreover, the screening effect could be substantial in intergranular ordering of these materials since the length unit to be compared with the penetration depth is the grain size ($\sim$ 1 μm) rather than the short coherence length of the Cooper pair. As the screening effect makes the otherwise long-ranged interaction between vortices short ranged and destabilizes the vortex glass (or gauge glass) phase of type-II superconductors in a field [201,202], one wonders if it would eventually wash out a sharp phase transition to the chiral glass phase.

Because of a rugged energy landscape the multi-loop model (4.5) is very hard to equilibrate. This difficulty can be partially overcomed by using, e.g., the Monte Carlo exchange method proposed by Hukushima and Nemoto [203]. The work of these authors was influenced by the simulated tempering method [204], which in turn can be understood as a special case of the method of expanded ensembles [205]. In the extended ensemble method of Ref. [203] one simulates the sample with a given bond

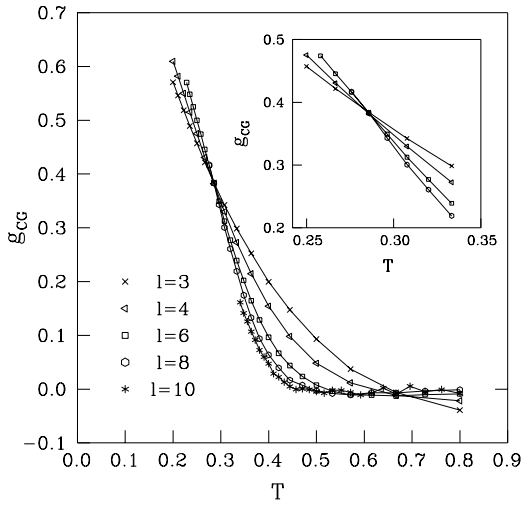

Fig. 27. The temperature and size dependence of the Binder ratio of the chirality, g_{CG}, for $\tilde{L} = 1$. Inset is a magnified view around the transition temperature $T_{CG} \simeq 0.29$. After Kawamura and Li [27].

realization at N_T distinct temperatures at a time distributed in the range $[T_{min}, T_{max}]$ and the whole configurations at two neighboring temperatures are occasionally exchanged. Monte Carlo updating consists of the two parts: The first part is the standard local Metropolis updating at each temperature, and the second part is an exchange of the whole lattices at two neighboring temperatures. Parameters N_T, T_{min} and T_{max} should be chosen in such a way that each replica could wander over the whole temperature region and the rate of exchanges between two neighboring temperatures would be of order of 0.5 and nearly constant [203].

We present mainly the results obtained for the inductance $\tilde{L} = 1$ by the replica exchange Monte Carlo [203] simulations. Fig. 27 displays the size and temperature dependence of the Binder ratio of the chirality, g_{CG}. The data of g_{CG} for $l = 3, 4, 6, 8$ all cross at almost the same temperature $T \approx 0.29$, strongly suggesting the occurrence of a finite-temperature chiral glass transition at $T_{CG} \approx 0.29$ (temperature T is measured in units of J). In particular, the data below T_{CG} show a rather clear fan out. The determined value of T_{CG} is slightly lower than the corresponding chiral glass transition temperature of the pure $\pm J$ XY spin glass determined in Ref. [196], $T_{CG} = 0.32 \pm 0.01$ (an estimate in [197] yields a higher value for T_{CG}). Note that the XY spin-glass model corresponds to the $\tilde{L} \to 0$ limit of the present model. The observed suppression of T_{CG} by the screening effect seems reasonable, since the latter makes the long-ranged interaction between chiralities short-ranged making the chiral glass transition less favorable.

Fig. 28 shows the scaling function $\tilde{g}_{CG}(l^{1/\nu_{CG}}|T - T_{CG}|)$ given by Eq. (6.11) with fixing $T_{CG} \approx 0.29$. The best scaling fit gives the correlation length exponent $\nu_{CG} = 1.3 \pm 0.2$ [27].

The temperature and size dependence of the chiral glass susceptibility, χ_{CG}, defined by Eq. (6.8), are shown in Fig. 29a. Finite-size scaling analysis based on the relation (6.13) is made with fixing $T_{CG} = 0.286$ and $\nu_{CG} = 1.3$, yielding the chiral critical-point-decay exponent $\eta_{CG} = -0.2 \pm 0.2$. The resulting finite-size-scaling plot is displayed in Fig. 29b. Other exponents can be estimated via the standard scaling relations (6.14) and (6.16) as $\gamma_{CG} \simeq 2.9$ and $\beta_{CG} \simeq 0.5$ [177].

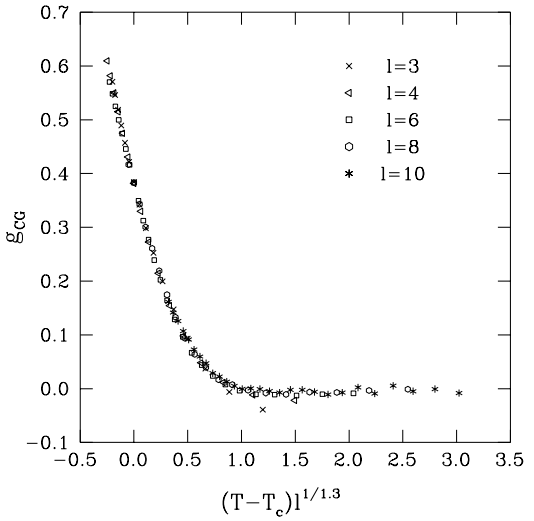

Fig. 28. Finite-size scaling plot of $\tilde{g}_{CG}$ with $T_{CG} = 0.286$ and $\nu_{CG} = 1.3$. After Kawamura and Li [27].

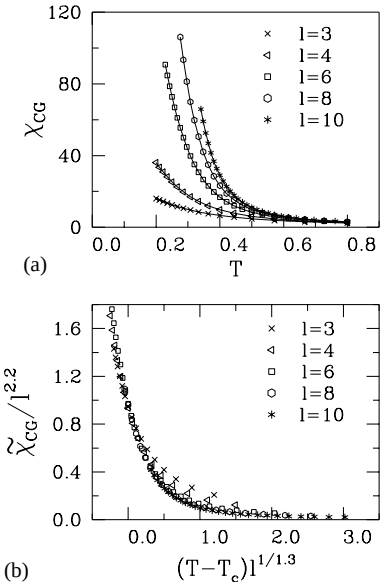

Fig. 29. (a) The temperature and size dependence of the chiral glass susceptibility, χ_{CG}, for $\tilde{L} = 1$. (b) Finite-size scaling plot of $\tilde{\chi}_{CG}$ with $T_{CG} = 0.286$, $\nu_{CG} = 1.3$ and $\eta_{CG} = -0.2$. After Ref. [177].

As one can see from Table 3, for $\tilde{L}=1$ the exponents reported in Ref. [27] are comparable to those obtained in Ref. [196] for $\tilde{L} = 0$ but they are clearly different from newer estimates of Kawamura and Li [197]. Therefore, it is not clear whether the screening effect is irrelevant or not at the 3D chiral glass transition. Further studies are required to clarify this point.

Table 3
Critical exponents of three-dimensional (3D) Ising spin glass (SG) and of 3D XY chiral glass (CG) with and without screening. The standard scaling relations have been used to obtain the full set of exponents from the values reported in the original references

Type	Distribution	Ref.	β	γ	ν	η
3D Ising SG	$\pm J$	[206]	≈ 0.55	≈ 4.0	1.7(3)	$-0.35(5)$
3D Ising SG	$\pm J$	[207]	≈ 0.65	4.1(5)	1.8(2)	$-0.26(4)$
3D Ising SG	Gaussian	[208]	≈ 0.64	≈ 4.7	2.0(1.5)	$-0.36(6)$
3D XY CG, $\tilde{L}=0$	$\pm J$	[196]	≈ 0.45	≈ 3.6	1.5(0.3)	$-0.4(2)$
3D XY CG, $\tilde{L}=0$	$\pm J$	[197]	≈ 0.69	≈ 2.2	1.2(0.2)	0.15(20)
3D XY CG, $\tilde{L}=1$	$\pm J$	[27]	≈ 0.5	≈ 2.9	1.3(0.2)	$-0.2(2)$

Within error bars the exponents of chiral glasses obtained in Refs. [196,27] coincide with those for 3D Ising spin glasses, suggesting that they belong to the same universality class. The results of [197] showed that the chiral glass transition may lie in a universality class different from the Ising glass. Regardless to this controversy, the simulations [27] gave a strong evidence of the existence of a chiral glass as a new phase in ceramic superconductors.

From the experimental point of view the nonlinear susceptibility χ_2 plays a more important role than the chiral glass susceptibility $\chi_{\rm CG}$ (6.10) because experiments can probe it directly but not $\chi_{\rm CG}$. On general theoretical grounds, χ_2 is expected to show a negative divergence at the transition point where the time-reversal symmetry is spontaneously broken in a spatially random manner [26]. The results shown in Fig. 30a are fully consistent with this expectation. The exponent associated with the negative divergence is estimated via a finite-size scaling analysis (see Fig. 30b) is equal to $\gamma_2 \simeq 4.4$ assuming $T_{\rm CG}=0.286$ and $\nu_{\rm CG}=1.3$. This value of γ_2 is larger than the chiral glass susceptibility exponent, $\gamma_{\rm CG} \simeq 2.9$. At present, it is not entirely clear whether this deviation reflects a true difference in the asymptotic critical behavior.

The tendency that the chiral glass ordering is suppressed at larger inductances was seen from simulations [177]. The phase diagram in the T–$\tilde{L}$ plane is sketched in Fig. 31. There appears to be a finite critical value of the inductance, $\tilde{L}_{\rm c}$, above which there is no equilibrium chiral glass transition. Although it is difficult to precisely locate $\tilde{L}_{\rm c}$ due to the extremely slow relaxations at low temperatures, it appears to lie around $5 \leqslant \tilde{L}_{\rm c} \leqslant 7$. It was also shown [177] that the paramagnetic tendency is more enhanced for larger $\tilde{L}$, while the chiral glass ordering itself is suppressed for larger $\tilde{L}$.

An attempt to observe the flux glass (or orbital glass) was made in Ref. [177] by the Monte Carlo simulations. Naively, one expects that the flux defined by Eq. (4.5), should behave in the same way as the chirality, since it is also a pseudoscalar variable sharing the same symmetry as the chirality. Indeed, the flux-glass susceptibility, e.g., shows a divergent behavior [177] similar to its chiral glass counterpart $\chi_{\rm CG}$. However, in contrast to the naive expectation, clear crossing of the Binder ratio as observed in $g_{\rm CG}$ is not observed in the flux glass case at least in the range of lattice sizes $l \leqslant 10$. Rather, the ordering tendency seems more enhanced in the sense that the flux glass susceptibility $g_{\rm FG}$ tends to increase with increasing L exhibiting a feature of the ordered phase even above $T_{\rm CG} \approx 0.29$ [177]. As the flux is an *induced* quantity generated by the finite inductance effect,

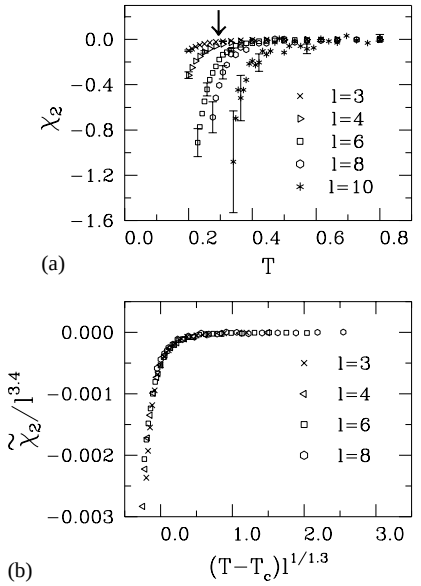

Fig. 30. (a) The temperature and size dependence of the nonlinear susceptibility χ_2 for $\tilde{L} = 1$. An arrow represents the location of the chiral glass transition point. (b) Finite-size scaling plot of $\tilde{\chi}_2$ with $T_{CG} = 0.286$, $\nu_{CG} = 1.3$ and $\gamma_2 = 4.4$. After Kawamura and Li [177].

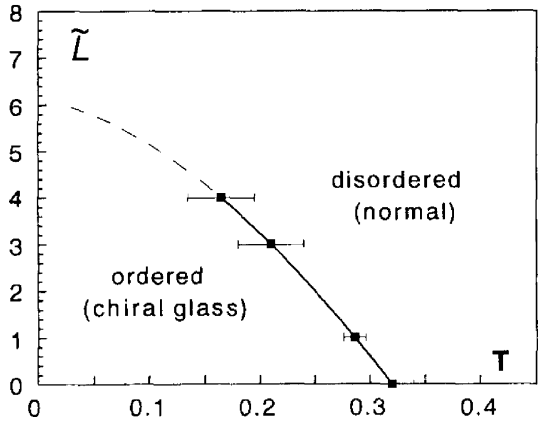

Fig. 31. A phase diagram in the T–$\tilde{L}$ plane. Renormalized inductance $\tilde{L}$ is defined by Eq. (4.3). After Kawamura and Li [27].

we believe this behavior to be a finite-size effect. Presumably, for inductance $\tilde{L} = 1$ the flux hardly reaches its asymptotic critical behavior in rather small lattices studied there. We tend to believe that the flux or orbital glass can occur in the multi-loop model (4.5) of larger system sizes and it should accompany with the PME.

6.3. Differences between chiral glass and other glassy phases in disordered type II superconductors

The point quenched randomness destabilizes the Abrikosov flux line lattice in a pure type-II superconductors, yielding novel glassy phases such as Bragg, gauge and vortex glass (the so-called Bose glass [209] caused by columnar or planar defects will not be discussed here). The aim of the present chapter is to make a clear distinction between these phases and the chiral glass. We consider the weak and strong disorder cases separately.

Bragg and vortex glass. The starting point to describe the Bragg [210–212] and vortex glass [213] is the Ginzburg–Landau free energy (5.8) with *a weak disorder*. The later can be introduced via the mean field transition temperature T_{c0} in the expression of $\alpha(T)$ in Eq. (5.8), i.e, $T_{c0} \to T_{c0} + \delta T_{c0}(\vec{r})$, where $\delta T_{c0}(\vec{r})$ is a random quantity. In the absence of an external magnetic field and disorder the model (5.9) may be mapped to the uniform XY model with the specific heat exponent $\alpha < 0$ [214,215]. Then, according to the Harris criterion [216], the weak randomness does not change the zero-field critical behavior of the type-II superconductors.

The situation becomes quite different if the external field is applied to a sample. In this case the question about the H–T phase diagram is still under debate but its currently popular view [212,217–219] is shown in Fig. 32. As shown first by Larkin [220], disorder spoils the translational long-range order in the Abrikosov lattice since the randomness in the local values of the critical temperature leads to a random potential acting on the vortices. Although the disordered averaged order parameter $[\langle \exp(\mathrm{i}\vec{Q}\cdot\vec{u})\rangle]$ ($\vec{Q}$ and $\vec{u}$ denotes a reciprocal lattice vector of the Abrikosov lattice and the vortex displacement, respectively) vanishes in the thermodynamic limit, the correlation function

$$S(\vec{Q},\vec{r}) = [\langle \exp\{\mathrm{i}\vec{Q}\cdot[\vec{u}(\vec{r}) - u(0)]\}\rangle] \tag{6.17}$$

may still obey an algebraic decay [210,217] provided the external field is weak enough. Since this algebraic decay should show up in Bragg peaks the corresponding phase is called Bragg glass [211]

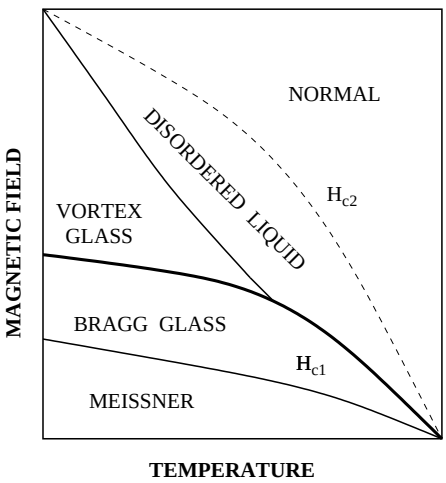

Fig. 32. A phase diagram of a weakly disordered type-II superconductor. In three dimensions the vortex glass phase should disappear in the presence of the screening.

or elastic vortex glass [221]. So the Bragg glass is characterized by translational correlations (6.17) decay asymptotically as power laws. It reflects some residual order of the Abrikosov lattice. After the Bragg glass was first proposed [211] (one should be noted that the algebraic decay of $S(\vec{Q},\vec{r})$ of three-dimensional vortex lattices in impure superconductors was first predicted by Nattermann [222]) its existence was supported by further analytical [223–225] and numerical calculations [226,227]. The strong experimental evidence for the existence of the Bragg glass phase was provided by the neutron diffraction data of Klein et al. [228].

On increasing external field the Bragg glass becomes unstable to the vortex glass phase in which translational correlations (6.17) decay exponentially. In the vortex glass phase, although there is no off-diagonal long-range order one may expect a nonzero Edwards–Anderson order parameter [213]

$$q_{\mathrm{VG}}^{\mathrm{EA}} = \frac{1}{V}\int \mathrm{d}\vec{r}\,|\tilde{\Psi}(\vec{r})|^2 \ , \tag{6.18}$$

where gauge-invariant $\tilde{\Psi}(\vec{r}) = \Psi(\vec{r})\exp[\int^x \mathrm{i}\vec{A}\,\mathrm{d}\vec{l}]$ and V is the volume of the system. This means that the vortices in this state are completely frozen at random positions dictated by the disorder as spins or chiralities in the spin or chiral glass phase. The pinning of vortex lines prevents the system from the energy dissipation and the linear resistivity should, therefore, vanish in the vortex glass phase. Interesting transport properties at and below the critical temperature were intensively discussed by Fisher et al. [221] by scaling arguments. Their predictions were confirmed by measurements of the I–V characteristics [229,230]. The existence of the vortex glass phase was also supported by simulations [227]. The evidence of the Bragg glass–vortex glass transition was provided by experiments [231,232] and simulations [227]. This transition appears to be very sensitive to the disorder strength [232].

Recently, it has been proposed that low-T_c materials would be better captured by a phase diagram different from what proposed in Fig. 32 [233]. Namely, instead of the vortex glass phase the so-called multi-domain glass would intervene between Bragg glass and disordered liquid phase. Translational correlations in this new phase are argued to exhibit a significant degree of short-range order.

Nonomura and Hu have found the vortex slush phase [234] to exist between the vortex glass and disordered liquid phases by simulations [235]. Such a new phase was not detected by similar simulations of Olsson and Teitel [236] but it seems to be supported by the resistivity experiments [237,238] and by the analytical argument [239]. Further studies are required to confirm or reject the existence of the multi-domain glass and vortex slush phases.

Gauge glass. So far the disorder was assumed to be weak. In the case of *strong disorder* gauge glass like models were proposed to describe granular superconductors [240,241]. Assuming that each superconducting grain i is described by the phase ϕ_{i} of the order parameter and the Josephson couplings J_{ij} are positive and the same for all of grain pairs ($J_{ij} = J > 0$), the Hamiltonian is given by [202]

$$\mathscr{H} = -J\sum_{\langle ij\rangle}\cos(\phi_{\mathrm{i}} - \phi_j - A_{ij} - \lambda_0^{-1}a_{ij}) + \frac{1}{2}\sum_P(\vec{\nabla}\times\vec{a})^2 \ . \tag{6.19}$$

Here $\sum_{\langle ij\rangle}$ and $\sum_P$ denotes the summation over nearest neighbours and over plaquettes of a cubic lattice, respectively. The influence of the external field and randomness is accounted by gauges A_{ij} which are taken to be independent random variables with a distribution between 0 and 2π.

$a_{ij} = \int_{\vec{r}_i}^{\vec{r}_j} \vec{a}(\vec{r})\,\mathrm{d}\vec{r}$, where $\vec{a}$ denotes the fluctuations of the vector potential which are limited by the bare screening length λ_0.

The gauge glass phase is characterized by a vanishing averaged condensate wave function $[\langle\Psi\rangle]=0$, but a finite Edwards–Anderson order parameter $[|\langle\Psi\rangle|^2]$. The transition to this phase is accompanied with a diverging gauge-glass susceptibility defined in Ref. [188].

In the absence of the screening ($\lambda_0 \to \infty$) the gauge glass was shown to be ordered at finite temperatures in three dimensions, while in two dimensions the ordering takes place only at $T = 0$ [189,190,242–247]. The analysis based on the determination of the scaling behavior of the domain wall energy $\mathscr{E}_{DW}(l) \propto l^{\theta}$ gave exponent $\theta(3D) \approx 0$ [243,242,246], indicating that the 3D gauge glass is more marginal than the Ising spin glass which have $\theta(3D) \approx 0.2$. A detailed discussion of the relation between the vortex glass and the gauge glasses was given by Blatter et al. [248]. The vortex glass occurs in the model with weak disorder but the disorder becomes effectively strong as the field is increased [249]. If one assumes (6.18) as a definition of the vortex glass order parameter then the gauge glass would be a vortex glass.

In ceramic superconductors the length unit associated with the intergranular ordering is the mean grain size which is of order micron, screening effect is generally non-negligible. The influence of screening (finite λ_0) on the nature of ordering of the gauge glass was considered by several groups [201,202,250]. It turns out that screening destroys the gauge glass transition in three dimensions. This conclusion remains unchanged if one includes the effect of anisotropy into the gauge glass model [251,252] by assuming an extra contribution to A_{ij} arising from the external field.

Contrary to the Bragg and vortex glass, the gauge and chiral glass may occur in systems with strong disorder. Comparing Hamiltonian (4.5) for the chiral glass ($\Phi_{\mathrm{p}}^{\mathrm{ext}} = 0$) and (6.19) for the gauge glass one can see two main differences. First, the former is supposed to appear in the zero external magnetic field, while the latter cannot exist without the field which serves as a source of frustration. Second, opposed to the gauge glass case where the couplings are always "ferromagnetic", the couplings in the chiral glass model may be positive or negative. This means that the chiral glass may be observed only in a system with anisotropic pairing. Since the $U(1)$ gauge symmetry is not broken, in this phase, unlike in the vortex or gauge glass, the phase of the condensate is *not* ordered, even randomly, on sufficient long length and time scales: The thermodynamic ordering occurs only in the loop-supercurrents, or in the chiralities. Therefore, the chiral glass is not thermodynamically superconducting state. The modest screening destroys the gauge glass in three dimensions but leaving the chiral glass stable against thermal fluctuations.

6.4. Experimental search for the chiral glass phase

First we will discuss some requirements for the appropriate ceramic samples where one could expect the chiral glass phase. One important parameter characterizing the sample is the dimensionless inductance, $\tilde{L}$, given by Eq. (4.3). From Fig. 31 it follows that an equilibrium chiral glass state could be realized in the samples with not large $\tilde{L}$. If one models a loop as a cylinder of radius r and height h, its inductance is given by $L = 4\pi^2 r^2/h$. Putting $r \sim 1$ μm, $h/r \sim 0.01$ and $J \sim 20$ K (these values are chosen to mimic the sample used in Ref. [29]), one gets $\tilde{L} \sim 10^{-2}$. Since this value is considerably smaller than $\tilde{L}_{\mathrm{c}}$, an equilibrium chiral glass phase may well occur in such samples. By contrast, if the sample has too large a grain size or too strong Josephson coupling, an equilibrium chiral glass phase will not be realized, or at least largely suppressed. Another requirement for the

sample is that the grains must be connected via weak links into an infinite cluster, not decomposed into finite clusters. This means that the concentration of π junctions should exceed the percolation threshold. The finite-cluster samples cannot exhibit a chiral glass transition, although the paramagnetic Meissner effect is still possible [9,253,254].

Once appropriate samples could be prepared, the chiral glass transition is detectable in principle via the standard magnetic measurements by looking for a negative divergence of nonlinear susceptibility χ_2 [27] as in the case of spin glasses. In such magnetic measurements, care has to be taken to keep the intensity of applied ac and dc fields weak enough, typically much less than 1G, so that the external flux per loop is sufficiently smaller than Φ_0.

A sharp negatively divergent anomaly of χ_2 was reported in a $YB_2C_4O_8$ ceramic sample by the ac method by Matsuura et al. [29] which might be a signal of the chiral glass transition. This study was extended by Deguchi et al. [255] to the case when the pressure is applied to a sample to vary the Josephson couplings. The transition temperature T_{CG} was found to be shifted towards higher temperatures as the pressure increases but the character of the transition to the chiral glass state remains unchanged. This observation is consistent with the theoretical prediction [27,177] that T_{CG} is determined entirely by the strength of the Josephson interaction which should grow with the pressure.

The opposite conclusion from the susceptibility data was reported by Ishida et al. [32] who showed that the nonlinear susceptibility of a $(Sr_{0.7}Ca_{0.3})_{0.95}CuO_{2-x}$ sample negatively diverges but it oscillates as a function of temperature near the critical point. As argued by these authors, such a behavior can be explained by the Bean critical state model but not by the chiral glass one.

Recently, Papadopoulou et al. [39] has also observed the negative divergence of χ_2 with exponent $\gamma_2 \approx 3.4$ for a melt-cast $Bi_2Sr_2CaCu_2O_8$ sample. This value of γ_2 is smaller that the theoretical value $\gamma_2 \approx 4.4$ but close to the chiral glass susceptibility exponent $\gamma_{CG} \approx 2.9$ [27,177]. The temperature region to observe the divergence of χ_2 is, however, too narrow that the result of Papadopoulou et al. [39] cannot be considered as a good evidence for the existence of the chiral glass phase.

As in the case of spin glasses, measurements of dynamic susceptibilities such as $\chi'(\omega)$ and $\chi''(\omega)$ would also give useful information on the possible chiral glass ordering, particularly when combined with the dynamic scaling analysis. Near the chiral glass transition point, the imaginary part of the linear susceptibility, $\chi''(\omega)$, is expected to satisfy the dynamic scaling relation of the form,

$$\chi''(\omega, T, H) \approx \omega^{\beta_{CG}/z_{CG}\nu_{CG}} \tilde{\chi}'' \left(\frac{\omega}{t^{z_{CG}\nu_{CG}}}, \frac{H^2}{t^{\beta_{CG}+\gamma_{CG}}} \right) , \tag{6.20}$$

where $t \equiv |(T - T_{CG})/T_{CG}|$ and z_{CG} is a dynamical chiral glass exponent. From Ref. [27] (see also Table 3), we get the static chiral glass exponents to be $\nu_{CG} \simeq 1.3$, $\beta_{CG} \simeq 0.5$ and $\beta_{CG} + \gamma_{CG} \simeq 3.4$. Using the dynamical exponent $z_{CG} = 6.3 \pm 1.7$ [256] we obtain a value around $z_{CG}\nu_{CG} \approx 8.2$.

A dynamic scaling analysis was made by Leylekian, Ocio and Hammann for LSCO ceramic samples [257,258]. These authors performed both the ac susceptibility and the noise measurements, and found an intergranular cooperative transition even in zero field at a temperature about 10% below the superconducting transition temperature of the grain. Note that the noise measurements enable one to probe truly zero-field phenomena where one can be free from the extrinsic pinning effects such as the ones envisaged in the so-called critical-state model [259]. It was then found that the data of χ'' satisfied the dynamic scaling relation (6.20). Here note that one is *not* allowed to invoke the standard vortex-glass scenario to explain such intergranular cooperative transition *in zero*

field, since in the standard vortex-glass picture frustration is possible only under finite external fields. By contrast, the experiment seems consistent with the chiral glass picture.

Meanwhile, when the intragranular superconducting transition and the intergranular transition take place at mutually close temperatures as in Ref. [257,258], the Josephson coupling, J, which has been assumed to be temperature independent in the present model, is actually strongly temperature dependent in the transition region. In such a case, care has to be taken in analyzing the experimental data, since the temperature dependence of J might modify the apparent exponent value from the true asymptotic value to some *effective value*. In fact, the dynamical exponent $zv \simeq 30$ determined by Leylekian et al. were different from the standard spin-glass value, which might be due to the proximity effect of the intragranular superconducting transition [257,258]. If, on the other hand, the temperature dependence of J was taken into account in the fit, a more realistic value $zv \simeq 10 - 15$ was obtained in Ref. [257,258]. As claimed by Leylekian et al. they data are compatible with the transition to the gauge glass state. Using $\nu_{GG} = 1.3 \pm 0.04$ and $z_{GG} = 4.7 \pm 0.7$ from Ref. [243], we have $z_{GG}\nu_{GG} \approx 6.2$. The experimental value seems to be more consistent with the theoretical estimate $z_{CG}\nu_{CG} \approx 8.2$ for the chiral glass than with the gauge glass (or vortex glass) counterpart. In view of large error bars, such a conclusion remains, however, ambiguous.

The most convincing evidence for the chiral glass phase from the dynamical scaling analysis of susceptibility was reported by Deguchi et al. for YBCO ceramic [260]. Their results shown in Fig. 33 give $z_{GG}\nu_{GG} = 8.2$ and $\beta_{CG} = 0.5$ which are well accounted by the chiral glass model.

Experimental data from the out-of-phase component $\chi''(\omega)$ of the ac susceptibility and the scaling analysis may be employed to obtain the relaxation time which diverges on approaching T_{CG}. In this case, a "freezing" temperature T_f, can be defined as a frequency-dependent temperature $T_f(\omega)$ at which the maximum relaxation time is $1/\omega$. If there is a phase transition at T_{CG}, the relaxation time $\tau = 1/\omega$ behaves as

$$\frac{\tau}{\tau_0} = \left| \frac{T_f(\omega) - T_{CG}}{T_{CG}} \right|^{-z_{CG}\nu_{CG}} = t^{-z_{CG}\nu_{CG}} \tag{6.21}$$

as $T \to T_{CG}$. Here $T_f(\omega)$ is chosen as the temperature at which the peak of $\chi''(\omega)$ is located. With the help of the scaling relation (6.21) Papadopoulou et al. have obtained $z_{CG}\nu_{CG} \approx 11$ for the melt-cast Bi2212 sample supporting the transition to the chiral-glass phase [31]. Moreover, a similar analysis on the sintered Bi2212 sample, that does not display magnetic aging, gave unphysical results for τ_0 and $z_{CG}\nu_{CG}$ [31]. This result strengthens the evidence for the existence of the chiral-glass phase.

Another way to probe the existence of the chiral glass phase is based on transport properties [256,30]. As mentioned above, in this phase a sample should not be true superconductor, with a small but nonvanishing linear resistivity ρ_L even at and below T_{CG}. Rough estimates of the residual ρ_L were given in [177]. The dynamical scaling theory for transport properties near the chiral glass transition may be developed with the help of its vortex glass counterpart [221]. Assume that under the external current of density j, there occurs a voltage drop, or electric field of intensity E. The voltage drop comes from two nearly independent sources: One from the motion of integer vortex lines, E_v, and the other from the motion of chiral domain walls, E_κ [256]. Then we have

$$E(j,T) = E_v(j,T) + E_\kappa(j,T)\ . \tag{6.22}$$

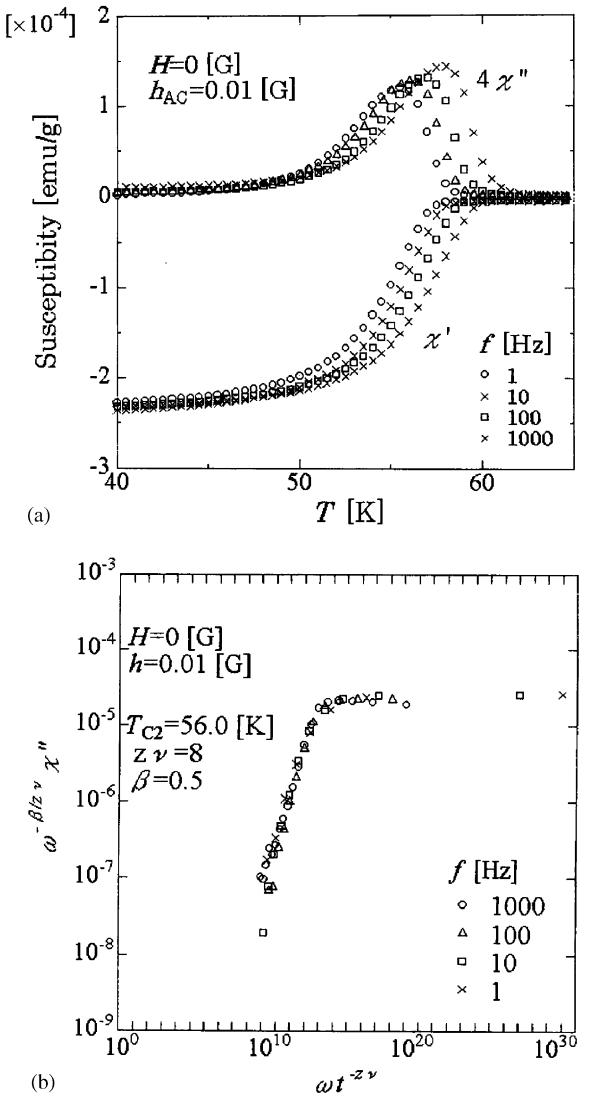

Fig. 33. (a) Temperature dependence of the linear susceptibility for different values of frequency indicated next to the curves. (b) The scaling plot for χ'' which gives $z\nu = 8$ and $\beta = 0.5$. After Deguchi et al. [260].

The first part is essentially a regular part, while the chiral part should obey the dynamic scaling law associated with the chiral glass transition, i.e.,

$$E_\kappa \approx |t|^{(z_{CG}+1)\nu_{CG}} \bar{E}_\kappa(j/|t|^{2\nu_{CG}}) \ , \tag{6.23}$$

where the spatial dimension has been set equal to $D=3$. Employing the Fisher–Fisher–Huse argument [221] yields the following asymptotic behaviors of the scaling function:

$$\bar{E}_\kappa(x) \approx \begin{cases} ax, & t > 0 \\ a' \exp[-bx^{-\mu_{CG}}] & t < 0 \end{cases} \quad \text{as } x \to 0 \ , \tag{6.24}$$

where a, a' and b are positive constants. μ_{CG} is an unknown exponent describing the chirality dynamics in the chiral glass state but it is expected to be positive (in the vortex glass case $0 < \mu \leqslant 1$).

The linear resistivity ρ_L and nonlinear resistivity ρ_{NL} can be written as a sum of the two nearly independent contributions [251],

$$\rho_L \equiv \left.\frac{dE}{dj}\right|_{j=0} = \rho_{L,v} + \rho_{L,\kappa} \ ,$$

$$\rho_{NL} \equiv \left.\frac{1}{6}\,\frac{d^3E}{dj^3}\right|_{j=0} = \rho_{NL,v} + \rho_{NL,\kappa} \ . \tag{6.25}$$

At the chiral glass transition point, the vortex terms $\rho_{L,v}(T)$ and $\rho_{NL,v}(T)$ stay finite without prominent anomaly, while the chiral parts exhibit a singular behavior associated with the transition. Then from Eq. (6.23) we have

$$\rho_{L,\kappa}(T) \approx \begin{cases} 0, & t < 0, \\ c' t^{(z_{CG}-1)\nu_{CG}}, & t > 0, \end{cases}$$

$$\rho_{NL,\kappa}(T) \approx \begin{cases} 0, & t < 0, \\ c'' t^{(z_{CG}-5)\nu_{CG}}, & t > 0. \end{cases} \tag{6.26}$$

Since $(z_{CG} - 1)\nu_{CG} \approx 6.9$ is a large positive number $\rho_{L,\kappa}(T)$ given by Eq. (6.26) vanishes toward T_{CG} sharply and the behavior of ρ_L is dominated by the regular vortex term.

As shown in the next section, Yamao et al. have observed that the nonlinear resistivity and the nonlinear magnetic susceptibility of $YB_2Cu_4O_8$ diverge at the temperature where the magnetic remanence sets in [30]. Meanwhile, the linear resistivity remains finite (see Fig. 44 below) without any appreciable anomaly. This behavior is hard to understand if one regards the transition to be a transition to the Meissner or the vortex glass phase, where ρ_L should vanish. The experimental data obtained for the linear resistivity [30] seem to be compatible with the chiral-glass picture where the total linear resistivity remains finite at $T = T_{CG}$.

As follows from Eq. (6.26), the nonlinear resistivity ρ_{NL} shows, however, stronger anomaly than ρ_L and it becomes divergent provided $z_{CG} < 5$. Using the phase representation Kawamura [256] obtained $z_{CG} = 6.3 \pm 1.7$ for the self-inductance $\tilde{L} = 1$ and it is hard to justify that $z_{CG} < 5$. Thus, it is not clear if the nonlinear susceptibility diverges at the chiral glass transition or not. So far as z_{CG} generally depends on the kind of dynamics, it may take a smaller value in the vortex representation than in the phase representation. Another possibility is that z_{CG} may depend on the self-inductance and other values of $\tilde{L}$ could lead to smaller values of z_{CG}. More accurate estimates of the dynamical exponent are needed to make a full comparison with experiments.

The chiral-glass phase is expected to display off-equilibrium phenomena similar to those in spin glasses, such as aging and memory effects. As mentioned above, recently Papadopoulou et al. [24] have observed the aging effect in ceramic BSCCO sample at very weak fields (see Fig. 40). It may have some relation to the chiral-glass order.

Taken together, the problem of the existence of the chiral glass phase in ceramic materials remains open. Further theoretical and experimental studies of off-equilibrium dynamical and transport properties of the chiral-glass ordered state would be of much interest.

7. Dynamical phenomena: experiments and simulations

In this section we present results of experimental studies of the dynamical phenomena related to the PME. Monte Carlo and Langevin dynamics simulations show that all of these phenomena may be captured by simple multi-loop model (4.5).

7.1. AC susceptibility

Experiments. It is well known that dc susceptibility provides important information on static magnetic properties of a investigated material whereas ac-susceptibility may shed light on both static and dynamic behaviors and provide the clue to the underlying mechanism for the PME.

Fig. 34 shows the ac susceptibility at different frequencies of a sintered Bi-2212 PME-sample [261] measured in an ac field $H_{ac} = 0.12$ Oe at different frequencies. The in-phase component $\chi'(\omega)$ shows shielding properties that directly correspond to the ZFC dc susceptibility. The out-of-phase component $\chi''(\omega)$ measures the dissipation in the sample and its sharp appearance takes place at a temperature very close but somewhat below T_c. The onset temperature for dissipation in the sample is almost frequency-dependent within the resolution of the measurement [261], only at an appreciably lower temperature an observable frequency dependence occurs. The broad frequency-dependent maximum

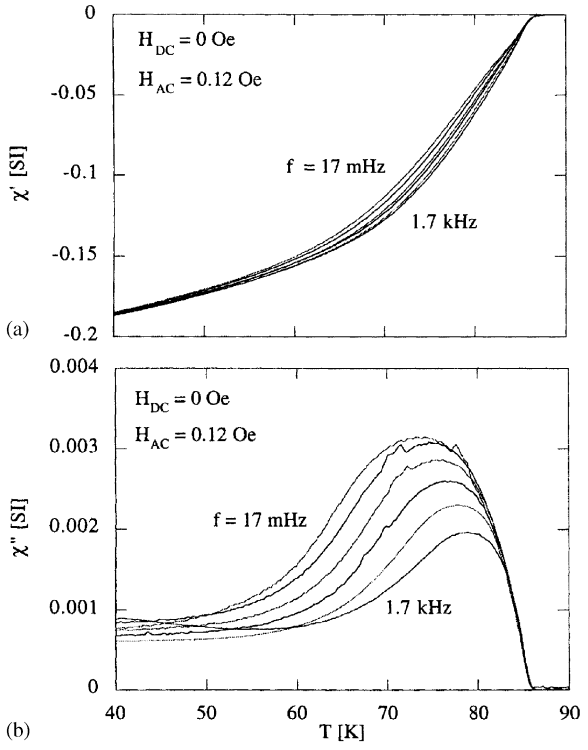

Fig. 34. Ac-susceptibility of a sintered Bi-2212 PME sample ($T_c = 87$ K) at different frequencies: 17, 170, 1.7, 170 Hz and 1.7 kHz. From Magnusson et al. [261].

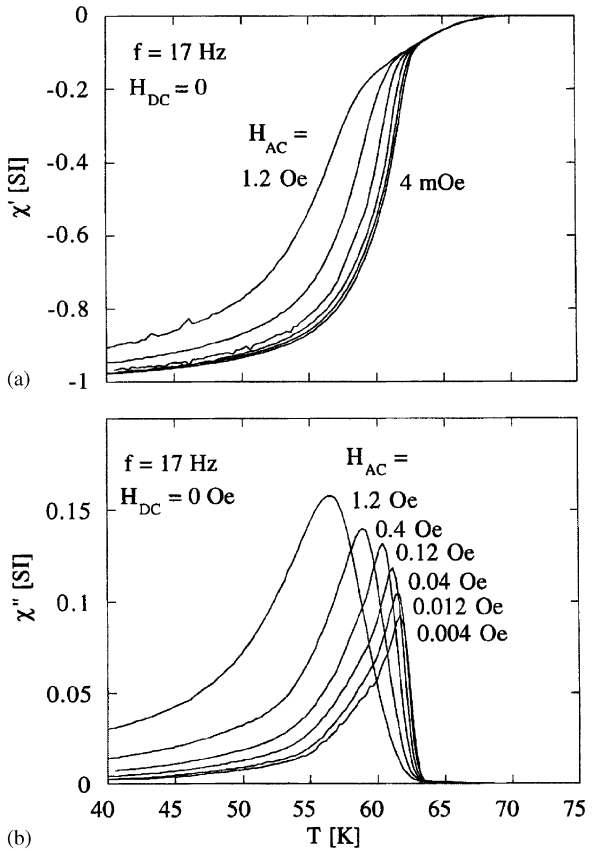

Fig. 35. Ac-susceptibility of a sintered Bi-2212 PME sample a frequency 17 Hz in different superposed dc-fields. From Magnusson et al. [261].

in $\chi''(\omega)$ from Fig. 34 and the corresponding frequency dependence of $\chi'(\omega)$ presumably come from spontaneous magnetic moments with widely distributed relaxation times.

In Fig. 35 χ' and χ'' of the above sintered Bi-2212 sample is shown at a frequency 17 Hz but in different superposed dc fields. One remarkable observation here is that at temperature close to $T_c \approx 87$ K the χ'' curves are strongly suppressed even by a dc-field as small as 0.1 Oe. This behavior contradicts the picture of conventional flux penetration where an increasing of H_{dc} should increase the dissipation and shifts χ'' to lower temperatures. The present suppression of the out-phase component may be understood assuming that the low field dynamics are governed by the response from the orbital magnetic moments. On one hand, the spontaneous moments with a relaxation time ω, where ω is the angular frequency of the ac field, are flipped back and forth by the ac-field causing the energy loss. On the other hand, the dc-field polarizes many of these moments along its direction preventing them from flipping, and thus reducing χ''.

The increase of χ'' at high dc field again is due to ordinary intragranular flux penetration [261]. An interesting difference between sintered and melt-cast samples was observed [39,261,262]: the dynamics of the former is dominated by spontaneous moments whereas the motion of thermally

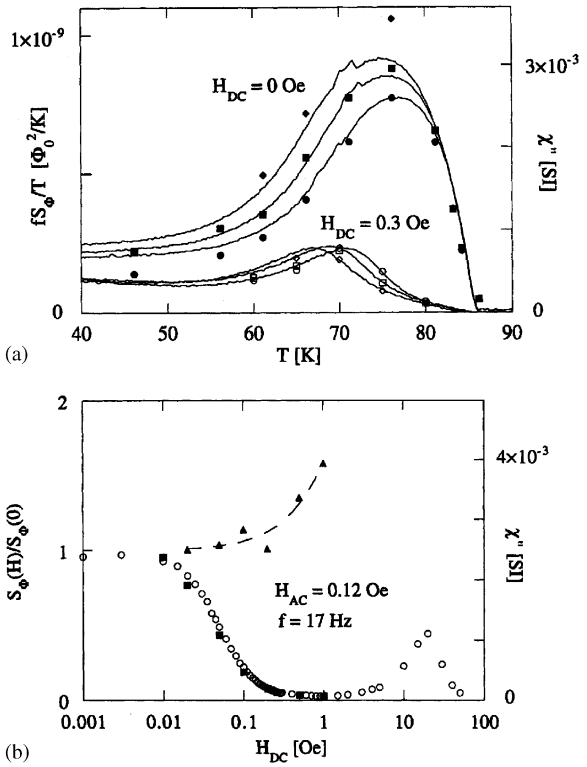

Fig. 36. (a) Magnetic flux noise fS_Φ/T (left-hand scale) at 0.2 Hz (diamonds), 2 Hz (squares), and 20 Hz (circles) and χ'' at three different frequencies, from left to right 0.17, 1.7 and 17 Hz (right-hand scale, solid lines) versus T. Filled symbols correspond to $H_{dc} = 0$ and open symbols to $H_{dc} = 0.3$. PME sample. (b) Magnetic noise $S_\Phi(H)/S_\Phi(0)$ (left-hand scale, solid squares) and χ'' (right-hand scale) at 17 Hz and $T = 80$ K vs. H_{dc} for the PME sample. The maximum at higher fields arises from intragranular flux penetration. $S_\Phi(H)/S_\Phi(0)$ at $f = 17$ Hz and $T = 62$ K versus the superimposed dc field for the non-PME sample (solid triangles) is also shown. The perfect agreement with the fluctuation dissipation theorem is seen. From Magnusson et al. [263].

excited vortices plays also an important role for the later ones. Thus, the ac susceptibility measurement points to the existence of spontaneous moments responsible for the PME but it does not clarify their origin.

Another way to probe the flux dynamics is to study the flux noise spectra $S_\phi(f)$ [263]. The suppression of the flux noise in PME samples by the dc field [263,39] (see upper panel of Fig. 36) also confirms the existence of the spontaneous supercurrents. For large enough dc fields the noise is expected to be dominated by vortices starting to grow with increasing field. The dc field dependence of the flux noise resembles that, at the same temperature and field ranges, of χ''.

In a region where the response of the ac susceptibility is linear in field, χ'' and $S_\phi(f)$ are related by the fluctuation–dissipation theorem

$$S_\phi(f, T, H_{dc}) = 2k_B T \frac{\chi''(f, T, H_{dc})}{\pi f} , \tag{7.1}$$

where k_B is Boltzmann constant. Fig. 36 shows a comparison between the magnetic noise and the ac-susceptibility via the fluctuation dissipation theorem. It is remarkable to note the almost perfect mapping between the ac susceptibility and the zero field noise was achieved. The validity of the fluctuation dissipation theorem constitutes that the noise measurements have been done in the equilibrium.

Since $\chi''(f)$ depends on f weakly, from Eq. (7.1) we have $S_\phi(f) \sim 1/f$. The experiments of Magnusson et al. show that this quantity scales with f as $1/f^\alpha$ where α is close to 1 indicating that the noise may be a flicker noise and arose from the distribution of activation energies of the vortex hopping. Since the $1/f$ noise has been also observed in spin glasses [264] one may suggests that the PME is relevant to some glassy phase like a chiral glass one.

Simulation. AC susceptibilities may be monitored by applying the external magnetic ac field. Then the external field H containing the dc and ac parts is given by

$$H = H_{dc} + H_{ac}\cos(\omega t)\ . \tag{7.2}$$

In general, the dc field is necessary to generate even harmonics. The real and imaginary parts of nth order harmonics $\chi'_n(\omega)$ and $\chi''_n(\omega)$ are calculated as

$$\chi'_n(\omega) = \frac{1}{\pi h_{ac}} \int_{-\pi}^{\pi} m(t)\cos(n\omega t)\,\mathrm{d}(\omega t)\ ,$$

$$\chi''_n(\omega) = \frac{1}{\pi h_{ac}} \int_{-\pi}^{\pi} m(t)\sin(n\omega t)\,\mathrm{d}(\omega t)\ . \tag{7.3}$$

For the system described by the multiloop model (4.5) the magnetization $m(t)$ is given by Eq. (4.10), the dimensionless ac field h_{ac} is related to H_{ac} via (4.12).

The linear ac susceptibility and higher harmonics of ceramic s-wave superconductors have been intensively studied using the Bean model [265], Kim model [266] and a network of resistively shunted Josephson junctions [267,268]. Very little theoretical and simulation work has been done in this direction for d-wave superconductors, although such work would be vital to interpret experimental data [261–263].

The ac susceptibility of a d-wave ceramic superconductor was computed [145] by Monte Carlo simulations with the help of Hamiltonian (4.5) and Eq. (7.3) with $n = 1$. While Monte Carlo simulations involve no real dynamics, one can still expect that they give useful information on the long-time behavior of the system. In fact, the characteristic time for the sintered samples, which are believed to be captured by our model, is of order 10^{-12} s [267]. This time has the same order of magnitude as a single Monte Carlo step. In general, the period of oscillations is much longer than the characteristic time [145]. For such a slowly changing ac field the system can be regarded as being in quasi-equilibrium and the Monte Carlo updating may be applied. A priori, the validity of this approximation is not clear but it may be justified [269] by comparing the Monte Carlo results with those obtained by other approaches to the dynamics such as considered in Ref. [267].

A qualitative agreement between simulations [145] and experiments [261,262] was achieved, e.g., for the dependence of χ' and χ'' on temperature and the ac field. Namely, as H_{ac} is increased, χ'' grows and its peak shifts towards lower temperatures, while χ' becomes less and less diamagnetic. Simulations [145] showed that at high frequencies there is very little difference between the χ of the s- and d-wave models. At low frequencies, clear differences have been seen: The magnitude of χ'' of the s-wave model becomes an order of magnitude smaller than that of the d-wave model,

indicating that the d-wave system exhibits much stronger dissipation. A close similarity observed between the χ'' of d-wave superconductors and that of the spin glass [145] is consistent with the chiral glass picture as well as with experimental findings [261].

It would be highly desirable to check the validity of the fluctuation dissipation theorem (7.1) and verify whether the $1/f$-noise occurs in a system showing the PME by simulations. This may be done in the framework of the multiloop model (4.5).

7.2. Compensation effect

Experiment. Heinzel et al. [23] have shown that the PME may be analysed by the compensation technique based on the measurement of the second harmonics of the magnetic ac susceptibility. The essence of the so called compensation effect is that the second harmonics signal vanishes at some compensation field H_{com} even a nonzero dc field is applied. This is a bit surprising because even harmonics should be generated in the presence of the dc field due to $M(H) = -M(-H)$ symmetry.

The compensation effect may be detected in the following way. The sample is cooled in the external dc field down to a low temperature and then the field is switched off. At the fixed low T the second harmonics are monitored by applying the dc and ac fields to the sample.

The results obtained for PME sample $YBa_2Cu_3O_7$ are shown in Fig. 37 where $H_{com} \approx 15$ Oe. The observed intersection of χ_2' and χ_2'' at $H_{dc} = H_{com}$ indicates a change of their sign. The key observation

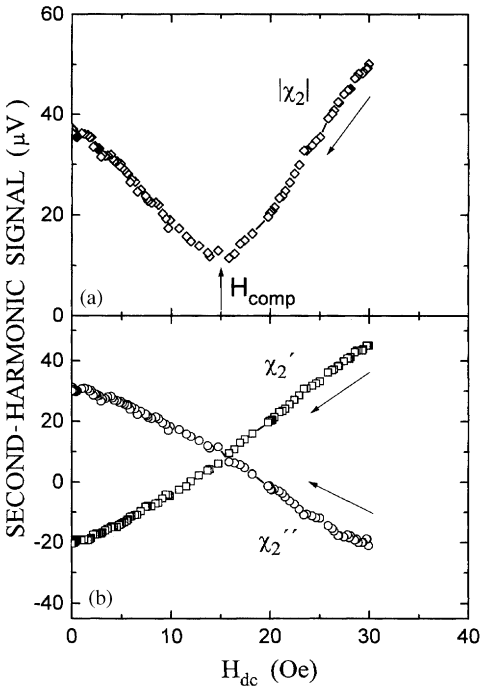

Fig. 37. Second harmonics of the magnetic ac susceptibility ($H_{ac} = 1$ Oe) obtained for $YBa_2Cu_3O_7$ after field cooling in a dc field $H_{dc} = 30$ Oe to $T = 77$ K and stepwise reducing H_{dc}. (a) Modulus $|\chi_2|$ of the complex harmonics. (b) Real (χ_2') and imaginary (χ_2'') parts of the second harmonics. After Heinzel et al. [23].

is that the compensation effect appears only in the samples which show the PME but not in those which do not. It may be explained in the following way. Due to the presence of non-zero spontaneous orbital moments and the frustration, the remanent magnetization or, equivalently, the internal field is generated in the cooling process. If the direction of the external dc field is identical to that during the FC procedure, the induced shielding currents will reduce the remanence. Consequently, the absolute value of the second harmonics $|\chi_2|$ decreases until the signal of the second harmonics is minimized at a field $H_{dc} = H_{com}$. Thus the study of the compensation effect allows us to establish not only the existence of the spontaneous orbital moments but also to determine internal fields generated during the cooling process. The compensation effect is a collective phenomenon and it may be captured by the multi-loop model of 0 and π-junction network.

Simulation. We now present the Monte Carlo simulation results [269] explaining the compensation effect [23] in ceramic superconductors. Again we employ model (4.5) and Eq. (7.3) ($n = 2$) to compute the second harmonics. The calculations follow exactly the experimental procedure of Heinzel et al. [23]. In the FC regime, first the system is cooled in some dc field $h_{dc} \neq 0$ from a high T down to a low T which is below the paramagnet-chiral glass transition temperature [269]. When the lowest temperature is reached the dc field used in cooling is switched off and we apply the combined field given by Eq. (7.2). We monitor the second harmonics reducing the dc field from a high dc field to zero stepwise. Fig. 38 shows the typical behavior of the second harmonics for the

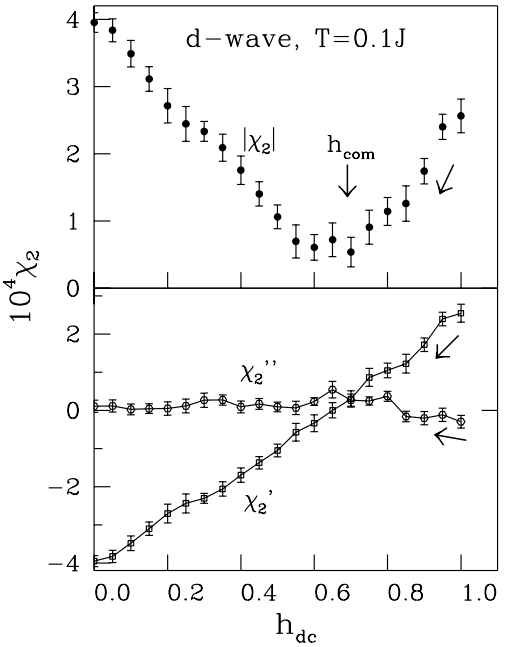

Fig. 38. The second harmonics of the d-wave model (4.5) obtained after field cooling in a dc field $h_{dc} = 1$ from $T = 0.7$ to $T = 0.1$. At the lowest $T = 0.1$ ($< T_{CG} \approx 0.17$ for $\tilde{L} = 4$) the dc field used in cooling is switched off and the second harmonics are generated by applying the combined dc and ac fields. The dc field is stepwise reduced from $h_{dc} = 1$ to $h_{dc} = 0$. The inductance is chosen to be equal to $\tilde{L} = 4$ and system size $l = 8$. The arrows indicate the sense of the changes in the dc field. The results are qualitatively the same as those presented in Fig. 37. After Ref. [269].

d-wave ceramic superconductors. $|\chi_2|$ reaches minimum at the compensation field $h_{com} = 0.7 \pm 0.05$. At this point, similar to the experimental findings presented in Fig. 37 [23], the intersection of χ_2' and χ_2'' is observed. This fact indicates that at H_{com} the system is really in the compensated state. Furthermore, in accord with the experiments, at the compensation point the real and imaginary parts should change their sign [23]. Our results show that χ_2' changes its sign roughly at $h_{dc} = h_{com}$. A similar behavior is also displayed by χ_2'' but it is harder to observe due to a smaller amplitude of χ_2''.

Performing simulations in the same way as for the d-wave case, one cannot observe the compensation effect for the s-wave model [269] because the cooling of a unfrustrated "ferromagnetic" system could not produce any remanent dc field which would compensate the external one. This result is again in accord with the experimental data [23].

Thus, the compensation effect may be explained, at least qualitatively, by using the multiloop model of the ceramic superconductors with anisotropic pairing symmetry. The existence of the compensation phenomenon only in those samples showing the PME indirectly support the chiral glass phase in these materials.

7.3. Aging phenomenon

Experiment. The aging phenomenon observed first in spin glasses [270] have been studied both theoretically [271] and experimentally [264] in detail. In this phenomenon the physical quantities depend not only on the observation time but also on the waiting time (or age), t_w, i.e. how long one waits at constant field or temperature before measurements. The origin of such memory phenomena relates to the rugged energy landscape which appears due to disorder and frustration [144].

Overall, one can explain the aging effect qualitatively in the following way. After the waiting time t_{w1} and t_{w2}, e.g., the system gets trapped, in principle, in different local minima as shown in Fig. 39. Since the corresponding energy barriers are different the physics should depend on in what local minimum the system was before one starts to do measurements. It should be stressed that both the waiting and measurement times are typically much shorter than the relaxation time which

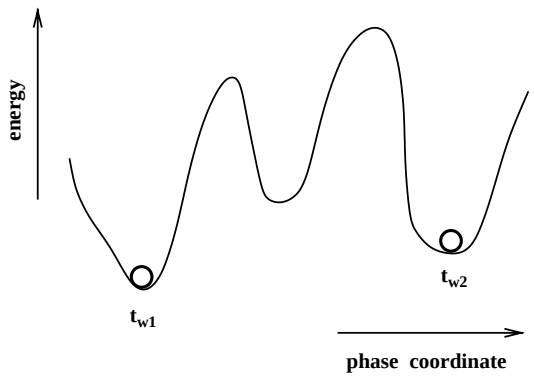

Fig. 39. Schematic energy landscape of a frustrated system in the phase space. After waiting times t_{w1} and t_{w2} the system gets trapped in different local minima.

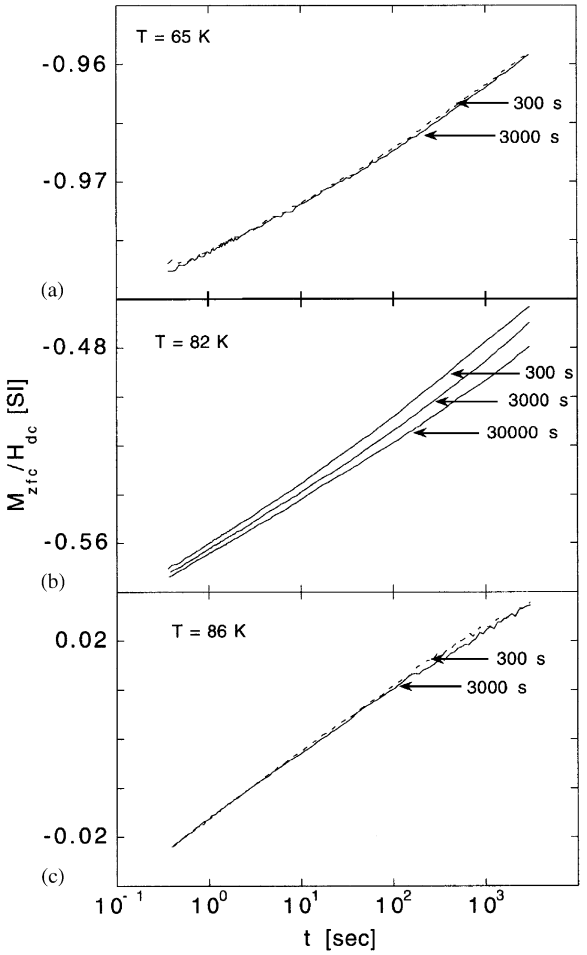

Fig. 40. M_{zfc}/H_{dc} of the melt-cast $Bi_2Sr_2CaCu_2O_8$ sample is plotted vs. observation time for $H_{dc} = 0.02$ G at temperatures (a) 65 K, (b) 82 K, and (c) 86 K. The waiting time used were 300 and 3000 s; in (b) the result for $t_{wait} = 30000$ s is also included. From Papadopoulou et al. [24].

may be astronomically large for a frustrated system [144]. The aging is, therefore, a nonequilibrium phenomenon.

Recently, Papadopoulou et al. [24,272] has observed the aging effect in the PME sample $Bi_2Sr_2CaCu_2O_8$ monitoring the ZFC magnetization. The relaxation of the ZFC magnetization has been measured by cooling the sample in zero field to the measuring temperature, allowing the sample to stay at that temperature for a certain time t_w and then applying the probing field and recording the change of the magnetization with observation time at constant temperature. Papadopoulou et al. have made two key observations. First, the aging effect is not observed at high fields and at high temperatures. Second, this effect occurs at some intermediate temperature interval (see Fig. 40) and it disappears again at low temperatures. Thus the aging phenomenon exists only for weak enough fields and in an intermediate temperature region.

The first observation is trivial because at high fields or high temperatures the roughness of the energy landscape does not play any crucial role and the system looses its memory. At low temperatures the role of the energy landscape becomes important, the second result of Ref. [24] is, therefore, not trivial from the point of view of the standard spin glass theory. Papadopoulou et al. suggested that at low temperatures the external field is screened from the bulk of the sample and it cannot probe the collective behavior of the Josephson junction network. As one can see below, the correctness of this idea may be confirmed using the multi-loop model (4.5).

The results from aging measurements are in immediate contrast to models explaining the PME as a flux compression phenomenon [19,21] which are only applicable to the positive FC magnetization observed in some conventional superconductors. The aging phenomenon in the melt-cast samples [24], with similarities to the aging in spin glasses, implies the interaction between spontaneous magnetic moments causing them to behave collectively. Inside each of the large grains of a sample there can exist many thousands of domains, and the intragrain regions can be, therefore, modeled as Josephson networks containing a random distribution of ordinary Josephson junctions and π junctions.

Simulation. The study of the aging phenomenon in spin glasses by computer simulations lasts for may years [273]. Our aim is not to present those results but to focus on the explanation [274] of specific features of the aging in granular superconductors observed by Papadopoulou et al. [24].

To understand the experiments [24] we use the model (4.5) for a d-wave superconductor. The dependence of the magnetization $m(t)$ given by Eq. (4.10) on the waiting time was computed by the Monte Carlo simulations [274]. In order to mimic the aging effect in the ZFC regime we quench the system from a high temperature to the working temperature. The system is there evolved in zero field during a waiting time, t_w. Then the external field h is turned on and the subsequent growth of the magnetization $M(t, t_w)$ is monitored.

One can demonstrate [274] that there are three screening regimes for the aging phenomenon. In the strong screening limit when $\tilde{L} > \tilde{L}_2^* = 9 \pm 0.5$, the aging is suppressed at any temperature. In the weak screening regime, $\tilde{L} < \tilde{L}_1^* = 3.5 \pm 0.5$, it is observable even at low temperatures. The intermediate screening regime, $\tilde{L}_1^* < \tilde{L} < \tilde{L}_2^*$, is found to be the most interesting: the aging is present only in an intermediate temperature interval and it does not appear at low temperatures.

Fig. 41 shows the results for $\tilde{L} = 7$ belonging to the intermediate screening regime. In agreement with the experiments [24], the aging effect appears only for the intermediate temperature interval. At low T's ($T \leqslant T^* = 0.02 \pm 0.01$) the effect is suppressed due to the screening of the magnetic field from the bulk. The results have been obtained for the observation times comparable with the waiting ones but we believe that they should be valid for longer observation time scales [274].

It should be stressed that the experimental finding of Papadopoulou et al. [24] cannot be explained by the standard XY model where the screening effect is not taken into account. The mechanism of aging may be understood from studies the spatial distribution of flux inside a sample [274]. In fact, in the strong screening limit the aging effect does not occur at any temperature because the external field is screened entirely. For a fixed screening strength the magnetic field is expelled more and more from the bulk as T is lowered. Therefore, for the intermediate values of screening one could not observe the aging at low T's.

The fact that the increase of the self-inductance would wash out the aging effect may be explained by exploring the effect of screening on the energy landscape [275]. Studies of local minima at $T = 0$ showed that the energy landscape gets smoother and smoother as the screening is enhanced and the glassy effects would become less pronounced.

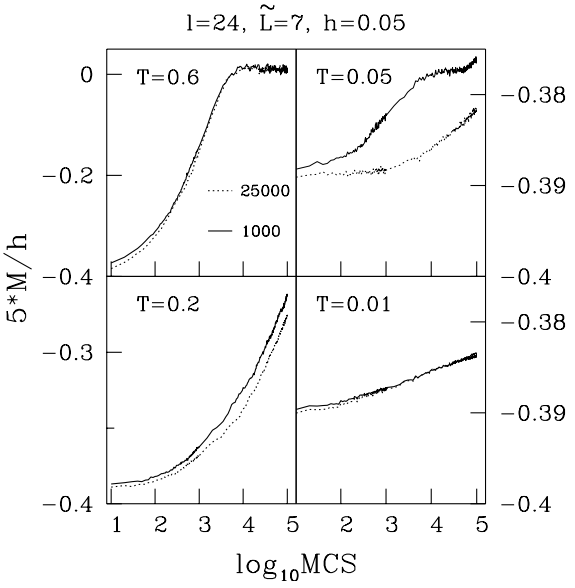

Fig. 41. The temperature and time dependence of M for $t_w = 1000$ and $t_w = 25000$. $l = 24$, $\tilde{L} = 7$ (intermediate screening regime) and $h = 0.05$. The aging disappears at low temperatures. The results are averaged over 60–120 samples. From Li et al. [274].

So, the non-trivial aging phenomenon in ceramic superconductors may be understood in the framework of the model (4.5) where the anisotropy of the pairing function plays a key role. The observation of aging and the PME in the same material does yield support, therefore, for the existence of d-wave superconductivity. Furthermore the PME dynamics owns the characteristics features of the non-equilibrium dynamics of spin glasses. The results on aging are thus indicative of the formation of a low temperature glassy phase in a system showing a pronounced PME, a phase that resembles the chiral glass phase [26,27].

7.4. Anomalous microwave absorption

Experiment. MWA measurements are a sensitive tool for detection of the transport properties of high-T_c superconductors below the critical temperature, when superconducting paths are risen and dc measurements cease to give information. Soon after the discovery of high-T_c superconductivity it has been established [276–280], that in ceramic samples there exists a large non-resonant MWA in zero and low applied magnetic field that can be associated with the transition to the superconducting phase. In fields below H_{c1} the MWA of high-T_c materials is due to dissipative flux motion in the link network or, equivalently, due to the junction's resistance.

Braunish et al. [3,4,281] found a striking correlation between the field dependence of the MWA and the PME. Their typical results are shown in Fig. 42. Clearly, in the absence of the PME the MWA has a conventional minimum at $H = 0$ and in low fields $P(H) \sim H^2$. The change over from the quadratic to linear behavior appears at H_{c1}^* associated with the critical field, at which the magnetic flux breaks into the weak-link network [4]. Contrary to non-PME samples the MWA of

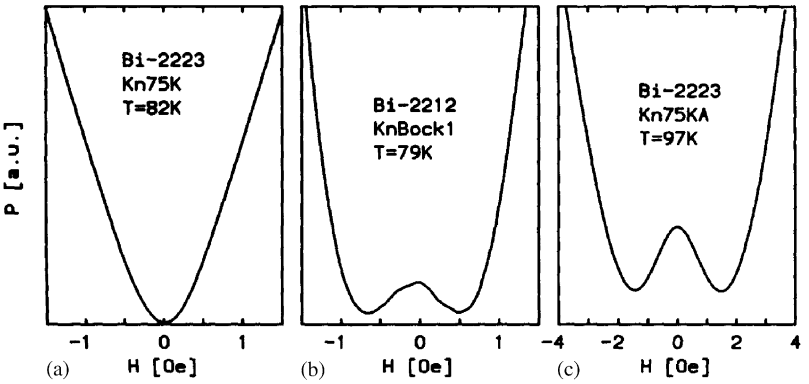

Fig. 42. (a) The field dependence of the MWA for a powdered HTSC sample which does not show the PME. The changeover from parabolic to linear occurs around 0,6 Oe. (b) The same as in (a) but for the PME sample. The minima are located at ±0.6 Oe, near the field where the FC signal changes from diamagnetic to paramagnetic. (c) The MWA signal of a Bi-2223 sample showing a weak PME. From Ref. [4].

PME samples show a maximum at $H = 0$ and it reaches minimum at a field near which the FC signal changes from paramagnetic to diamagnetic behavior [282].

Simulation. The unusual behavior of the MWA may be explained in the framework of a single-loop model [9]. If the loop contains a π junction, then the spontaneous internal field is generated. In the absence of the external field, the microwave field is coupled to this field and dissipates energy. As a static field is turned on, the oscillatory field loses gradually its access to the spontaneous moments and the absorption power decreases. If the dc field is strong enough the π junction loop would behave like a 0 junction one, leading to the increase of the power. The absorption minimum should be located at $H \approx \Phi_0/4S$ [9], i.e. between the fields making the centers between the first maximum and minimum of the free energy shown in Fig. 19.

The general scheme to study the MWA in an Josephson junction networks may be found, for example, in Ref. [283]. Here we follow a simpler approach [284]. Namely, in order to reproduce the anomalous behavior of the absorption power we use the resistively shunted junction (RSJ) model [285] combined with the linear response theory [286]. In this formalism the linear response to the external electromagnetic field is proportional to a voltage—voltage correlation function. To get insight on the MWA we calculate quantity P which is proportional to the frequency integral of this correlation function. Then, we have [284]

$$P = \frac{1}{R}\sum_{\mathrm{i}} \langle V_{\mathrm{i}}^2 \rangle \ , \tag{7.4}$$

where $\langle V_{\mathrm{i}}^2 \rangle$ is a mean value of the square of the voltage induced by the thermal noise on each junction and R is the normal resistance of the links.

To calculate V_{i} we use the RSJ model [12] for the current flowing between two grains. The derivation of dynamical equations for this model is given in Appendix B. The full set of equations for the gauge invariant phases θ (see Eq. (B.2) is as follows:

$$\frac{\hbar}{2eR}\frac{\mathrm{d}\theta_\mu(\mathbf{n})}{\mathrm{d}t} = -\frac{2e}{\hbar}J_\mu(\mathbf{n})\sin\theta_\mu(\mathbf{n}) - \frac{\hbar}{2eL}\Delta_\nu^-\left[\Delta_\nu^+\theta_\mu(\mathbf{n}) - \Delta_\mu^+\theta_\nu(\mathbf{n})\right] - \zeta_\mu(\mathbf{n},t) \ . \tag{7.5}$$

Here we use following notation: the site of each grain is at position $\mathbf{n}=(n_x,n_y,n_z)$ (i.e. $i\equiv\mathbf{n}$); the lattice directions are $\mu=\hat{\mathbf{x}},\hat{\mathbf{y}},\hat{\mathbf{z}}$; the link variables are between sites $\mathbf{n}$ and $\mathbf{n}+\mu$ (i.e. link $ij\equiv$ link $\mathbf{n},\mu$); and the plaquettes p are defined by the site $\mathbf{n}$ and the normal direction μ (i.e plaquette $p\equiv$ plaquette $\mathbf{n},\mu$, for example the plaquette $\mathbf{n},\hat{\mathbf{z}}$ is centered at position $\mathbf{n}+(\hat{\mathbf{x}}+\hat{\mathbf{y}})/2$). The forward difference operator $\Delta_\mu^+\theta_v(\mathbf{n})=\theta_v(\mathbf{n}+\mu)-\theta_v(\mathbf{n})$ and the backward operator $\Delta_\mu^-\theta_v(\mathbf{n})=\theta_v(\mathbf{n})-\theta_v(\mathbf{n}-\mu)$ (see Appendix B for more details). Critical currents $J_\mu(\mathbf{n})$ are the same as J_{ij} in Hamiltonian (4.5). The left part of Eq. (7.5) describes the normal current, while the first and second terms in the right part correspond to the supercurrent and screened current, respectively. The Langevin noise current $\zeta_\mu(\mathbf{n},t)$ has Gaussian correlations

$$\langle\zeta_\mu(\mathbf{n},t)\zeta_{\mu'}(\mathbf{n}',t')\rangle=\frac{2k_BT}{R}\,\delta_{\mu,\mu'}\delta_{\mathbf{n},\mathbf{n}'}\delta(t-t')\ . \tag{7.6}$$

The local voltage V_i is then given by

$$V_i=\frac{d\theta_i}{dt}\ . \tag{7.7}$$

Eq. (7.5) describes the overdamped dynamics. One can show that the inertia (capacitive) terms do not change results qualitatively and they are neglected.

The system of differential equations (7.5) is integrated numerically by a second order Runge–Kutta–Helfand–Greenside algorithm for stochastic differential equations [287]. The time step is chosen to depend on $\tilde{L}$ and is equal to $\Delta t=0.1\tau_J$ and $\Delta t=0.1\tau_J\times\tilde{L}$ for $\tilde{L}>1$ and $\tilde{L}<1$, respectively.

The field dependence of the MWA in two-dimensional s- and d-wave disordered superconductors was studied by Dominguez et al. [284]. Similar results have been obtained for three dimensions [275]. Fig. 43 shows the field dependence of the MWA for $T=0.2$ and for various values of $\tilde{L}$. In the case of s-wave superconductors we have the standard minimum at $H=0$ for any value of inductance and T. As expected, $P\sim H^2$ at weak fields.

For the d-wave samples P has the unconventional peak at $H=0$. Contrary to the one-loop model [9] such peak is seen not only for $\tilde{L}>1$ but also for $\tilde{L}\leqslant 1$.

In our model (7.5) the temperature dependence of the critical current is neglected. However, one can show that the dimensionless temperature T chosen in Fig. 43 corresponds to the relevant to experiments real temperature, T_R. In fact, the critical current depends not only on temperature but also on conditions under which samples were prepared. The typical value of the critical current density for ceramic superconductors is $\sim 10^6$ A/m^2 (see, for example, Ref. [280,288–290]). Since the typical size of grains is about 1 μm we have the critical current $I_c\sim 10^{-6}A$. Using $T_R=JT/k_B=\hbar I_cT/2ek_B$ one obtains $T_R/T\sim 100$ K. Clearly, the dimensionless T chosen in Fig. 43 correctly describes the experimental values of temperature [3].

Comparing Fig. 43 with Fig. 42 one can see that the multi-loop model (4.5) correctly captures the experiments of Braunish et al. [3,4]. Furthermore, the height of the peak shown in Fig. 43 is very small: $(P(H=0)-P_{\min})/P_{\min}$ is of order of 10^{-3}. This is also in qualitative agreement with experimental findings [3] that the peak should be low.

7.5. AC resistivity

Experiment. In recent experiments Yamao et al. [30] have measured the ac linear resistivity, ρ_0, and the nonlinear resistivity, ρ_2, of ceramic superconductor $YBa_2Cu_4O_8$. ρ_0 and ρ_2 are defined

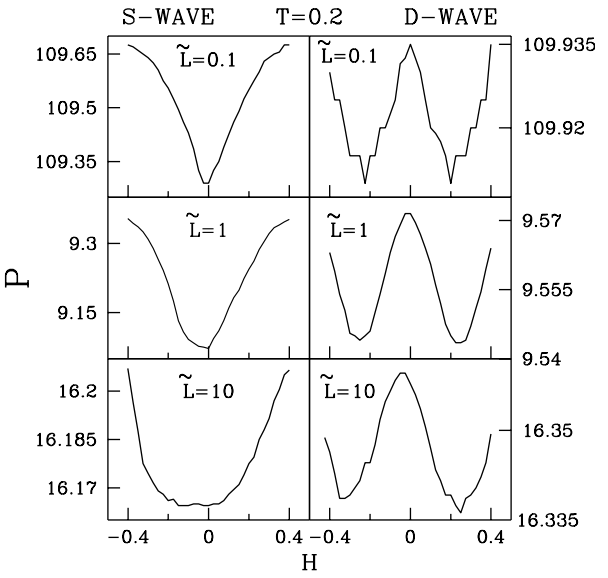

Fig. 43. The field dependence of P for s- (left panel) and d-wave (right panel) ceramic superconductors. We choose $T = 0.2$ and $\tilde{L} = 0.1, 1$ and 10. The results are averaged over 20 samples. After Li [275].

as the first and third coefficient of the expansion of the voltage $V(t)$ in terms of the external current $I_{\text{ext}}(t)$:

$$V = \rho_0 I_{\text{ext}} + \rho_2 I_{\text{ext}}^3 + \cdots \ . \tag{7.8}$$

When the sample is driven by an ac current $I_{\text{ext}}(t) = I_0 \sin(\omega t)$, one can relate ρ_0 and ρ_2 to the first harmonics V'_ω and third harmonics $V'_{3\omega}$ in the following way:

$$\rho_0 = V'_\omega / I_0, \quad \rho_2 = -4V'_{3\omega}/I_0^3 \ ,$$
$$V'_{n\omega} = \frac{1}{2\pi} \int_{-\pi}^{\pi} V(t) \sin(n\omega t)\, d(\omega t), \quad n = 1, 3 \ . \tag{7.9}$$

Fig. 44 shows the temperature dependence of V'_ω / I for $YBa_2Cu_4O_8$ sample around T_{c2} below which the remanent magnetization becomes nonzero [30]. The key observation from this figure is that ρ_0 does not vanish even at and below the intergrain ordering temperature T_{c2}. On the other hand, ρ_2 has a peak near this temperature, which was found to be negative [30] (see Fig. 45).

In the chiral glass phase the $U(1)$ gauge symmetry is not broken and the phase of the condensate remains disordered [27]. The chiral glass phase, therefore, should not be superconducting but exhibit an Ohmic behavior with a finite small resistance. Based on these theoretical predictions Yamao et al. [30] speculated that their results give further support to the existence of the chiral glass phase, in addition to previous results from magnetic susceptibility measurements [29].

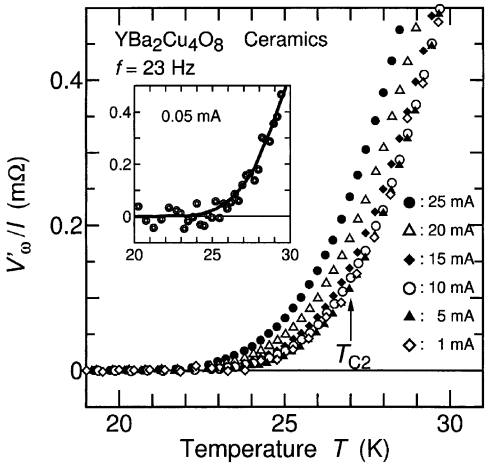

Fig. 44. The temperature dependence of V'_{ω}/I around T_{c2}. Frequency $f = 23$ Hz and values of I are shown in the figure. The inset shows the data measured at $I = 0.05$ mA. The solid line indicates the limiting $\rho_0 - T$ curve. After Yamao et al. [30].

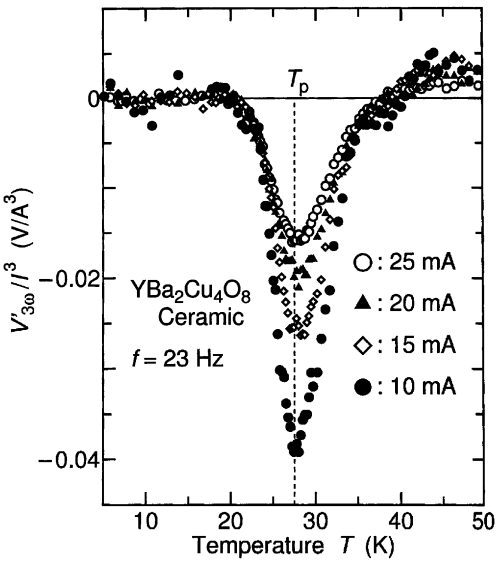

Fig. 45. The temperature dependence of $V'_{3\omega}/I^3$. Frequency $f = 23$ Hz and values of I are shown in the figure. The peak is located at $T_p \approx 27.5$ K. After Ref. [30].

Another interesting result of Yamao et al. [30] is the power law dependence of $|V'_{3\omega}(T_p)/I_0)^3|$ (or of ρ_2) at its maximum position T_p on I_0:

$$|V'_{3\omega}(T_p)/I_0^3| \sim I_0^{-\alpha} \ . \tag{7.10}$$

The experimental value of the power law exponent is $\alpha \approx 1.1$.

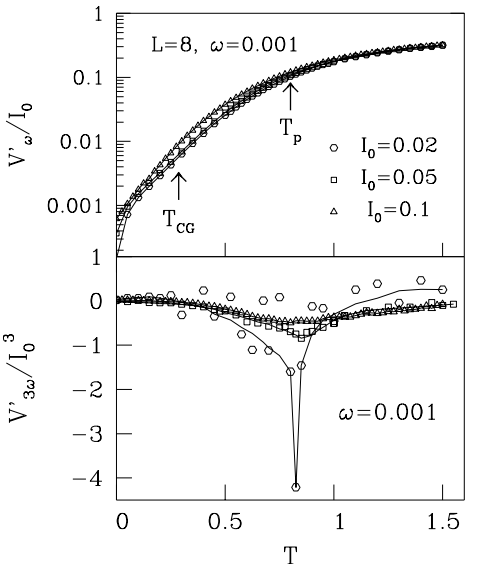

Fig. 46. The temperature dependence of V'_ω/I_0 and $V'_{3\omega}/I_0^3$ of a d-wave superconductor for $l=8, \tilde{L}=1$ and $\omega=0.001$. The open triangles, squares and hexagons correspond to $I_0=0.1, 0.05, 0.02$. The arrows correspond to $T_p=0.8$ and $T_{\rm CG}=0.286$, respectively. The results are averaged over 15–40 disorder realizations. From Li and Dominguez [291].

Simulation. In order to reproduce the experimental results of Yamao et al. [30] we again use the multi-loop model (4.5) combined with the Langevin dynamics equations of the RSJ model which are given by Eq. (7.5). We should add to the right part of these equations the external oscillatory electric field $E_{\rm ext}(t) \propto I_{\rm ext}$ [291]. The details of simulations are given in [291].

Fig. 46 shows the temperature dependence of the linear resistivity $\rho_0 = V'_\omega/I_0$ and the non-linear resistivity $\rho_2 = -4V'_{3\omega}(T)/I_0^3$ for different values of I_0. The linear resistivity is nonzero at the chiral glass transition temperature $T_{\rm CG}$ as well as at the point T_p where the nonlinear resistivity has maximum. The results for ρ_0 presented in Fig. 46 were obtained for the system size $l=8$ but one can show [291] that they are valid in the thermodynamic limit. Thus, the fact that ρ_0 does not vanish at T_p is in full agreement with the experiments [30]. The other observation from simulations [291] is that T_p coincides with a temperature where the FC magnetization starts to departure from the ZFC one. This is also consistent with the experimental findings of Yamao et al. [30].

As said above Yamao et al. have made an interesting conjecture that the peak of the nonlinear resistivity should correspond to the phase transition to the chiral-glass phase. $T_{\rm CG}$ and T_p are, however, well separated (see Fig. 46) suggesting that the peak in the nonlinear resistivity may not be indicative for the existence of the chiral-glass state. One of possible interpretations of simulation results is that T_p just separates the normal state phase from a "chiral paramagnet" where there exist local chiral-magnetic moments. These moments can be polarized under an external magnetic field, an therefore one can observe the PME under a low external field below T_p. At a lower temperature, collective phenomena due to the interactions among the chiral moments will start to be important, leading to the transition to the chiral-glass state. This last transition should show up in the nonlinear chiral-glass susceptibility which diverges at $T_{\rm cg}$ [145].

At present, it is not entirely clear whether T_p corresponds to the chiral-glass transition. Its departure from T_{CG} may be just a shortcoming of the RSJ dynamics.

From lower panel of Fig. 46 one can see that the height of the peak in $\max|V'_{3\omega}/I_0^3|$ grows as the current amplitude decreases supporting the experimental result presented in Fig. 45. A detailed study [292] shows that this dependence can be described by the power law (7.10) which is valid not only for both d-wave and s-wave ceramic superconductors. The exponent α was found to be not universal but depend on the self-inductance and current regimes [292].

In the weak current regime α is independent of the self-inductance and $\alpha = 0.5 \pm 0.1$ for both of s- and d-wave materials. In the s-wave case, since T_p corresponds to a true continuous metal–superconductor phase transition, one can use the scaling argument [221] to obtain the dynamical exponent z via α [292]. In three dimensions $z = 5 - 2\alpha \approx 4$ which is higher than $z \approx 3$ for the corresponding uniform model [202]. For the d-wave system, T_p is the temperature where there is an onset of positive magnetization, i.e. the paramagnetic Meissner effect starts to be observed, but it does not seem to correspond to a phase transition [291]. The scaling analysis is not, therefore, applied.

In the strong current regime [292] the exponent α depends on the screening strength. For the d-wave superconductors and $1 < \tilde{L} < 5$ we have $\alpha \approx 1$ which is close to the experimental value [30]. In order to make the comparison with experiments to be meaningful we show that α was measured in the strong current regime. In fact, the real current is $I = 2eJ/\hbar I_0$, $J \sim 10^2$ K and $I_0 \sim 10^{-1}$ we, therefore, have $I \sim 10^{-2}$ mA which is much weaker than the current $I \sim 10$ mA used in experiments of Yamao et al.. The another issue is that the interval of inductance where $\alpha \approx 1$ is realistic for ceramics [280] because typical values of $\tilde{L}$ are bigger than 3 [280]. An accurate comparison between theory and experiments requires, however, the knowledge of $\tilde{L}$ which is not known for the compound of $YBa_2Cu_4O_8$ studied in Ref. [30].

7.6. Enhancement of critical current

Experiment. The question about enhancement of the critical current of superconductors is important from both the theoretical and application points of view. Several experiments [293,294] in ultrathin (5–10 nm thick) $YBa_2Cu_3O_{7-x}$ films showed that an electric field E may affect T_c as well as the critical current I_c. The later may increase or decrease depending on the polarity of E and this is usually attributed to the changes in the critical current due to variations in the charge density or due to a redistribution of carriers which appear at the surface layer with depths of the order of the electrostatic screening length d_E (in high-T_c superconductors, $d_E \approx 5$ Å). For any experimentally measurable field-induced effects, d_E should be larger than the superconducting coherence length and this happens to the case in ceramics which have a reduced carrier density [293–295].

Recent experiments [25,296–302] revealed, however, that the enhancement of J_c is also possible in bulk (1.5 mm thick) ceramic high-T_c superconductors when E is applied trough an insulating layer (see Fig. 47). This unusual behavior cannot be explained by a surface effect [293,294]. Moreover, for high enough electric fields, the critical current always increases regardless of the polarity of the field.

Using the SNS contact model one can show that an electric field can induce a change in the critical currents of the Josephson junctions in granular samples [303]. However, in this model there is either an enhancement or a deleption of J_c depending on the sign of E. Authors of Ref. [304] have

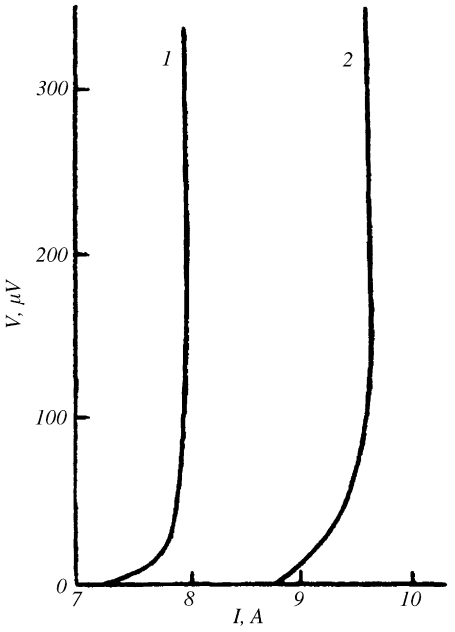

Fig. 47. I–V characteristics for $(BiPb)_2Sr_2Ca_2Cu_3O_x$ sample for $E = 0$ (1) and $E = 120$ mV/m (2). $J_{c0} = 320$ A/cm^2 and $T = 77$ K. After applying the electric field the IV curve is shifted towards higher currents, i.e. the apparent critical current increases. After Smirnov et al. [300].

proposed that an electric field applied to a granular superconductor can produce a magnetoelectric-like effect, which could be indirectly related to the behavior of the critical current observed in [296–299,305–307], but no comparison with the experiments was given.

Simulation. Following Dominguez et al. [308] one can explain the experimental findings on enhancement of the critical current of bulk granular superconductors using the d-wave multi-loop model. In fact, we could employ the full Langevin equations (7.5) but the unusual electric field effects may be captured even neglecting the screening effect ($L = 0$) and thermal fluctuations ($\eta_\mu(\mathbf{n}, t) = 0$). Then the current $J_{\vec{\mu}}(\mathbf{n})$ between to grains $\mathbf{n}$ and $\mathbf{n} + \vec{\mu}$ is a sum of the Josephson supercurrent plus a dissipative Ohmic current [308]

$$J_\mu(\mathbf{n}) = J^0_{\mathbf{n},\mu} \sin\theta_\mu(\mathbf{n}) + \frac{\Phi_0}{2\pi R}\frac{\mathrm{d}\theta_\mu(\mathbf{n})}{\mathrm{d}t} \ , \tag{7.11}$$

where $\theta_\mu(\mathbf{n}) = \phi(\mathbf{n} + \vec{\mu}) - \phi(\mathbf{n}) - A_\mu(\mathbf{n}, t)$ is the gauge invariant phase difference, and $A_\mu(\mathbf{n}, t) = 2\pi/\Phi_0 \int_{\mathbf{n}}^{\mathbf{n}+\mu} \mathbf{A}\,\mathrm{d}\mathbf{l}$. Together with the conditions of current conservation, $\sum_\mu [J_\mu(\mathbf{n}) - J_\mu(\mathbf{n} - \vec{\mu}) = 0$, Eq. (7.11) defines dynamics of the system.

We assume that an electric field $\mathbf{E}$ is applied in the z direction and the network is driven by an external current density I_{ext} along the y direction. Then, in the absence of the external magnetic field, the vector potential $A_\mu(\mathbf{n}, t) = -\delta_{\mu,z}\omega_{\mathrm{E}}t - \delta_{\mu,y}\alpha_y(t)$, where the electric field frequency $\omega_{\mathrm{E}} = 2\pi Ed/\Phi_0$ with d being the intergrain distance or junction thickness [308]. As follows from Eq. (7.11), the

external current density determines the evolution of $\alpha_y(t)$ as

$$I_{\rm ext} = \frac{1}{l^3}\sum_{\mathbf{n}} I^0_{\mathbf{n}y}\sin\theta_y(\mathbf{n}) + \frac{\Phi_0}{2\pi R}\frac{\mathrm{d}\alpha_y}{\mathrm{d}t} \ . \tag{7.12}$$

The average voltage per junction induced by the driving current is then obtained as $V = (\Phi_0/2\pi)\langle \mathrm{d}\alpha_y/\mathrm{d}t\rangle$.

It should be noted that one does not take into account the effects of intergrain and intragrain capacitances in model (7.12) and the screening of the electric field is, therefore, neglected [308]. The electric field scale is $E_0 = RI_0(T=0)/d = \pi\Delta(0)/2ed$, where $\Delta(0)$ is the superconducting energy gap; for the YBaCuO ceramics one has $\Delta(0) \approx 20$ meV, $d \sim 10-20$ Å, which gives $E_0 \sim 30$ MV/m, i.e. in the same range as the fields used in [296–299,305–307]. Dominguez et al. [308] studied two models of disorder. (i) Granular s-wave superconductor: $I^0_{\mathbf{n}\mu}$ is assumed to be a random variable uniformly distributed in the interval $[I_0(1-\Delta_c), I_0(1+\Delta_c)]$ with $\langle I^0_{\mathbf{n}\mu}\rangle = I_0$ and $\Delta_c < 1$. (ii) Granular d-wave superconductor involving 0 and π junctions has the same bimodal distribution for $I^0_{\mathbf{n}\mu}$ as discussed in previous section.

Fig. 48 shows typical simulation results [308] for current–voltage characteristics before and after applying an electric field $\mathbf{E}$ for a s- (left panel) and d-wave (right panel) three-dimensional ceramic superconductor. In the former case after the field is switched on the whole IV curve shifts to lower values of the current indicating the decrease of the apparent critical current and the voltage change $\Delta V = V(E) - V(0)$ is positive for a given current $I > I_c$. This contradicts, however, the experimental finding shown in Fig. 47, where an increase in I_c was seen.

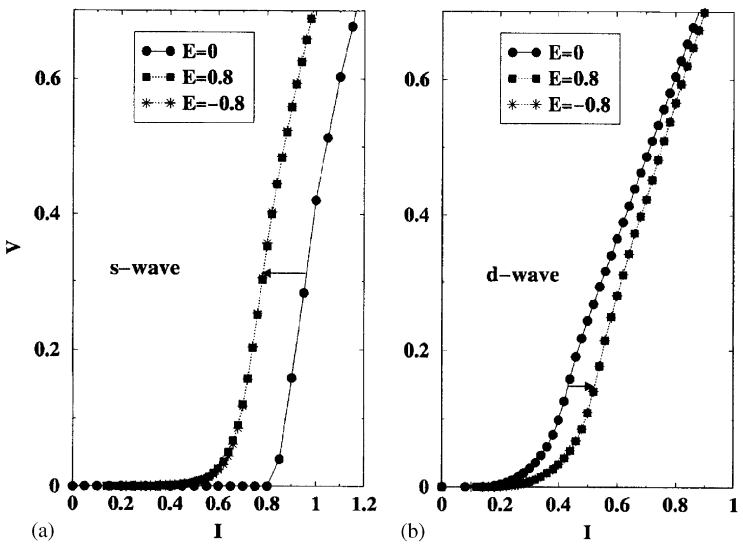

Fig. 48. Current–voltage characteristics before and after applying an electric field $\mathbf{E}$. (a) For a granular s-wave superconductor with $\Delta_c = 0.6$. (b) For a d-wave superconductor with a bimodal distribution of positive and negative Josephson couplings coming from 0 and π junctions. Voltages are normalized by lRI_0 and currents by l^2I_0 and the lattice size $l = 16$. After Dominguez et al. [308].

In the d-wave case, after application of the electric field the IV curve moves towards higher currents, i.e. the apparent critical current *increases*. It is precisely what was observed on experiments (see Fig. 47). Furthermore, if one changes $E \to -E$ the IV curves overlap showing that the effect is independent of the polarity of the electric field. The similar effect was also seen in the experiments [298,299].

There is other interesting aspect of experimental findings that if an applied current is near the critical current then $\Delta V/V_0$ increases as a function of E and, after reaching a maximum, it falls and then becomes negative for large enough fields [297]. This behavior can be also explained in the framework of the d-wave model [12].

Two unexpected results from the experiments on the electric field effects are: (i) a pronounced electric field effect in a bulk ceramic sample and (ii) an increase of the apparent critical current as a function of E independent of the field polarity. All these features are qualitatively captured by the simple d-wave model in which the frustration due to π junction and the ac Josephson effect induced by the electric field are important. It would be interesting to explore the effect of the electric field on the paramagnetic signal, on the chiral glass phase and glassy dynamics in ceramic superconductors [298,299].

8. Summary

We have reviewed the experimental facts, simulations and theories of the PME observed in conventional and ceramic high-T_c superconductors. There exist two main mechanisms for this very interesting phenomenon: the flux compression and the π junction. The later probably occurs due to anisotropic pairing of electrons but other possibilities like the scattering on magnetic impurities in Josephson junctions are not excluded.

From the technical point of view, the paramagnetic signal due to the flux trapping inside a sample of confined geometry may be obtained either by considering the Bean critical model or by solving the nonlinear Ginzburg–Landau equations. In the case of ceramic superconductors with the d-wave symmetry of the order parameter, the spontaneous magnetic moment leading to the PME occurs in the loop of odd number of π junctions. The screening plays a crucial role in both the single loop and multi-loop models. It should be noted that the later can capture not only the PME but also many related dynamical phenomena in granular materials.

The flux compression scenario should work for mesoscopic conventional materials but it may be also applied to granular superconductors where the grain surfaces can play an important role. Therefore, the existence of the PME itself could not serve as an unambiguous indicator for the d-wave symmetry of the order parameter of cuprates. It would be very important to prepare ceramic samples with negligible surface effects to check if the paramagnetic signal can occur or not.

In addition to the phase-sensitive and phase-insensitive experiments, the experiments on the aging, anomalous MWA, $1/f$ flux noise, compensation effect and enhancement of the critical current which may be described by simple XY model with screening (4.5), tend to support the d-wave pairing symmetry of the cuprate superconductors. From both experimental and theoretical points of view it would be very exciting to find out whether these effects appear in conventional superconductors showing the PME.

The chiral-glass phase which may be observed by negative divergence of the nonlinear susceptibility is an interesting example of the time-reversal symmetry breaking. In contrast to the gauge and vortex glass, it appears only in a zero external magnetic field. Furthermore, the moderate screening could not destabilize the chiral glass phase at finite temperatures in three dimensions. Since the experiments [32,29–31,255,260] gave conflicting results on the existence of this phase in high-T_c superconductors, much more work in this direction is left for future studies.

Acknowledgements

We have benefited greatly from discussions with numerous colleagues. We would particularly like to thank D. Dominguez, H. Kawamura, T. Nattermann, P. Nordblad and H. Zung. We are very indebted to P. Janiszewski and M.V. Ba for their kind help in preparing many figures. Financial support from the Polish agency KBN (Grant number 2P03B-146-18) is acknowledged.

Appendix A. Critical self-inductance of the multi-loop model

In order to demonstrate that the critical inductance of the multi-loop model is smaller than that of the single-loop model, we analyse the ground state of an isolated frustrated plaquette, an elementary unit of our lattice model as shown in Fig. 49. The plaquette consists of four bonds (junctions) among which one is a π-junction with negative coupling $-J < 0$, and other three are 0-junctions with positive coupling constant $\varepsilon J > 0$ $(0 < \varepsilon < \infty)$. The multi-loop model considered here corresponds to $\varepsilon = 1$, while $\varepsilon = \infty$ describes a single π junction analysed by Sigrist and Rice [9]. The external field is set equal to 0.

Introducing gauge-invariant phase difference on each bond $\theta_{ij} = \phi_i - \phi_j - A_{ij}$ ("temporal gauge" [12,145]), the dimensionless energy of the plaquette shown in Fig. 49 is

$$F = \mathscr{H}/J = \varepsilon \cos\theta_1 - \cos\theta_2 - \cos\theta_3 - \cos\theta_4 + \frac{1}{\tilde{L}}(\theta_1 + \theta_2 + \theta_3 + \theta_4)^2 \ . \tag{A.1}$$

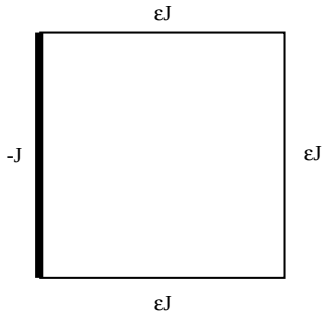

Fig. 49. An isolated frustrated loop consisting of four junctions, one of which is a π junction of magnitude $-J$ (thick line) and the other three are 0-junction of magnitude εJ with $0 < \varepsilon < \infty$. The case $\varepsilon = 1$ corresponds to an elementary frustrated plaquette of the multi-loop model, while $\varepsilon = \infty$ corresponds to the frustrated single-loop model analysed in the previous section.

Here, for simplicity, we drop one sub index of the θ_{ij} and denote the phases as θ_1 at π junction and $\theta_2 - \theta_4$ at 0 junctions. Minimizing F with respect to $\theta_1 - \theta_4$, we get four coupled equations. After a little algebra, one can see that the ground-state configuration should satisfy the relations

$$\theta_2 = \theta_3 = \theta_4 = \theta, \quad \theta_1 = \arcsin(-\varepsilon \sin\theta) \ , \tag{A.2}$$

with θ being determined from the following equation

$$\varepsilon \sin\theta + \frac{1}{\tilde{L}}(3\theta + \arcsin(-\varepsilon \sin\theta)) = 0 \ . \tag{A.3}$$

One can show that if $\varepsilon < 3$, this equation always has doubly degenerate solutions $\theta = \pm\theta^*$ which corresponds to supercurrents with opposite directions. A spontaneous moment, therefore, arises for an arbitrary value of inductance. If ε is larger than three, there appears a finite critical value of the inductance $\tilde{L}_c(\varepsilon) = 1 - 3/\varepsilon$ [145]: for a inductance $\tilde{L} > \tilde{L}_c(\varepsilon)$, there again exist doubly degenerate solutions $\theta = \pm\theta^*$, while for $\tilde{L} < \tilde{L}_c(\varepsilon)$, only trivial solution exists at $\theta = 0$ corresponding to the state without spontaneous supercurrent. In the limit $\varepsilon \to \infty$, one recovers the critical value $\tilde{L}_c = 1$ obtained by Sigrist and Rice [9]. Thus, we have shown that, contrary to the one-loop model, the critical inductance of the interacting loop models with weak links of nearly the same magnitude is equal to $\tilde{L}_c = 0$.

Appendix B. RSJ model

In this appendix we derive the equations of the RSJ model which have been used to study dynamical phenomena such as the MWA, the ac resistivity and the enhancement of the critical current in chapter 7. As shown in the inset of Fig. 50 the RSJ model of a single junction contains the superconducting and resistive parts which are denoted by a cross and a rectangular, respectively. Then the total current I through the junction is [7]

$$I = I_R + I_S = \frac{1}{R}\frac{\Phi_0}{2\pi}\frac{d\theta}{dt} + I_c \sin\theta \ , \tag{B.1}$$

where R and I_c are the resistivity and the critical current of the junction, respectively. The gauge invariant phase θ between points 1 and 2 is

$$\theta_{12} = \int_1^2 d\mathbf{l}\left(\nabla\phi - \frac{2\pi}{\Phi_0}\mathbf{A}\right) \ , \tag{B.2}$$

where $\nabla\phi$ is the gradient of the phase of macroscopic wave function, $\mathbf{A}$ is the vector potential, and the line integration is taken between two sides of the junction with sign convention in accordance with the coordinate directions shown in Fig. 50.

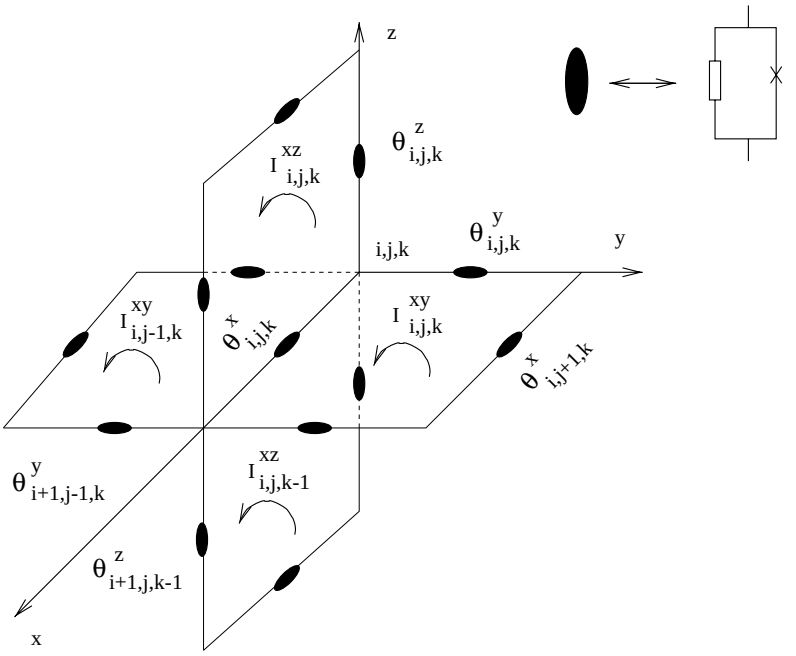

Fig. 50. Schematic description of the three-dimensional RSJ model of the Josephson junction network. The gauge invariant phases are marked on some representative junctions. The θ^{μ} values grow in the positive directions the corresponding axis $\mu = x, y, z$. The positive direction of currents circulating in loops is chosen to be counterclockwise. The inset shows a single junction containing the resistive and superconducting parts.

We now consider the three-dimensional network on a cubic lattice shown in Fig. 50. Representing the current flowing from point (i,j,k) in direction μ to the nearest point as $I^{\mu}_{i,j,k}$, from Eq. (B.1) we have [285]

$$I^{\mu}_{i,j,k} = \frac{1}{R}\frac{\Phi_0}{2\pi}\frac{\mathrm{d}\theta^{\mu}_{i,j,k}}{\mathrm{d}t} + I^{\mu}_{i,j,k\mathrm{c}}\sin\theta^{\mu}_{i,j,k}, \quad \mu = x, y, z \ , \tag{B.3}$$

where $\theta^{\mu}_{i,j,k}$ is the gauge invariant phase between points (i,j,k) and its nearest neighbor in direction μ. $I^{x}_{i,j,k}$ is, e.g., the current from (i,j,k) to $(i+1,j,k)$ (see Fig. 50) and $I^{\mu}_{i,j,k\mathrm{c}}$ is the local critical current.

The crucial point here is that $I^{\mu}_{i,j,k}$ consists of contributions from four loops sharing the corresponding junction and we, therefore, have

$$\begin{aligned} I^{x}_{i,j,k} &= I^{xy}_{i,j,k} - I^{xy}_{i,j-1,k} + I^{xz}_{i,j,k-1} - I^{xz}_{i,j,k} \ , \\ I^{y}_{i,j,k} &= I^{yz}_{i,j,k} - I^{yz}_{i,j,k-1} + I^{xy}_{i-1,j,k} - I^{xy}_{i,j,k} \ , \\ I^{x}_{i,j,k} &= I^{xz}_{i,j,k} - I^{xz}_{i-1,j,k} + I^{yz}_{i,j-1,k} - I^{yz}_{i,j,k} \ . \end{aligned} \tag{B.4}$$

Labeling the flux $\Phi^{\mu\nu}_{i,j,k}$ threading through loop (i,j,k) in $\mu\nu$-plane in the same manner as $I^{\mu\nu}_{i,j,k}$ we have

$$\Phi^{xy}_{i,j,k} = \frac{\Phi_0}{2\pi}\left(\theta^x_{i,j,k} + \theta^y_{i+1,j,k} - \theta^x_{i,j+1,k} - \theta^y_{i,j,k}\right) ,$$

$$\Phi^{xz}_{i,j,k} = \frac{\Phi_0}{2\pi}\left(\theta^z_{i,j,k} + \theta^x_{i,j,k+1} - \theta^z_{i+1,j,k} - \theta^x_{i,j,k}\right) ,$$

$$\Phi^{yz}_{i,j,k} = \frac{\Phi_0}{2\pi}\left(\theta^y_{i,j,k} + \theta^z_{i,j+1,k} - \theta^y_{i,j,k+1} - \theta^z_{i,j,k}\right) . \tag{B.5}$$

For the cubic array containing $l \times l \times l$ junctions fluxes (B.5) are defined for following values of (i,j,k):

$$\Phi^{xy}_{i,j,k}\colon\ 0 \leqslant i \leqslant l-1; 0 \leqslant j \leqslant l-1; 0 \leqslant k \leqslant l\ ;$$

$$\Phi^{xz}_{i,j,k}\colon\ 0 \leqslant i \leqslant l-1; 0 \leqslant j \leqslant l; 0 \leqslant k \leqslant l-1\ ;$$

$$\Phi^{yz}_{i,j,k}\colon\ 0 \leqslant i \leqslant l; 0 \leqslant j \leqslant l-1; 0 \leqslant k \leqslant l-1\ . \tag{B.6}$$

The corresponding restrictions on (i,j,k) for phases are

$$\theta^x_{i,j,k}\colon\ 0 \leqslant i \leqslant l-1; 0 \leqslant j \leqslant l; 0 \leqslant k \leqslant l\ ;$$

$$\theta^y_{i,j,k}\colon\ 0 \leqslant i \leqslant l; 0 \leqslant j \leqslant l-1; 0 \leqslant k \leqslant l\ ;$$

$$\theta^z_{i,j,k}\colon\ 0 \leqslant i \leqslant l; 0 \leqslant j \leqslant l; 0 \leqslant k \leqslant l-1\ . \tag{B.7}$$

Assuming the self-inductances of all loops to be identical and equal to L one has

$$I^{\mu\nu}_{i,j,k} = \begin{cases} (\tilde{\Phi}^{\mu\nu}_{i,j,k} - \tilde{\Phi}^{\mathrm{ext}}_{\mu\nu})/L & \text{for } (i,j,k) \in \text{(B.6)} \\ 0 & \text{otherwise.} \end{cases} \tag{B.8}$$

Here $\Phi^{\mathrm{ext}}_{\mu\nu}$ is a flux threading through a loop in $\mu\nu$-plane which is equal to $\Phi^{\mathrm{ext}}_{\mu\nu} = HS$ if the $\mu\nu$-plane is perpendicular to $\vec{H}$ and $\Phi^{\mathrm{ext}}_{\mu\nu} = 0$ otherwise (see also Eq. (4.6)). Substituting Eq. (B.4), (B.5) and (B.8) into Eq. (B.3) we obtain the full set of equations for gauge invariant phases which is often used to study dynamics of the Josephson junction network at zero temperature. For nonzero temperatures one has to add the Langevin noise term to mimic the effect of the heat bath.

We now show that in the case when the external magnetic field $H = 0$ the Langevin equations for phases may be written in a compact form. Using Eq. (4.7) and $\Phi_0 = hc/2e$ one has

$$I^{\mu}_{i,j,kc} = \frac{2e}{\hbar c} J^{\mu}_{i,j,k} , \tag{B.9}$$

where $J^{\mu}_{i,j,k}$ is the Josephson couplings. From Eqs. (B.3), (B.4), (B.5), (B.8) and (B.9) we obtain the following equation for $\theta^x_{i,j,k}$:

$$\frac{\hbar}{2eR}\frac{d\theta^x_{i,j,k}}{\mathrm{d}t} = -\frac{2e}{\hbar c^2} J^x_{ijk} \sin\theta^x_{i,j,k} - \frac{\hbar}{2eL}[(\theta^x_{i,j,k} + \theta^y_{i+1,j,k} - \theta^x_{i,j+1,k} - \theta^y_{i,j,k})$$

$$-(\theta^x_{i,j-1,k}+\theta^y_{i+1,j-1,k}-\theta^x_{i,j,k}-\theta^y_{i,j-1,k})$$
$$+(\theta^z_{i,j,k-1}+\theta^x_{i,j,k}-\theta^z_{i+1,j,k-1}-\theta^x_{i,j,k-1})$$
$$-(\theta^z_{i,j,k}+\theta^x_{i,j,k+1}-\theta^z_{i+1,j,k}-\theta^x_{i,j,k})]\ . \tag{B.10}$$

Equations for $\theta^y_{i,j,k}$ and $\theta^z_{i,j,k}$ can be written in a similar form. For the sake of convenience we represent (i,j,k) by vector $\mathbf{n}$ and redefine $\theta^\mu_{i,j,k}\to\theta_\mu(\mathbf{n})$ and $J^\mu_{i,j,k}\to J_\mu(\mathbf{n})$. We introduce also the forward operator Δ^+_μ and backward operator Δ^-_μ which act on $\theta_\nu(\mathbf{n})$ in the following way:

$$\Delta^+_\mu\theta_\nu(\mathbf{n})=\theta_\nu(\mathbf{n}+\mu)-\theta_\nu(\mathbf{n})\ ,$$
$$\Delta^-_\mu\theta_\nu(\mathbf{n})=\theta_\nu(\mathbf{n})-\theta_\nu(\mathbf{n}-\mu)\ . \tag{B.11}$$

In the (i,j,k)-representation the last equation takes the form

$$\Delta^+_x\theta^\nu_{i,j,k}=\theta^\nu_{i+1,j,k}-\theta^\nu_{i,j,k},$$
$$\Delta^-_x\theta^\nu_{i,j,k}=\theta^\nu_{i,j,k}-\theta^\nu_{i-1,j,k} \tag{B.12}$$

for component $\mu=x$. Similar equations for $\mu=y$ and z can be easily written down. With the help of Eq. (B.12) one can show that Eq. (B.10) is reduced to Eq. (7.5) in the main text.

References

[1] J.G. Bednorz, K.A. Müller, Possible high-T_c superconductivity in Ba–La–Cu–O system, Z. Phys. B 64 (1986) 189–193.

[2] P. Svelindh, K. Niskanen, P. Nordblad, L. Lundgren, B. Lönnberg, T. Lundström, Anti-Meissner effect in the BiSrCaCuO-system, Physica C 162–164 (1989) 1365–1366.

[3] W. Braunisch, N. Knauf, V. Kataev, S. Neuhausen, A. Grutz, A. Kock, B. Roden, D. Khomskii, D. Wohlleben, Paramagnetic Meissner effect in Bi high-temperature superconductors, Phys. Rev. Lett. 68 (1992) 1908–1911.

[4] W. Braunisch, N. Knauf, G. Bauer, A. Kock, A. Becker, B. Freitag, A. Grutz, V. Kataev, S. Neuhausen, B. Roden, D. Khomskii, D. Wohlleben, Paramagnetic Meissner effect in high-temperature superconductors, Phys. Rev. B 48 (1993) 4030–4042.

[5] B. Schliepe, M. Stindtmann, I. Nikolic, K. Baberschke, Positive field-cooled susceptibility in high-T_c superconductors, Phys. Rev. B 47 (1993) 8331–8334.

[6] D.I. Khomskii, Wohlleben effect (paramagnetic Meissner effect) in high-temperature superconductors, J. Low Temp. Phys. 95 (1994) 205–223.

[7] M. Tinkham, Introduction to Superconductivity, MacGraw-Hill, New York, 1996.

[8] F.V. Kusmartsev, Destruction of the Meissner effect in granular high-temperature superconductors, Phys. Rev. Lett. 69 (1992) 2268–2271.

[9] M. Sigrist, T.M. Rice, Paramagnetic effect in high-T_c superconductors—a hint for d-wave superconductivity, J. Phys. Soc. Jpn. 61 (1992) 4283–4286.

[10] M. Sigrist, T.M. Rice, Unusual paramagnetic Meissner phenomena in granular high-temperature superconductors—a consequence of d-wave pairing? Rev. Mod. Phys. 67 (1995) 503–513.

[11] D.-X. Chen, A. Hernando, Paramagnetic Meissner effect and 0–π Josephson junctions, Europhys. Lett. 26 (1994) 365–370.

[12] D. Domínguez, E.A. Jagla, C.A. Balseiro, Phenomenological theory of the paramagnetic Meissner effect, Phys. Rev. Lett. 72 (1994) 2773–2776.

[13] K.N. Shrivastava, Para-Meissner effect in high-temperature superconductors, Solid State Commun. 90 (1994) 589–594.

[14] K.N. Shrivastava, Para-Meissner oscillations in the magnetization of a high-temperature superconductor, Phys. Lett. A 188 (1994) 182–186.
[15] C.C. Tsuei, J.R. Kirtley, Pairing symmetry in cuprate superconductors, Rev. Mod. Phys. 72 (2000) 969–1016.
[16] D.J. Thompson, M.S.M. Minhaj, L.E. Wenger, J.T. Chen, Observation of paramagnetic Meissner effect in Niobium disks, Phys. Rev. Lett. 75 (1995) 529–532.
[17] P. Kostic, B. Veal, A.P. Paulikas, U. Welp, V.R. Todt, C. Gu, U. Geiser, J.M. Williams, K.D. Carlson, R.A. Klemm, Paramagnetic Meissner effect in Nb, Phys. Rev. B 53 (1996) 791–801.
[18] A.K. Geim, S.V. Dubonos, J.G.S. Lok, M. Henini, J.C. Maan, Paramagnetic Meissner effect in small superconductors, Nature 396 (1998) 144–146.
[19] A.E. Koshelev, A.I. Larkin, Paramagnetic moment in field-cooled superconducting plates—paramagnetic Meissner effect, Phys. Rev. B 52 (1995) 13559.
[20] A.E. Khalil, Inversion of Meissner effect and granular disorder in $Bi_2Sr_2CaCu_2O_{8+\delta}$ superconductors, Phys. Rev. B 55 (1997) 6625–6630.
[21] V.V. Moshchalkov, X.G. Qui, V. Bruyndoncz, Paramagnetic Meissner effect from the self-consistent solution of the Ginzburg–Landau equations, Phys. Rev. B 55 (1997) 11793–11801.
[22] M. Sigrist, Superconductors: mesoscopic magnetism, Nature 396 (1998) 110–111.
[23] Ch. Heinzel, Th. Theilig, P. Ziemann, Paramagnetic Meissner effect analysed by second harmonics of the magnetic susceptibility: consistency with a ground state carrying spontaneous current, Phys. Rev. B 48 (1993) 3445–3454.
[24] E.I. Papadopoulou, P. Nordblad, Svendlindh, S. Schöneberger, R. Gross, Magnetic aging in $Bi_2Sr_2CaCu_2O_8$ displaying the paramagnetic Meissner effect, Phys. Rev. Lett. 82 (1999) 173–176.
[25] T.S. Orlova, B.I. Smirnov, J.Y. Laval, Yu.P. Stepanov, Correlation of the electric field effect with the weak link behavior in granular YBCO superconductors, Supercond. Sci. Technol 12 (1999) 356–359, and references therein.
[26] H. Kawamura, Nature of orbital-glass transition in *d*-wave ceramic superconductors, J. Phys. Soc. Japan 64 (1995) 711–715.
[27] H. Kawamura, M.S. Li, Equilibrium phase with broken time-reversal symmetry in ceramic high-T_c superconductors, Phys. Rev. Lett. 78 (1997) 1556–1559.
[28] J. Villain, Two-level systems in a spin glass model: I. General formalism, two-dimensional model, J. Phys. C 10 (1977) 4793–4803.
[29] M. Matsuura, M. Kawacki, K. Miyoshi, M. Hagiwara, K. Koyama, Negative divergence of nonlinear susceptibility at the intergrain phase ordering transition in a superconductive ceramic $YBa_2Cu_4O_8$, J. Phys. Soc. Japan 64 (1995) 4540–4543.
[30] T. Yamao, M. Hagiwara, K. Koyama, M. Matsuura, Intergrain ordering of a superconductive ceramic of $YBa_2Cu_4O_8$ at zero external magnetic field studied by linear and nonlinear transport coefficients, J. Phys. Soc. Japan 68 (1999) 871–875.
[31] E.I. Papadopoulou, P. Nordblad, P. Svedlindh, Dynamic scaling of granular $Bi_2Sr_2CaCu_2O_8$—evidence of a chiral glass phase transition? Physica C 341–348 (2000) 1379–1380.
[32] T. Ishida, T. Mikayama, K. Okuda, Search for a *d*-wave chiral glass High-T_c superconductors $(Sr_{0.7}Ca_{0.3})_{0.95}CuO_{2-x}$, J. Phys. Soc. Japan 66 (1997) 2256–2259.
[33] B. Freitag, B. Bűchner, N. Kauf, B. Roden, H. Micklitz, A. Freimuth, V. Kataev, Characteristic microstructure in small Bi-2212 grains showing the Wolleben effect as revealed by high-resolution electron microscopy, Europhys. Lett. 45 (1999) 393–398.
[34] S. Riedling, G. Bruchle, R. Lucht, K. Rhberg, H.v. Lhneysen, H. Claus, Observation of the Wohlleben effect in YBa2Cu3O7—delta single crystals, Phys. Rev. B 49 (1994) 13283–13286.
[35] G.S. Okram, D.T. Adroja, B.D. Padalia, Om. Prakash, P.A.J. de Groot, The paramagnetic Meissner effect in superconductors $Nd_{2-x}Ce_xCuO_y$ at 40 G and flux trapping, J. Phys.: Condens. Matter 9 (1997) L525–L531.
[36] F.C. Chou, D.C. Johnston, W-W. Cheong, P.C. Canfield, Preparation, magnetization and electrical resistivity of electrochemically oxidized $La_2CuO_{4+\delta}$ single crystals, Physica C 216 (1993) 66–76.
[37] A.I. Golovashkin, A.V. Gudenko, M.L. Norton, A.M. Tskovrebov, L.N. Zherikina, The anomalous magnetic properties of high-T_c Ba–K–Bi–O in superconducting state, Physica B 284–288 (2000) 779–780.
[38] K. Niskanen, J. Magnusson, P. Nordblad, P. Svedlindh, A.S. Ullström, T. Lundström, Anti-Meissner effect and low field magnetic relaxation in sintered Bi-2212, Physica B 194-196 (1993) 1549–1550.
[39] E.I. Papadopoulou, Ph.D. Thesis, Uppsala University, 2001.

[40] N. Knauf, J. Fischer, B. Roden, R. Borowski, B. Freitag, B. Büchner, H. Micklitz, A. Freimuth, V. Kataev, D.I. Khomskii, Wohlleben effect in small grains of Bi-based high-temperature superconductors: evidence for intrinsic nature of spontaneous currents, Europhys. Lett. 35 (1996) 541–546.
[41] F.V. Kusmartsev, Orbital glass, Phys. Lett. A 169 (1992) 108–114.
[42] R. Lucht, H. von L.-Hohneysen, H. Claus, M. Kläser, G. Müller-Vogt, Surface sensitive paramagnetic Meissner effect in $YBa_2Cu_3O_x$ single crystals, Phys. Rev. B 52 (1995) 9724–9726.
[43] R. Caparroz, P.N. Lisbo-Filho, W.A.C. Passos, W.A. Ortiz, Critical current of tridimensional $La_{1.85}Sr_{0.15}CuO_{4-\delta}$, Physica C 354 (2001) 284–288.
[44] M.S.M. Minhaj, D.J. Thompson, L.E. Wenger, J.T. Chen, Paramagnetic Meissner effect in a Niobium disk, Physica C 235–240 (1994) 2519–2520.
[45] L. Pust, L.E. Wegner, M.R. Koblischka, Detailed investigation of the superconducting transition of niobium disks exhibiting the paramagnetic Meissner effect, Phys. Rev. B 58 (1998) 14191–14194.
[46] F.M. Araujo-Moreira, P. Barbara, A.B. Cawthorne, C.J. Lobb, Reentrant ac magnetic susceptibility in Josephson-junction arrays, Phys. Rev. Lett. 78 (1997) 4625–4628.
[47] P. Barbara, F.M. Araujo-Moreira, A.B. Cawthorne, C.J. Lobb, Reentrant ac magnetic susceptibility in Josephson-junction arrays: an alternative explanation for the paramagnetic Meissner effect, Physical Review B 60 (1999) 7489–7495.
[48] L.E. Wenger, L. Pust, M.R. Koblischka, Investigation of the paramagnetic Meissner effect on Nb disks, Physica C 284-288 (2000) 797–798.
[49] J.R. Clem, Z. Hao, Theory for the hysteretic properties of the low-field dc magnetization in type-II superconductors, Phys. Rev. B 48 (1993) 13774–13783.
[50] A. Terentiev, D.B. Watkins, L.E. de Long, D.J. Morgan, J.B. Ketterson, Paramagnetic relaxation and Wohlleben effect in field-cooled Nb thin films, Phys. Rev. B 60 (1999) R761–R764.
[51] A.K. Geim, et al., Phase transitions in individual sub-micrometre superconductors, Nature 390 (1997) 259–262.
[52] V.A. Schweigert, F.M. Peeters, Phase transitions in thin superconducting disks, Phys. Rev. B 57 (1998) 13817–13832.
[53] V.A. Schweigert, F.M. Peeters, P.S. Deo, Vortex phase diagram for mesoscopic superconducting disks, Phys. Rev. Lett. 81 (1998) 2783–2786.
[54] A.C. Bolech, G.C. Buscaglia, A. Lopez, Numerical simulation of vortex arrays in thin superconducting films, Phys. Rev. B 52 (1995) 15719–15722.
[55] J.J. Palacios, Metastability and paramagnetism in superconducting mesoscopic disks, Phys. Rev. Lett. 84 (2000) 1796–1799.
[56] I.O. Kulik, Magnitude of the critical Josephson tunnel current, Zh. Eksp. Teor. Fiz. 65 (1965) 1211–1214.
[57] H. Shiba, T. Soda, Superconducting tunneling through the barrier with paramagnetic impurities, Prog. Theor. Phys. 41 (1969) 25–44.
[58] L.N. Bulaevskii, V.V. Kuzii, A.A. Sobyanin, Superconducting system with weak links and current in the ground state, Pis'ma Eksp. Theor. Fiz. 25 (1977) 314–318 (JETP lett. 25 (1977) 290).
[59] A.A. Abrikosov, L.P. Gor'kov, E. Dzyaloshinskii, Methods of Quantum Field Theory in Statistical Physics, Prentice-Hall, Englewood Cliffs, NJ, 1963.
[60] P.W. Anderson, Localized magnetic states and Fermi surface anomalies in tunneling, Phys. Rev. Lett. 17 (1966) 95–97.
[61] B.I. Spivak, S.A. Kivelson, Negative local superfluid densities: the difference between dirty superconductors and dirty Bose liquids, Phys. Rev. B 43 (1991) 3740–3743.
[62] B.L. Altshuler, D.E. Khmelnitzkii, B.Z. Spivak, Localization effects in normal metal and supercurrent through the S–N–S junction, Sol. State Commun. 48 (1983) 841–844.
[63] V.B. Geshkenbein, A.I. Larkin, Josephson effect in superconductors with heavy fermions, Pis'ma Zh. Ekps. Teor. Fiz. 43 (1986) 306–309 (JETP Lett. 43 (1986) 395–397).
[64] V.B. Geshkenbein, A.I. Larkin, A. Barone, Vortices with half magnetic flux quanta in heavy-fermion superconductors, Phys. Rev. B 36 (1997) 235–238.
[65] J. Bardeen, L.N. Cooper, J.R. Schrieffer, Theory of superconductivity, Phys. Rev. 108 (1957) 1175–1204.
[66] J.F. Annett, N.D. Goldenfeld, A.J. Leggett, in: D.M. Ginsberg (Ed.), Physical Properties of High-Temperature Superconductors V, World Scientific, Singapore, 1996, p. 571.

[67] R.A. Klemm, C.T. Rieck, K. Scharnberg, Order parameter symmetries in high-temperature superconductors, Phys. Rev. B 61 (2000) 5913–5916.
[68] D. Esteve, et al., Observation of the a.c. Josephson effect inside copper-oxide-based superconductors, Europhys. Lett. 3 (1987) 1237–1242.
[69] C.E. Gough, M.S. Colclough, E.M. Forgan, R.G. Jordan, M. Keene, C.M. Muirhead, A.I.M. Rae, N. Thomas, J.S. Abell, S. Sutton, Flux quantization in a high-T_c superconductor, Nature (London) 326 (1987) 855–857.
[70] H.F.C. Hoevers, P.J.M. van Bentum, L.E.C. van de Leemput, H. van Kempen, A.J.G. Schellingerhout, D. van der Marel, Determination of the energy gap in a thin $YBa_2Cu_3O_{7-x}$ film by Andreev reflection and by tunneling, Physica 152 (1988) 105–110.
[71] M. Takigawa, P.C. Hammel, R.H. Heffner, Z. Fisk, Spin susceptibility in superconducting $YBa_2Cu_3O_7$ from ^{63}Cu Knight shift, Phys. Rev. B 39 (1989) 7371–7374.
[72] S.E. Barrett, D.J. Durand, C.H. Pennington, C.P. Slichter, T.A. Friedman, J.P. Rice, D.M. Ginsberg, ^{63}Cu Knight shifts in the superconducting state of $YBa_2Cu_3O_{7-\delta}$ ($T_c = 90$ K), Phys. Rev. B 41 (1990) 6283–6296.
[73] L.D. Landau, E.M. Lifshitz, Statistical Physics, Pergamon, New York, 1979, Part I.
[74] M. Sigrist, T.M. Rice, Symmetry classification of states in high-T_c superconductors, Z. Phys. B: Condens. Matter 68 (1987) 9–14.
[75] J.F. Annett, N.D. Goldenfeld, S.R. Renn, in: D.M. Ginsberg (Ed.), Physical Properties of High-Temperature Superconductors II, World Scientific, Singapore, 1990, p. 571.
[76] J.F. Annett, Symmetry of the order parameter for high-temperature superconductivity, Adv. Phys. 39 (1991) 83–126.
[77] Q.P. Li, B.E. Koltenbah, R. Joynt, Mixed s-wave and d-wave superconductivity in high-T_c systems, Phys. Rev. B 48 (1993) 437–455.
[78] F. Wegner, S. Östlund, d-wave pairing in tetragonal superconductors, Phys. Rev. B 47 (1993) 5977–5983.
[79] S.S. Jha, A.K. Rajagopal, Intralayer and interlayer spin-singlet pairing and energy gap functions with different possible symmetries in high-T_c layered superconductors, Phys. Rev. B 55 (1997) 15248–15260.
[80] D.J. Van Harlingen, Phase-sensitive tests of the symmetry of the pairing state in the high-temperature superconductors—evidence for $d_{x^2-y^2}$ symmetry, Rev. Mod. Phys. 67 (1995) 515–535.
[81] S.K. Yip, A. Garg, Superconducting states of reduced symmetry: general order parameters and physical implications, Phys. Rev. B 48 (1993) 3304–3308.
[82] T. Schneider, J.M. Singer, Phase Transition Approach to High Temperature Superconductivity Universal Properties of Cuprate Superconductors, Imperial College Press, London, 2000.
[83] V.P. Mineev, K.V. Samokhin, Introduction to Unconventional Superconductivity, Gordon and Breach Scientific Publishers, Amsterdam, 1999.
[84] M. Sigrist, K. Ueda, Phenomenological theory of unconventional superconductivity, Rev. Mod. Phys. 63 (1991) 239–331.
[85] S.K. Yip, O.F. de Alcantara Bonfim, P. Kumar, Supercurrent tunneling between conventional and unconventional superconductors: a Ginzburg–Landau approach, Phys. Rev. B 41 (1990) 11214–11228.
[86] Z.X. Shen, D.S. Dessau, Phys. Rep. 253 (1995) 1.
[87] J. Leusueur, B. Leridon, M. Aprili, X. Grison, in: J. Bok, G. Deutscher (Eds.), The Gap Symmetry and Fluctuations in High Temperature Superconductors, Plenum, New York, 1998.
[88] T.P. Devereaux, D. Einzel, Electronic Raman scattering in superconductors as a probe of anisotropic electron pairing, Phys. Rev. B 51 (1995) 16336–16357.
[89] I.K. Yanson, Contact spectroscopy of high-temperature superconductors (review article) I. Physical and methodical fundamentals of contact spectroscopy of high-T_c superconductors, Experimental results for $La_{2-x}Sr_xCuO_4$ and their discussion, Fiz. Nizk. Temp. 17 (1991) 275–299.
[90] H. Monien, K. Scharnberg, L. Tewordt, D. Walker, Specific heat, thermal conductivity, ultrasound attenuation in d-wave superconductors, Solid State Commun. 61 (1987) 581–585.
[91] A. Chakraborty, A.J. Epstein, D.L. Cox, Specific heat of $Bi_2Sr_2CuO_6$, $Bi_2Sr_2CaCu_2O_8$ in the superconducting state, Phys. Rev. B 39 (1989) 12267–12270.
[92] M.E. Reeves, T.A. Friedmann, D.M. Ginsberg, Specific-heat measurements on two high-transition-temperature superconducting oxides: $La_{1.85}Ba_{0.15}CuO_4$, $La_{1.8}Sr_{0.2}CuO_4$, Phys. Rev. B 35 (1987) 7207–7209.

[93] Y.P. Feng, A. Jin, D. Finotello, K.A. Gillis, M.H.W. Chan, Low-temperature specific heat of $La_{1.85}Sr_{0.15}CuO_4$, La_2CuO_4, Phys. Rev. B 38 (1988) 7041–7044.
[94] S. von Molnar, A. Torressen, D. Kaiser, F. Holtzberg, T. Penney, Low-temperature specific heat of single-crystal $YBa_2Cu_3O_{7-\delta}$, Phys. Rev. B 37 (1988) 3762–3765.
[95] K.A. Moler, D.J. Baar, J.S. Urbach, R. Liang, W.N. Hardy, A. Kapitulnik, Magnetic field dependence of the density of states of $YBa_2Cu_3O_{6.95}$ as determined from the specific heat, Phys. Rev. Lett. 73 (1994) 2744–2747.
[96] K.A. Moler, D.L. Sisson, J.S. Urbach, M.R. Beasley, A. Kapitulnik, D.J. Baar, R. Liang, W.N. Hardy, Specific heat of $YBa_2Cu_3O_{7-\delta}$, Phys. Rev. B. 55 (1997) 3954–3965.
[97] D.A. Wright, J.P. Emerson, B.F. Woodfield, J.E. Gordon, R.A. Fisher, N.E. Phillips, Low-temperature specific heat of $YBa_2Cu_3O_{7-\delta}$, $0 \leqslant \delta \leqslant 0.2$: evidence for d-wave pairing, Phys. Rev. Lett. 82 (1999) 1550–1553.
[98] G.E. Volovik, Superconductivity with lines of gap nodes: density of states in the vortex, Pis'ma Eksp. Theor. Fiz. 58 (1993) 457–461 (JETP Lett. 58 (1993) 469).
[99] M.E. Reeves, S.E. Stupp, T.A. Friedmann, F. Slakey, D.M. Ginsberg, M.V. Klein, Field-dependent specific heat of polycrystalline $YBa_2Cu_3O_{7-x}$, Phys. Rev. 40 (1989) 4573–4584.
[100] B. Revaz, J.-Y. Genoud, A. Junod, K. Neumaier, A. Erb, E. Walker, d-wave scaling relations in the mixed-state specific heat of $YBa_2Cu_3O_7$, Phys. Rev. Lett. 80 (1998) 3364–3367.
[101] G.E. Volovik, Fermionic entropy of the vortex state in d-wave superconductors, Pis'ma Eksp. Theor. Fiz. 65 (1997) 465–469 (JETP Lett. 65 (1997) 491).
[102] S.H. Simon, P.A. Lee, Scaling of the quasiparticle spectrum for d-wave superconductors, Phys. Rev. Lett. 78 (1997) 1548–1551.
[103] J.F. Annett, N. Goldenfeld, S.R. Renn, Interpretation of the temperature dependence of the electromagnetic penetration depth in $YBa_2Cu_3O_{7-\delta}$, Phys. Rev. B 43 (1991) 2778–2782.
[104] D.J. Scalapino, The case for $d_{x^2-y^2}$ pairing IBN the cuprate superconductors, Phys. Rep. 250 (1995) 329–365.
[105] W.N. Hardy, D.A. Bonn, D.C. Morgan, Ruixing Liang, Kuan Zhang, Precision measurements of the temperature dependence of λ in $YBa_2Cu_3O_{6.95}$: strong evidence for nodes in the gap function, Phys. Rev. Lett. 70 (1993) 3999–4002.
[106] Z. Ma, R.C. Taber, L.W. Lombardo, A. Kapitulnik, M.R. Beasley, P. Merchant, C.B. Eom, S.Y. Hou, J.M. Phillips, Microwave penetration depth measurements on $Bi_2Sr_2CaCu_2O_8$ single crystals and $YBa_2Cu_3O_{7-\delta}$ thin films, Phys. Rev. Lett. 71 (1993) 781–784.
[107] J.Y. Lee, K.M. Paget, T.R. Lemberger S.R. Foltyn, X. Wu, Crossover in temperature dependence of penetration depth $\lambda(T)$ in superconducting $YBa_2Cu_3O_{7-\delta}$ films, Phys. Rev. B 50 (1994) 3337–3341.
[108] D.A. Bonn, S. Kamal, K. Zhang, R. Liang, D.J. Baar, E. Klein, W.N. Hardy, Comparison of the influence of Ni and Zn impurities on the electromagnetic properties of $YBa_2Cu_3O_{6.95}$, Phys. Rev. B 50 (1994) 4051–4063.
[109] H. Walter, W. Prusseit, R. Semerad, H. Kinder, W. Assmann, H. Huber, H. Burkhardt, D. Rainer, J.A. Sauls, Low-temperature anomaly in the penetration depth of $YBa_2Cu_3O_7$ films: evidence for andreev bound states at surfaces, Phys. Rev. Lett. 80 (1998) 3598–3601.
[110] S. Kamal, R. Liang, A. Hosseini, D.A. Bonn, W.N. Hardy, Magnetic penetration depth and surface resistance in ultra high-purity $YBa_2Cu_3O_{7-\delta}$ crystal, Phys. Rev. B 58 (1998) R8933–R8936.
[111] K. Karpinska, M.Z. Cieplak, S. Guha, A. Malinowski, T. Skoskiewicz, W. Plesiewicz, M. Berkowski, B. Broyce, T.R. Lemberger, P. Lindenfeld, Metallic nonsuperconducting phase, d-wave superconductivity in Zn-substituted $La_{1.85}Sr_{0.15}CuO_4$, Phys. Rev. Lett. 84 (2000) 155–158.
[112] W.A. Atkinson, J.P. Carbotte, Penetration-depth calculations in the ab, c directions in a layered S/N superconductor, Phys. Rev. B 51 (1995) 16371–16379.
[113] R.A. Klemm, S.H. Liu, Role of normal layers in penetration depth determinations of the pairing state in high-T_c superconductors, Phys. Rev. Lett. 74 (1995) 2343–2346.
[114] M.J. Graf, S.K. Yip, J.A. Sauls, Electronic thermal conductivity and the Wiedemann-Franz law for unconventional superconductors, Phys. Rev. B 53 (1996) 14161–15147.
[115] A.C. Durst, P.A. Lee, Impurity-induced quasiparticle transport and universal-limit Wiedemann-Franz violation in d-wave superconductors, Phys. Rev. B 62 (2000) 1270–1290.
[116] M. Houssa, M. Ausloos, Comment on Electronic thermal conductivity and the Wiedemann-Franz law for unconventional superconductors, Phys. Rev. B 56 (1997) 953–954.

[117] C. Uher, in: D. Ginsberg (Ed.), Physical Properties of High Temperature superconductors, Vol. III, World Scientific, Singapore, 1992, p. 159.
[118] Z. Gold, R. Gagnon, B. Ellman, L. Taillefer, K. Behnia, Anisotropic thermal conductivity of $YBa_2Cu_3O_{7-x}$, Physica C 235–240 (1994) 1485–1486.
[119] L. Taillefer, B. Lussier, R. Gagnon, K. Behnia, H. Aubin, Universal heat conduction in $YBa_2Cu_3O_{6.9}$, Phys. Rev. Lett. 79 (1997) 483–486.
[120] R. Movshovich, M.A. Hubbard, M.B. Salamon, A.V. Balatsky, R. Yoshizaki, J.L. Sarrao, M. Jaime, Low-Temperature anomaly in thermal conductivity of $Bi_2Sr_2Ca(Cu_{1-x}Ni_x)_2O_8$: second superconducting phase? Phys. Rev. Lett. 80 (1998) 1968–1971.
[121] M. Chiao, R.W. Hill, C. Lupien, L. Taillefe, P. Lambert, R. Gagnon, P. Fournier, Low-energy quasiparticles in cuprate superconductors: a quantitative analysis, Phys. Rev. B 62 (2000) 3554–3558.
[122] I. Vekhter, E.J. Nicol, J.P. Carbotte, Ultrasonic attenuation in clean d-wave superconductors, Phys. Rev. B 59 (1999) 7123–7126.
[123] S. Bhattacharya, M.J. Higgins, D.C. Johnston, A.J. Jacobson, J.P. Stokes, J.T. Lewandowski, D.P. Goshorn, Anomalous ultrasound propagation in the high-T_c superconductors: $La_{1.8}Sr_{0.2}CuO_{4-y}$ and $YBa_2Cu_3O_{7-\delta}$, Phys. Rev. B 37 (1988) 5901–5904.
[124] M.-F. Xu, H.-P. Baum, A. Schenstrom, B.K. Sarma, M. Levy, K.J. Sun, L.E. Toth, S.A. Wolf, D.U. Gubser, Ultrasonic-attenuation measurements in single-phased $YBa_2Cu_3O_7$, Phys. Rev. B 37 (1988) 3675–3677.
[125] N. Bulut, D.J. Scalapino, Analysis of NMR data in the superconducting state of $YBa_2Cu_3O_7$, Phys. Rev. Lett. 68 (1992) 706–709.
[126] A.M. Gabovich, A.I. Voitenko, Influence of order-parameter nonhomogeneities on low-temperature properties of superconductors, Phys. Rev. B 60 (1999) 7465–7472.
[127] A.M. Gabovich, A.I. Voitenko, M.S. Li, M. Pekala, H. Szymczak, Heat capacity of mesoscopically disordered superconductors with emphasis on MgB_2, J. Phys.: Condens. Matter 14 (2002) 9621–9629.
[128] D.A. Wollman, D.J. Van Harlingen, W.C. Lee, D.M. Ginsberg, A.J. Leggett, Experimental determination of the superconducting pairing state in YBCO from the phase coherence of YBCO-Pb dc SQUIDs, Phys. Rev. Lett. 71 (1993) 2134–2137.
[129] C.C. Tsuei, J.R. Kirtley, C.C. Chi, L.S. Yu-Jahnes, A. Gupta, T. Shaw, J.Z. Sun, M.B. Ketchen, Pairing symmetry and flux quantization in a tricrystal superconducting ring of $YBa_2Cu_3O_{7-\delta}$, Phys. Rev. Lett. 73 (1994) 593–596.
[130] A. Mathai, Y. Gim, R.C. Black, A. Amar, F.C. Wellstood, Experimental proof of a time-reversal-invariant order parameter with a π shift in $YBa_2Cu_3O_{7-\delta}$, Phys. Rev. Lett. 74 (1995) 4523–4526.
[131] D.A. Brawner, H.R. Ott, Evidence for an unconventional superconducting order parameter in $YBa_2Cu_3O_{0.69}$, Phys. Rev. B 50 (1994) 6530–6533.
[132] R.A. Klemm, Comment on experimental determination of the superconducting pairing state in YBCO from the phase coherence of YBCO-Pb dc SQUIDs, Phys. Rev. Lett. 73 (1994) 1871.
[133] D.A. Wollman, D.J. Van Harlingen, A.J. Leggett, Wollmann et al. reply, Phys. Rev. Lett. 73 (1994) 1872.
[134] J.R. Kirtley, K.A. Moller, G. Villard, A. Maignan, c-Axis penetration depth of Hg-1201 single crystals, Phys. Rev. Lett. 81 (1998) 2140–2143.
[135] K.A. Moller, J.R. Kirtley, D.G. Hinks, T.W. Li, M. Xu, Images of interlayer Josephson vortices in $Tl_2Ba_2CuO_{6+\delta}$, Science 279 (1998) 1193–1196.
[136] R.R. Schulz, B. Chesca, B. Goetz, C.W. Schneider, A. Schmehl, H. Bielefeldt, H. Hilgenkamp, J. Mannhart, Design and realization of an all d-wave, dc π-superconducting quantum interference device, Appl. Phys. Lett. 76 (2000) 912–914.
[137] D.A. Wollmann, D.J. Van Harlingen, J. Giapintzakis, D.M. Ginsberg, Evidence for $d_{x^2-y^2}$ pairing from the magnetic field modulation of $YBa_2Cu_3O_7$-Pb Josephson junctions, Phys. Rev. Lett. 74 (1995) 797–800.
[138] K.K. Likharev, Introduction to Dynamics of Josephson Junctions, Nauka, Moscow, 1985 (in Russian).
[139] I. Iguchi, Z. Wen, Experimental evidence for a d-wave pairing state in $YBa_2Cu_3O_{7-y}$ from a study of $YBa_2Cu_3O_{7-y}$/insulator/Pb Josephson tunnel junctions, Phys. Rev. B 49 (1994) 12388–12391.
[140] J.H. Miller Jr., Q.Y. Ying, Z.G. Zou, N.Q. Fan, J.H. Xu, M.F. Davis, J.C. Wolfe, Use of tricrystal junctions to probe the pairing state symmetry of $YBa_2Cu_3O_{7-\delta}$, Phys. Rev. Lett. 74 (1995) 2347–2350.
[141] D.A. Brawner, H.R. Ott, Evidence for a non-s-wave superconducting order parameter in $YBa_2Cu_3O_{6.6}$, Phys. Rev. B 53 (1996) 8249–8252.

[142] C. Nappi, R. Cristiano, M.P. Lisitskii, Fiske steps in annular Josephson junctions with trapped flux quanta, Phys. Rev. B 58 (1998) 11685–11691.
[143] J.R. Kirtley, K.A. Moler, D.J. Scalapino, Spontaneous flux, magnetic-interference patterns 0–π Josephson junctions, Phys. Rev. B 56 (1997) 886–891.
[144] K. Binder, A.P. Young, Spin glasses: experimental facts, theoretical concepts, open questions, Rev. Mod. Phys. 58 (1986) 801–976.
[145] H. Kawamura, M.S. Li, Monte Carlo studies of the ordering of ceramic superconductors: chiral glass, orbital-glass and nonlinear susceptibilities, Phys. Rev. B 54 (1996) 619–636.
[146] R. Sasik, L.N. Bulaevskii, A.R. Bishop, M.P. Maley, Vortices and plasmons in inductive periodic Josephson-junction arrays, Phys. Rev. B 55 (1997) 11688–11692.
[147] M. Sigrist, D.B. Bailey, R.B. Laughlin, Fractional vortices as evidence of time-reversal symmetry breaking in high-temperature superconductors, Phys. Rev. Lett. 74 (1995) 3249–3252.
[148] C. Dasgupta, B.I. Halperin, Phase transition in a lattice model of superconductivity, Phys. Rev. Lett. 47 (1981) 1556–1560.
[149] A.P. Malozemoff, L. Krusin-Elbaum, D.C. Cronemeyer, Y. Yeshrun, F. Holtzberg, Remanent moment of high-temperature superconductors: Implications for flux-pinning and glassy models, Phys. Rev. B 38 (1988) 6490–6499.
[150] M. Kawachi, M. Hagiwara, K. Koyama, M. Matsuura, Successive phase transitions of a hierarchical nature in a $YBa_2Cu_4O_8$, J. Phys. Soc. Japan 63 (1994) 3405–3411.
[151] C. Auletta, R. de Luca, S. Pace, G. Raiconi, Numerical simulation of magnetic-flux penetration in concentric circular arrays of Josephson junctions, Phys. Rev. B 47 (1993) 14326–14333.
[152] C. Auletta, G. Raiconi, R. de Luca, S. Pace, Positive field-cooled dc susceptibility in granular superconductors interpreted through numerical simulations on a simple Josephson-junction array model, Phys. Rev. B 51 (1995) 12844–12847.
[153] M. Chandran, Positive moment of an inductively coupled Josephson junction array, Phys. Rev. B 56 (1997) 6169–6174.
[154] A.P. Nielsen, A.B. Cawthorne, P. Barbara, F.C. Wellstood, C.J. Lobb, R.S. Newrock, M.G. Forreste, Paramagnetic Meissner effect in multiply-connected superconductors, Phys. Rev. B 62 (2000) 14380–14383.
[155] C. De Leo, G. Rotoli, P. Barbara, A.P. Nielsen, C.J. Lobb, Mutual-inductance route to the paramagnetic Meissner effect in two-dimensional Josephson-junction arrays, Phys. Rev. B 64 (2001) 144518-1–144518-5.
[156] Y. He, C.M. Muirhead, W.F. Vinen, Paramagnetic Meissner effect in high-temperature superconductors: experiments and interpretation, Phys. Rev. B 53 (1996) 12441–12453.
[157] I.A. Chaban, Paramagnetic Meissner effect, J. Supercond. 13 (2000) 1011–1017.
[158] P. Tokmakova, I.A. Chaban, Phase diagram and peculiarities of the sound propagation in $YBa_2Cu_3O_x$ superconductivity, Phys. Chem. Tech. 3 (1990) 2567–2580 (in Russian).
[159] J.M. Kosterlitz, D.J. Thouless, Ordering, metastability and phase transitions in two-dimensional systems, J. Phys. C: Solid State Phys. 6 (1973) 1181–1203.
[160] C.P. Bean, Magnetization of hard superconductors, Phys. Rev. Lett. 8 (1962) 250–253.
[161] R.P. Huebener, F. Kober, R. Gross, H.-C. Ri, Thermoelectric and thermomagnetic effects in the mixed state of HTS's, Physica C 185-189 (1991) 349–354.
[162] L.D. Landau, E.M. Lifshitz, Theoretical Physics, Vol. 8, Electrodynamics of Continuous Media, Nauka, Moscow, 1982 (in Russian).
[163] P.N. Mikheenko, Yu.E. Kuzovlev, Inductance measurements of HTSC films with high critical currents, Physica C 204 (1993) 229–236.
[164] M. Abramowitz, I.A. Stegun (Eds.), Handbook of Mathematical Functions, Natl. Bur. Stand. Appl. Math. Ser. No 55, U.S. GPO, Washington, DC, 1965.
[165] V.L. Ginzburg, L.D. Landau, Theory of superconductivity, Zh. Eksp. Teor. Fiz. 20 (1950) 1064–1082.
[166] G.F. Zharkov, Paramagnetic Meissner effect in superconductors from self-consistent solution of Ginzburg–Landau equations, Phys. Rev. B 63 (2001) 214502-1–214502-6.
[167] P.G. de Gennes, Superconductivity of Metals and Alloys, Addison-Wesley, New York, 1966.
[168] R.B. Dingle, Some magnetic properties of metals, I. General introduction and properties of large systems of electrons, Proc. R. Soc. London, Ser. A 212 (1952) 47–65.

[169] R.B. Dingle, Some magnetic properties of metals, IV. Properties of small systems of electrons, Proc. R. Soc. London, Ser. A 211 (1952) 500–516.
[170] O. Buisson, P. Gandit, R. Rammal, Y.Y. Wang, B. Pannetier, Magnetization oscillation of a superconducting disk, Phys. Lett. A 150 (1990) 36–42.
[171] V.V. Moshchalkov, L. Geilen, C. Strunk, R. Jonckheere, X. Qui, C. Van Haesendonck, Y. Bruynseraede, Effect of sample topology on the critical fields of mesoscopic superconductors, Nature 373 (1995) 319–322.
[172] D. Saint-James, P.G. de Gennes, Onset of superconductivity in decreasing fields, Phys. Lett. A 7 (1963) 306–309.
[173] F. de la Cruz, H.J. Fink, J. Luzuriaga, Temperature dependence of the superconducting giant-vortex state, Theory and experiment, Phys. Rev. B 20 (1979) 1947–1959.
[174] A.A. Abrikosov, Fundamentals of the Theory of Metals, North-Holland, Amsterdam, 1988.
[175] H.J. Fink, A.G. Presson, Magnetic irreversible solution of the Ginzburg–Landau equations, Phys. Rev. 151 (1966) 219–228.
[176] V.A. Schweigert, F.M. Peeters, Paramagnetic Meissner effect in mesoscopic samples, cond-mat/0001110.
[177] H. Kawamura, M.S. Li, Chiral glass: a new equilibrium phase of ceramic high-T_c superconductors, J. Phys. Soc. Japan 66 (1997) 2110–2122.
[178] H. Kawamura, Universality of phase transitions of frustrated antiferromagnets, J. Phys.: Condens Matter 10 (1998) 4707–4754.
[179] H. Kawamura, Spin and chirality orderings of frustrated magnets—stacked-triangular antiferromagnets, spin glasses, Can. J. Phys. 79 (2001) 1447–1458.
[180] H. Kawamura, Classical and quantum chiral order in frustrated XY magnets, Cond-Mat/0202109.
[181] V. Kalmeyer, R.B. Laughlin, Equivalence of the resonating-valence-bond, fractional quantum Hall states, Phys. Rev. Lett. 59 (1987) 2093–2096.
[182] X.G. Wen, Frank Wilczek, A. Zee, Chiral spin states and superconductivity, Phys. Rev. B 39 (1989) 11413–11423.
[183] P.A. Lee, N. Nagaosa, Gauge theory of the normal state of high-T_c superconductors, Phys. Rev. B 46 (1992) 5621–5639.
[184] S. Deser, R. Jackiw, S. Templeton, Three-dimensional massive gauge theories, Phys. Rev. Lett. 48 (1982) 975–978.
[185] H.B. Nielson, M. Ninomiya, The Adler-Bell-Jackiw anomaly and Weyl fermions in a crystal, Phys. Lett. B 130 (1983) 389–396.
[186] R.B. Laughlin, Superconducting ground state of noninteracting particles obeying fractional statistics, Phys. Rev. Lett. 60 (1988) 2677–2680.
[187] F.D.M. Haldane, Model for a Quantum hall effect without landau levels: condensed-matter realization of the parity anomaly, Phys. Rev. Lett. 61 (1988) 2015–2018.
[188] D.A. Huse, H.S. Seung, Possible vortex-glass transition in a model random superconductor, Phys. Rev. B 42 (1990) 1059–1061.
[189] M.J.P. Gingras, Numerical study of vortex-glass order in random-superconductor, related spin-glass models, Phys. Rev. B 45 (1992) 7547–7550.
[190] M. Cieplak, J.R. Banavar, M.S. Li, A. Khurana, Frustration, scaling, local gauge invariance, Phys. Rev. B 45 (1992) 786–792.
[191] S.F. Edwards, P.W. Anderson, Theory of spin glasses, J. Phys. F 5 (1975) 965–974.
[192] F. Guerra, About the overlap distribution in mean field spin glass models, Int. J. Mod. Phys. B 10 (1996) 1675–1684.
[193] E. Marinari, C. Naitza, F. Zuliani, M. Picco, F. Ritort, General method to determine replica symmetry breaking transitions, Phys. Rev. Lett. 81 (1998) 1698–1701.
[194] H.S. Bokil, A.J. Bray, Barbara Drossel, M.A. Moore, Comment on general method to Determine replica symmetry breaking transitions, Phys. Rev. Lett. 82 (1999) 5174–5174;
E. Marinari, C. Naitza, F. Zuliani, G. Parisi, M. Picco, F. Ritort, Marinari et al. Reply, Phys. Rev. Lett. 82 (1999) 5175–5175.
[195] M.N. Barber, in: C. Domb, J.L. Lebowitz (Eds.), Phase Transitions, Critical Phenomena, Vol. 8, Academic, New York/London, 1983 (Chapter 2).
[196] H. Kawamura, Numerical studies of chiral ordering in three-dimensional XY spin glasses, Phys. Rev. B 51 (1995) 12398–12409.

[197] H. Kawamura, M.S. Li, Nature of the ordering in the three-dimensional XY spin glass, Phys. Rev. Lett. 87 (2001) 187204-1–187204-4.
[198] K. Hukushima, H. Kawamura, Chiral glass transition and replica symmetry breaking of a three-dimensional Heisenberg spin glass, Phys. Rev. E 61 (2000) R1008–R1011.
[199] S.E. Korshunov, Replica symmetry breaking in vortex glasses, Phys. Rev. B 48 (1993) 3969–3975.
[200] G. Parisi, Off-equilibrium fluctuation–dissipation relation in fragile glasses, Phys. Rev. Lett. 79 (1997) 3660–3663.
[201] H.S. Bokil, A.P. Young, Absence of a phase transition in a three-dimensional vortex glass model, Phys. Rev. Lett. 74 (1995) 3021–3024.
[202] C. Wengel, A.P. Young, Monte Carlo study of a three-dimensional vortex-glass model with screening, Phys. Rev. B 54 (1996) R6869–R6872.
[203] K. Hukushima, K. Nemoto, Exchange Monte Carlo method and application to spin glass simulations, J. Phys. Soc. Japan 65 (1996) 1604–1608.
[204] E. Marinari, G. Parisi, Simulated tempering: a new Monte Carlo scheme, Europhys. Lett. 19 (1992) 451–458.
[205] A.P. Luybartsev, A.A. Martsinovski, S.V. Shevkanov, P.N. Vorontsov-Velyaminov, New approach to Monte Carlo calculation of the free energy: method of expanded ensembles, J. Chem. Phys. 96 (1992) 1776–1783.
[206] N. Kawashima, A.P. Young, Phase transition in the three-dimensional $\pm J$ Ising spin glass, Phys. B. 53 (1996) R484–487.
[207] M. Palassini, S. Caracciolo, Universal finite-size scaling functions in the 3D Ising spin glass, Phys. Rev. Lett. 82 (1999) 5128–5131.
[208] E. Marinari, Giorgio Parisi, Juan J. Ruiz-Lorenzo, Phase structure of the three-dimensional Edwards–Anderson spin glass, Phys. Rev. B 58 (1998) 14852–14863.
[209] U.C. Täuber, D.R. Nelson, Superfluid bosons, flux liquids: disorder, thermal fluctuations, and finite-size effects, Phys. Rep. 289 (1997) 159–233.
[210] T. Giamarchi, P. Le Doussal, Elastic theory of pinned flux lattices, Phys. Rev. Lett. 72 (1994) 1530–1533.
[211] T. Giamarchi, P. Le Doussal, Elastic theory of flux lattices in the presence of weak disorder, Phys. Rev. B 52 (1995) 1242–1270.
[212] T. Giamarchi, P. Le Doussal, Phase diagrams of flux lattices with disorder, Phys. Rev. B 5 (1997) 6577–6583.
[213] M.P.A. Fisher, Vortex-glass superconductivity: a possible new phase in bulk high-T_c oxides, Phys. Rev. Lett. 62 (1989) 1415–1418.
[214] J.C. Le Guillou, J. Zinn-Justin, Critical exponents from field theory, Phys. Rev. B 21 (1980) 3976–3998.
[215] J.A. Lipa, D.R. Swanson, J.A. Nissen, T.C.P. Chui, U.E. Israelsson, Heat capacity and thermal relaxation of bulk helium very near the lambda point, Phys. Rev. Lett. 76 (1996) 944–947.
[216] A.B. Harris, Effect of random defects on the critical behavior of ising models, J. Phys. C 7 (1974) 1671–1692.
[217] T. Nattermann, S. Scheidl, Vortex-glass phases in type-II superconductors, Adv. Phys. 49 (2000) 607–704.
[218] J. Kierfeld, V. M. Vinokur, Dislocations, the critical endpoint of the melting line of vortex line lattices, Phys. Rev. B 61 (2000) R14928–R14931.
[219] B. Khaykovich, M. Konczykowski, E. Zeldov, R.A. Doyle, D. Majer, P.H. Kes, T.W. Li, Vortex-matter phase transitions in $Bi_2Sr_2CaCu_2O_8$: effects of weak disorder, Phys. Rev. B 56 (1997) R517–R520.
[220] A.I. Larkin, Effect of inhomogeneities on the structure of the mixed state of superconductors, Sov. Phys. JETP 31 (1970) 784–786.
[221] D.S. Fisher, M.P.A. Fisher, D.A. Huse, Thermal fluctuations, quenched disorder, phase transitions and transport in type-II superconductors, Phys. Rev. B 43 (1991) 130–159.
[222] T. Nattermann, Scaling approach to pinning: charge density waves, giant flux creep in superconductors, Phys. Rev. Lett. 64 (1990) 2454–2457.
[223] D. Carpentier, P. Le Doussal, T. Giamarchi, Stability of the Bragg glass phase in a layered geometry, Europhys. Lett. 35 (1996) 379–384.
[224] J. Kierfeld, T. Nattermann, T. Hwa, Topological order in the vortex-glass phase of high-temperature superconductors, Phys. Rev. B 55 (1997) 626–629.
[225] D.S. Fisher, Stability of elastic glass phases in random field XY magnets, vortex lattices type-II superconductors, Phys. Rev. Lett. 78 (1997) 1964–1967.
[226] M.J.P. Gingras, D.A. Huse, Topological defects in the random-field XY model and the pinned vortex lattice to vortex glass transition in type-II superconductors, Phys. Rev. B 53 (1996) 15193–15200.

[227] A. van Otterlo, R.T. Scalettar, G.T. Zimanyi, Phase diagram of disordered vortices from London Langevin simulations, Phys. Rev. Lett. 81 (1998) 1497–1500.
[228] T. Klein, J. Joumard, S. Blanchard, J. Marcus, R. Cubitt, T. Giamarchi, P. le Doussal, A Bragg glass phase in the vortex lattice of a type II superconductor, Nature 413 (2001) 404–406.
[229] R.H. Koch, V. Foglietti, W.J. Gallagher, G. Koren, A. Gupta, M.P.A. Fisher, Experimental evidence for vortex-glass superconductivity in Y–Ba–Cu–O, Phys. Rev. Lett. 63 (1989) 1511–1514.
[230] P.L. Gammel, L.F. Schneemeyer, D.J. Bishop, SQUID picovoltometry of $YBa_2Cu_3O_7$ single crystals: evidence for a finite-temperature phase transition in the high-field vortex state, Phys. Rev. Lett. 66 (1991) 953–956.
[231] K. Deligiannis, P.A.J. de Groot, M. Oussena, S. Pinfold, R. Langan, R. Gagnon, L. Taillefer, New features in the vortex phase diagram of $YBa_2Cu_3O_{7-\delta}$, Phys. Rev. Lett. 79 (1997) 2121–2124.
[232] H. Safar, P.L. Gammel, D.A. Huse, G.B. Alers, D.J. Bishop, W.C. Lee, J. Giapintzakis, D.M. Ginsberg, Vortex dynamics below the flux-lattice melting transition in $YBa_2Cu_3O_{7-\delta}$, Phys. Rev. B 52 (1995) 6211–6214.
[233] G.I. Menon, Phase behavior of type-II superconductors with quenched point pinning disorder: A phenomenological proposal, Phys. Rev. B 65 (2002) 104527-1–104527-23.
[234] T.K. Worthington, M.P.A. Fisher, D.A. Huse, Observation of separate vortex-melting and vortex-glass transitions in defect-enhanced $YBa_2Cu_3O_7$ single crystals, Phys. Rev. B 46 (1992) 11854–11861.
[235] Y. Nonomura, X. Hu, Effects of point defects on the phase diagram of vortex states in high-T_c superconductors in the $B||c$ axis, Phys. Rev. Lett. 86 (2001) 5140–5143.
[236] P. Olsson, S. Teitel, Disorder driven melting of the vortex line lattice, Phys. Rev. Lett. 87 (01) 137001-1–137001-4.
[237] T. Nishizaki, K. Shibata, T. Sasaki, N. Kobayashi, New equilibrium phase diagram of $YBa_2Cu_3O_y$ under high magnetic fields, Physica C 341–348 (2000) 957–960.
[238] H.H. Wen, S.L. Li, G.H. Chen, X.S. Ling, Vortex-slush state in $YBa_2Cu_3O_7$-thin films, Phys. Rev. B 64 (2001) 054507-1–054507-5.
[239] R. Ikeda, Effects of line disorder on the vortex glass transition induced by the point disorder, J. Phys. Soc. Jpn. 70 (2001) 219–227.
[240] C. Ebner, D. Stroud, Diamagnetic susceptibility of superconducting clusters: spin-glass behavior, Phys. Rev. B 31 (1995) 165–171.
[241] S. John, T.C. Lubensky, Phase transitions in a disordered granular superconductor near percolation, Phys. Rev. B 34 (1986) 4815–4825.
[242] M.P.A. Fisher, T.A. Tokuyasu, A.P. Young, Vortex variable-range-hopping resistivity in superconducting films, Phys. Rev. Lett. 66 (1991) 2931–2934.
[243] J.D. Reger, T.A. Tokuyasu, A.P. Young, Vortex-glass transition in three dimensions, Phys. Rev. B 44 (1991) 7147–7150.
[244] R.A. Hyman, M. Wallin, M.P.A. Fisher, S.M. Girvin, A.P. Young, Current-voltage characteristics of two-dimensional vortex-glass models, Phys. Rev. B 51 (1995) 15304–15311.
[245] J.M. Kosterlitz, N. Akino, Numerical study of order in a gauge glass model, Phys. Rev. Lett. 81 (1998) 4672–4675.
[246] J. Maucourt, D.R. Grempel, Scaling of domain-wall energies in the three-dimensional gauge glass model, Phys. Rev. B 58 (1998) 2654–2657.
[247] T. Olson, A.P. Young, Finite temperature ordering in the three-dimensional gauge glass, Phys. Rev. B 61 (2000) 12467–12473.
[248] G. Blatter, M.V. Feigelman, V.B. Geshkenbein, A.I. Larkin, V.M. Vinokur, Vortices in high-temperature superconductors, Rev. Mod. Phys. 64 (1994) 1125–1388.
[249] G.I. Menon, C. Dasgupta, Effects of pinning disorder on the correlations, freezing of the flux liquid in layered superconductors, Phys. Rev. Lett. 73 (1994) 1023–1026.
[250] J. Kisker, H. Rieger, Application of a minimum-cost flow algorithm to the three-dimensional gauge-glass model with screening, Phys. Rev. B 58 (1998) R8873–R8876.
[251] H. Kawamura, Simulation studies on the stability of the vortex-glass order, J. Phys. Soc. Jpn. 69 (2000) 29–32.
[252] F.O. Pfeiffer, H. Rieger, Numerical study of the strongly screened vortex-glass model in an external field, Phys. Rev. B 60 (1999) 6304–6307.
[253] J. Magnusson, J.-O. Andersson, M. Björnander, P. Nordblad, P. Svedlindh, Time dependence of the paramagnetic Meissner effect: comparison between model calculations, experiments, Phys. Rev. B 51 (1995) 12776–12781.

[254] J. Magnusson, M. Björnander, L. Pust, P. Svedlindh, P. Nordblad, T. Lundström, Time dependence of the magnetization of $Bi_2Sr_2CaCu_2O_8$ displaying the paramagnetic Meissner effect, Phys. Rev. B 52 (1995) 7675–7681.
[255] H. Deguchi, K. Koyama, M. Yasunaka, S. Takagi, N. Nagano, K. Mizuno, Pressure dependence of the chiral glass transition in Y–Ba–Cu–O superconductors, J. Phys. Chem. Solids 63 (2002) 1081–1083.
[256] H. Kawamura, Dynamical properties of chiral glass order in ceramic high-T_c superconductors, J. Phys. Soc. Jpn. 69 (Suppl. A) (2000) 281–286.
[257] L. Leylekian, M. Ocio, J. Hammann, Thermodynamic flux fluctuations in the granular superconductor $La_{1.8}Sr_{0.2}CuO_4$, Physica C 185–189 (1991) 2243–2244.
[258] L. Leylekian, M. Ocio, J. Hammann, Gauge glass properties in a granular $La_{1.8}Sr_{0.2}CuO_4$ superconductor, Physica B 194-196 (1994) 1865–1866.
[259] C.P. Bean, Magnetization of high-field superconductors, Rev. Mod. Phys. 36 (1964) 31–38.
[260] H. Deguchi, M. Yanusaka, R. Oniki, S. Takagi, K. Koyama, K. Mizuno, Dynamical scaling analysis of susceptibility in ceramic YBCO superconductors, submitted to LT23 Proceedings.
[261] J. Magnusson, E. Papadopoulou, P. Svedlindh, P. Nordblad, AC susceptibility of a paramagnetic Meissner effect sample, Physica C 297 (1998) 317–325.
[262] E.L. Papadopoulou, P.P. Svedlindh, P. Nordblad, Flux dynamics of a superconductor showing a glassy paramagnetic Meissner state, Phys. Rev. B. 65 (2002) 144524-1–144524-6.
[263] J. Magnusson, P. Svedlindh, P. Nordblad, Flux noise in $Bi_2Sr_2CaCu_2O_8$ displaying the paramagnetic Meissner effect: evidence of spontaneous magnetic moments, Phys. Rev. B 57 (1998) 10929–10935.
[264] P. Nordblad, P. Svedlindh, in: A.P. Young (Ed.), Spin Glasses and Random Fields, Singapore, World Scientific, p. 1.
[265] L. Ji, R.H. Sohn, G.C. Spalding, C.J. Lobb, M. Tinkham, Critical-state model for harmonic generation in high-temperature superconductors, Phys. Rev. B 40 (1989) 10936–10945.
[266] T. Ishida, R.B. Goldfarb, Fundamental, harmonic susceptibilities of $YBa_2Cu_3O_{7-\delta}$, Phys. Rev. B 41 (1990) 8937–8948.
[267] T. Wolf, A. Majhofer, ac susceptibilities of a network of resistively shunted Josephson junctions with self-inductances, Phys. Rev. B 47 (1993) 5383–5389.
[268] A. Majhofer, T. Wolf, W. Dieterich, Irreversible magnetization effects in a network of resistively shunted tunnel junctions, Phys. Rev. B 44 (1991) 9634–9638.
[269] M.S. Li, Second harmonics and compensation effect in ceramic superconductors, Phys. Rev. B 60 (1999) 118–121.
[270] L. Lundgren, P. Svedlindh, P. Nordblad, O. Beckman, Dynamics of the relaxation-time spectrum in a CuMn spin-glass, Phys. Rev. Lett. 51 (1983) 911–914.
[271] J.-P. Bouchaud, L.F. Cugliandolo, J. Kurchan, M. Mezard, in: A.P. Young (Ed.), Spin Glasses, Random Fields, Singapore, World Scientific, p. 161.
[272] E.L. Papadopoulou, P. Nordblad, Aging, rejuvenation and memory phenomena in a Bi-2212 superconductor showing the paramagnetic Meissner effect, Eur. Phys. J. B 22 (2001) 187–191.
[273] H. Rieger, Monte Carlo studies of Ising spin glasses and random field systems, in: D. Stauffer (Ed.), Annual Reviews of Computational Physics II, World Scientific, Singapore, 1995, p. 295.
[274] M.S. Li, P. Nordblad, H. Kawamura, Aging effect in ceramic superconductors, Phys. Rev. Lett. 86 (2001) 1339–1342.
[275] M.S. Li, Microwave absorption in s- and d-wave disordered superconductors, Phys. Rev. B 64 (2001) 144501–144506.
[276] J. Stankowski, J. Martinek, B. Czyzak, Thermal detection of microwave absorption in high-temperature superconductors, Phys. Rev. B 36 (1987) 7126–27128.
[277] R. Durny, J. Hantela, S. Ducharme, B. Lee, O.G. Symko, P. Taylor, D.Z. Zheng, J.A. Xu, Microwave absorption in the superconducting, normal phases of Y–Ba–Cu–O, Phys. Rev. B 36 (1987) 2361–2363.
[278] K.W. Blazey, K.A. Műller, J.G. Bednorz, W. Berlinger, G. Amoretti, E. Buluggiu, A. Vera, F.C. Matacotta, Low-field microwave absorption in the superconducting copper oxides, Phys. Rev. 36 (1987) 7241–7243.
[279] M. Peric, B. Rakvin, M. Prester, N. Brnicevic, A. Dulcic, Size of Josephson junctions in Ba–Y–Cu–O compounds, Phys. Rev. B 37 (1988) 522–524.

[280] R. Marcon, R. Fastampa, M. Giura, C. Matacotta, Evidence of Josephson junctions in sintered $YBa_2Cu_3O_7$ samples by means of microwave absorption in a low magnetic field, Phys. Rev. B 39 (1989) 2796–2799.
[281] N. Knauf, J. Fischer, P. Schmidt, B. Roden, R. Borowski, Büchner, H. Micklitz, A. Freimuth, D. Khomskii, V. Kataev, Grain size dependence of the Wohlleben effect in Bi-2212 high temperature superconductors, Physica C 299 (1998) 125–135.
[282] V. Kataev, N. Knauf, B. Büchner, D. Wohlleben, Inter- and intragranular effects in microwave absorption of $(Bi, Pb)_2Sr_2Ca_2Cu_3O_y$, Physica C 184 (1991) 165–171.
[283] A. Rycers, J. Spalek, cond-mat/0106188.
[284] D. Domínguez, E.A. Jagla, C.A. Balseiro, Wohlleben effect in a model granular high T_c superconductor, Physica C 235–240 (1994) 3283–3284.
[285] D. Dominguez, J.V. Jose, Magnetic and transport dc properties of inductive Josephson-junction array, Phys. Rev. B 53 (1996) 11692–11713.
[286] R. Kubo, et al., in: M. Cardona, P. Fulde, H.-J. Queisser (Eds.), Statistical Physics II, Springer Series in Solid-State Sciences, Springer, Berlin, 1985.
[287] D. Dominguez, J.V. Jose, A. Karma, C. Wiecko, Novel axisymmetric coherent vortex state in arrays of Josephson junctions far from equilibrium, Phys. Rev. Lett. 67 (1991) 2367–2370.
[288] D.C. Larbalestier, S.E. Babcock, X. Cai, M. Daeumling, D.P. Hampshire, T.F. Kelley, L.A. Lavanier, P.J. Lee, J. Seuntjens, Weak links, the poor transport critical currents of the 123 compounds, Physica C 153–155 (1988) 1580–1585.
[289] M. Peuckert, W. Becker, J. Bock, B. Hettich, H.W. Neumuller, M. Scharz, Melt processing and oxygen doping of bismuth superconductors, Physica C 162–164 (1989) 893–894.
[290] N. Murayama, Y. Torri, Increase in J_c of Bi–Pb–Sr–Ca–Cu–O superconductors by hot pressing, Physica C 162–164 (1989) 1261–1262.
[291] M.S. Li, D. Dominguez, AC resistivity of d-wave ceramic superconductors, Phys. Rev. B 62 (2000) 14554–14558.
[292] M.S. Li, H. Zung, D. Dominguez, Nonlinear ac resistivity in *s*-wave, *d*-wave disordered granular superconductors, Phys. Rev. Lett. 88 (2002) 257004-1–257004-4.
[293] J. Mannhart, D.G. Schlom, J.G. Bednorz, K.A. Műller, Influence of electric fields on pinning in $YBa_2Cu_3O_{7-x}$ films, Phys. Rev. Lett. 67 (1991) 2099–2102.
[294] X.X. Xi, C. Doughty, A. Walkenhorst, C. Kwon, Q. Li, T. Venkatesan, Effects of field-induced hole-density modulation on normal state and superconductivity transport in $YBa_2Cu_3O_{7-x}$, Phys. Rev. Lett. 68 (1992) 1240–1243.
[295] J. Mannhart, High-T_c transistors, Supercond. Sci. Technol. 9 (1996) 49–67.
[296] B.I. Smirnov, S.V. Krishtopov, T.S. Orlova, The effect of a strong electric field on the conductivity of the YBaCuO ceramic, Phys. Solid State 34 (1992) 1331–1332.
[297] B.I. Smirnov, T.S. Orlova, S.V. Krishtopov, Reversible effect of an electric field in yttrium and bismuth high-temperature superconducting ceramics, Phys. Solid State 35 (1993) 1118–1120.
[298] T.S. Orlova, B.I. Smirnov, Supercond. Sci. Technol. 7 (1994) 899;
B.I. Smirnov, T.S. Orlova, N. Kudymov, Influence of magnetic field on the reversible electric field effect in a high-temperature superconductivity ceramic, Phys. Solid State 36 (1994) 837–838.
[299] B.I. Smirnov, T.S. Orlova, Influence of an electric field on the hysteresis of the current–voltage characteristic of $YBa_2Cu_3O_{7-x}$/Ag, Phys. Solid State 36 (1994) 1883–1887.
[300] B.I. Smirnov, T.S Orlova, A.N. Kudymov, M.T. Lanagan, N. Chen, K.C. Goretta, Effect of an electric field on the current–voltage curves of monolithic $(Bi, Pb)_2$ $Sr_2Ca_2Cu_3O_x$ superconductors, Phys. Solid State 38 (1996) 1603–1606.
[301] T.S. Orlova, B.I. Smirnov, J.Y. Laval, Effect of an electric field on the I–V curves of $DyBa_2Cu_3$-xOy/1 wt.% PtHTSC ceramics, Phys. Sol. State 43 (2001) 1007–1011.
[302] B.I. Smirnov, T.S Orlova, K.C. Goretta, *I–V* characteristics, the electric-field effect in melt-grown YBa_2Cu_3Ox/Y_2BaCuO_5 HTSC crystals, Phys. Sol. State 42 (2000) 1207–1210.
[303] A.L. Rakhmanov, A.V. Rozhkov, Electric field effect on the critical current of SNS contact, Physica C 267 (1996) 233–242.
[304] S.A. Sergeenkov, J.V. Jose, Analog of magnetoelectric effect in high-T_c granular superconductors, Europhys. Lett. 43 (1998) 469–475.

[305] T.S. Orlova, A.N. Kudymov, B.I. Smirnov, D.J. Miller, M.T. Lanagan, K.C. Goretta, Electric field effect on the conductivity of highly textured $Bi_2Sr_2CaCu_2O_y$ superconductors, Physica (Amsterdam) 253C (1995) 194–198.
[306] B.I. Smirnov, T.S. Orlova, A.N. Kudymov, M.T. Lanagan, N. Chen, K.C. Goretta, Influence of experimental conditions on the electric field effect in the ceramic (BiPb)(2)$Sr_2Ca_2Cu_3O_x$, Phys. Solid State 39 (1997) 1759–1761.
[307] T.S. Orlova, B.I. Smirnov, J.Y. Laval, Correlation between the electric-field effect and weak-link type in $YBa_2Cu_{3-x}O_y$, $YBa_2Cu_{3-x}O_y/Ag_x$ high-T_c superconducting ceramics, Phys. Solid State 40 (1998) 1088–1090.
[308] D. Domínguez, C. Wiecko, J.V. José, Critical current enhancement due to an electric field in a granular d-wave superconductors, Phys. Rev. Lett. 83 (1999) 4164–4167.